Novel design methods and control strategies for oil and gas offshore power systems

Pierobon, Leonardo

Publication date:
2015

Document Version
Publisher's PDF, also known as Version of record

Novel design methods and control strategies for oil and gas offshore power systems

PhD Thesis

$$(EIv'')'' = q - \rho A \ddot{v}$$

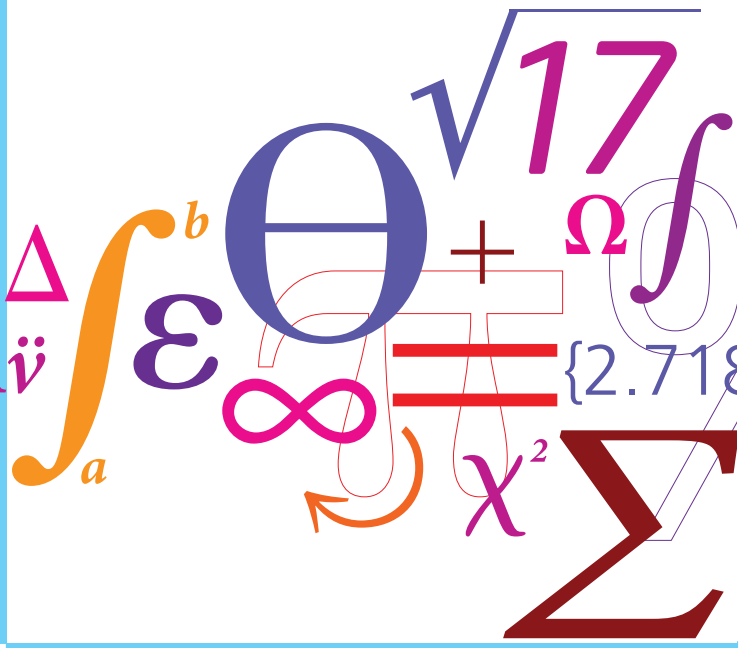

Leonardo Pierobon
DCAMM Special Report No. S83
October 2014

DTU Mechanical Engineering
Department of Mechanical Engineering

Novel design methods and control strategies for oil and gas offshore power systems

Leonardo Pierobon
M.Sc. Energy Engineering

Kongens Lyngby 2014

Novel design methods and control strategies for oil and gas offshore power systems

Doctoral Thesis
Print version
Font: Latin Modern typeset with LaTeX 2ε

Technical University of Denmark
Department of Mechanical Engineering
Section of Thermal Energy

Nils Koppels Allé, Building 403,
2800 Kongens Lyngby, Denmark
Phone +45 4525 4129
Fax +45 4588 4325
lpier@mek.dtu.dk
www.mek.dtu.dk

To my beloved mother Paola

and to my father Bruno

Abstract

This doctoral thesis is devoted to the research of innovative design methods and control strategies for power systems supplying future and existing offshore oil and gas facilities. The author uses these methods to address five research challenges: i) the definition of the optimal waste heat recovery technology, ii) the identification of the best working fluid to design efficient, light and cost-competitive waste heat recovery units, iii) the integration of dynamic criteria in the project phase to discard infeasible designs, iv) the development of a novel control strategy to optimally operate the power system, and v) the enhancement of its dynamic flexibility using the model predictive control. The case study of this work is the power system of the Draugen oil and gas platform (Kristiansund, Norway), where the possibility of equipping one of the gas turbines with a bottoming cycle unit is investigated.

The optimal technology is determined by programming a multi-objective optimization procedure, capable of optimizing the design of Rankine and Brayton engines. The objective functions are the daily carbon dioxide emissions, the weight of the components and the economic revenue. The optimization routine is interfaced with validated models sizing the heat transfer equipment. This software integration provides an initial estimate of the module compactness and of the impact of the pressure drops on the system performance. Finally, part-load and economic models quantify the spared emissions and the feasibility of the investment. The organic Rankine cycle technology has the largest potential to decrease the carbon dioxide emissions (10 - 15 %). On the other hand, the steam Rankine engine is more competitive from an economic perspective. The air Bryton cycles give the lightest modules (10 - 60 t). Therefore, this technology should be employed to retrofit existing offshore facilities with extended lifetime. Steam and organic Rankine engines are competing alternatives for new installations. The findings suggest to lean toward the use of organic Rankine cycle turbogenerators, if fuel-flexibility is a main priority for the platform operator. Engineering efforts should focus on cutting the production cost of the expander and on minimizing the core volume of the primary heat exchanger. In the selection of the working fluid, benzene and

cyclopentane are the organic compounds giving the highest performance, compactness and economic revenue. Considering the use of organic Rankine turbogenerators, dynamic analyses simulating critical scenarios (i.e. trip of one gas turbine) are shown to valuably complement the steady-state design procedure. The use of dynamic criteria can help identifying those candidates which do not meet the requirements of offshore electric grids. Specifically, the use of low-weight units is discouraged. It entails frequency fluctuations outside the specified tolerance (i.e. ±4 %) and instabilities in the process variables. Additionally, the proposed simulation tool can detect the system designs which expose the working fluid to unacceptable risk of chemical decomposition. Accounting for such phenomenon is of paramount importance as it may compromise the performance and lifetime of the components.

This work pays further attention to the design of an innovative controller to optimally operate one gas turbine connected to an organic Rankine cycle unit. The regulator uses the linear model predictive control to maintain the quality of the power supply, and, at the same time, to track the maximum performance of the plant. The speed of the pump of the organic Rankine cycle unit is varied to maximize the energy conversion efficiency of the plant. The controller can also verify real-time the actual feasibility of the optimal working condition with respect to operational constraints, i.e., the acid formation at the outlet of the primary heat exchanger and the decomposition of the working fluid. The results demonstrate that the activities at the peak efficiency are practicable from 40 % load to nominal power. The potential fuel savings are around 3 %. The increment of the final revenue can be up to 10 %. More conservative control strategies are advised at low-power activities (especially when burning combustibles with a high sulfur content), or when the thermal stresses on the working fluid should be minimized. Additionally, the controller is demonstrated to improve the dynamic flexibility of the plant compared to the reference controller designed by the gas turbine manufacturer. The model predictive control can reduce the frequency fluctuations in the range of 20 - 40 %, considering the gas turbine alone. The reduction increases up to 60 %, connecting the engine to the organic Rankine cycle module. The analysis on the effect of unmeasured disturbances (i.e. fouling in the heat transfer equipment) confirms the stability of the dynamic response. On the other hand, the results pinpoint the need for real-time upgrading of the internal models. This task is achievable adopting intelligent adaptation and learning techniques.

Resumé

Denne Ph.d.-afhandling omhandler forskning i innovative design- og optimeringsmetoder, og teknikker til avancerede kraftværkssystemer, der skal installeres på nye og eksisterende offshore olie- og gasplatforme. Systemet som studeres er generaliseret ved kraftværkssystemet som benyttes ombord på olie- og gasplatformen Draugen i Kristiansund, Norge.

De nævnte metoder anvendes til at adressere fem forskningsmæssige mål: i) Definition af den optimale varmegenvindingsteknologi, ii) identificering af de bedste arbejdsmedier til effektive, kompakte og økonomisk attraktive varmegenvindingskedler, iii) integration af dynamiske kriterier i projekteringsfasen, for at identificere uhensigtsmæssige designs, iv) udvikling af en kontrolstrategi, som sikrer optimal systemeffektivitet, og v) forbedring af den dynamiske fleksibilitet, ved hjælp af model predictive control algoritmer.

Den optimale teknologi bliver defineret ved hjælp af en nyudviklet optimeringsalgoritme, som kan identificere optimale Rankine- og Braytonprocesdesigns. Målene for optimeringerne er reducerede CO_2 emissioner og komponentvægt, samt det økonomiske potentiale. Optimeringsalgoritmen benytter validerede designmodeller af varmevekslere, som giver et umiddelbart estimat på varmegenvindingsmodulets kompakthed, og på betydningen af trykfald i fht. systemets effektivitet. Økonomiske modeller og dellastsimuleringer gør det muligt at kvantificere emissionsreduktioner og investeringsafkast.

Resultaterne indikerer at den organiske Rankineproces har det største potentiale for at reducere CO_2-emissioner, mens dampkraftsprocessen præsenterer det største økonomiske potentiale. Braytonprocessen giver de letteste moduler, og deres anvendelse anbefales i forbindelse med eftermontering på eksisterende offshore platforme, hvis levetid er forlænget.

Dampkraftsprocessen og den organiske Rankineproces er konkurrerende alternativer for nye installationer. Resultaterne indikerer at den organiske Rankineproces er fordel-

agtig i situationer hvor brændstofflexibilitet er vægtet højt. For denne proces anbefales det at koncentrere de tekniske bestræbelser omkring at minimere produktionsomkostningerne for ekspanderen og vægten af varmevekslere. Benzen og cyklopentan er, i denne proces, arbejdsmedier som fremviser de bedste præstationer, og de giver mulighed for at designe kompakte og økonomisk effektive kraftværksmoduler.

Den dynamiske analyse viser sig som et værdifuldt værktøj i designprocessen, idet den muliggør identifikationen af procesdesigns som ikke opfylder de specifikke krav som findes til offshore elnettet. I den forbindelse viser analyser at brugen af kompakte enheder bør frarådes pga. uacceptable frekvensudsving og procesustabilitet. Derudover kan det præsenterede simuleringsværktøj identificere systemdesigns, som udsætter arbejdsmediet for en uacceptabel risiko for kemisk nedbrydning.

Den dynamiske analyse er udvidet yderliggere ved udviklingen af et innovativt kontrolsystem, som har til formål at styre gasturbinen og det organiske Rankineproces kraftværksmodul, på den mest effektive måde. Kontrollogikken anvender en model predictive control algoritme, til at opretholde kvaliteten i elforsyningen og samtidigt at sikre den maksimale effektivitet af anlægget. Pumpens hastighed varieres således at driften altid sker med maksimal virkningsgrad. Kontrollogikken kan ydermere verificere om det optimale driftspunkt er opnået, givet de operationelle begrænsninger. Resultaterne indikerer, at maksimal effektivitet er mulig under laster fra 40 % op til nominel effekt, med potentielle brændstofbesparelser på omkring 3 % og en forøgelse af den økonomiske indkomst på op til 10 %.

Den foreslåede kontrollogik er også påvist at kunne føre til vigtige forbedringer i den dynamiske fleksibilitet, i forhold til standardkontrolleren. Feedbacksystemet kan i følge beregningerne lede til en 20 - 40 % reduktion af frekvensudsving for gasturbinen alene, og mere end 60 % reduktion med det organiske Rankineproces kraftværksmodul. Analyse af virkningen af ikke-målbare faktorer (såsom tilsmudsning i varmevekslerne) verificerer, at den dynamiske respons er mere stabil med det nyudviklede kontrolsystem. På den anden side viser resultaterne, at der er behov for en realtidsopdatering af de interne modeller, f.eks. vha. intelligente automatiserede adaptions- og læringsteknikker.

Preface

This thesis was prepared at the Section of Thermal Energy, Department of Mechanical Engineering, Technical University of Denmark (DTU) in fulfillment of the requirements for acquiring a Ph.D. degree in Mechanical Engineering. The work was performed from November 2011 to October 2014 under supervision of Associate Professor Fredrik Haglind (DTU), and co-supervision of Associate Professor Brian Elmegaard (DTU) and Ph.D. Rambabu Kandepu (Teknova A/S). The project was financed by the Norwegian Research Council through Petromaks with project number 203404/E30.

This doctoral thesis is produced as a monograph. It explores new design methods and control strategies for power systems on offshore oil and gas platforms. The three research areas are: i) steady-state optimization techniques to project the power system on board, ii) the introduction of dynamic criteria to discard infeasible plant designs, and iii) the development of a controller based on the model predictive control to optimally operate the power system.

Kongens Lyngby, 31-October-2014

Leonardo Pierobon

Acknowledgments

These three years of doctoral studies have been an exciting adventure not only from a research perspective but also from a human point of view. I see a research activity just like opening an unexplored route traveling along the way with loyal and skilled companions. Nowadays, the increasing need of knowledge on particular areas of engineering disciplines forces scientists to specialize on *niche* subjects. This unequivocal fact stresses the value of collaboration among persons with different expertises, and it empowers the research action. Indubitably, cooperation was the most important ingredient of my research. It enriched me professionally and humanly.

I am particularly grateful for the assistance given by my main supervisor, Associate Professor Fredrik Haglind (DTU). Our weekly meetings were moments of relevant scientific discussions, as well as of constructive criticisms which helped the development of my research skills. In this regard, I acknowledge the valuable assistance of my co-supervisors, Associate Professor Brian Elmegaard (DTU) and Ph.D. Rambabu Kandepu (Teknova A/S), for the time dedicated to support my activities. My special thanks are also extended to the staff at the Section of Thermal Energy, Department of Mechanical Engineering, DTU. In particular, I would like to mention the technical discussions and the nice moments spent with my co-workers: Martin Ryhl Kærn, Jorrit Wronski, Tuong Van-Nguyen, Andrea Mazzucco, Alberto Benato, Jesper Graa Andreasen, and Lorenzo Bellemo. Among my colleagues, I dedicate a special word to Ph.D. Ulrik Larsen. You gave me the possibility not only to work together on a number of research activities, but also to become a close friend, always helping me on the tortuous pathways of life. I also thank the former master's students co-supervised in their theses for helping me to extend my knowledge and improve my mentoring skills.

I wish to acknowledge Professor Piero Colonna (Delft University of Technology, the Netherlands) and Professor Erik Ydstie (Carnegie Mellon University, Pennsylvania), for giving me the opportunity to cooperate with their research groups as guest Ph.D. student. In The Netherlands, I had the privilege to work with Ph.D. Emiliano Casati and

Ph.D. Francesco Casella, who strongly contributed to the development of the DYNDES simulation tool presented here. During my period in the United States of America, the fruitful collaboration with Ph.D. Richard Chan and Krishna Iyengar led to the design of the control system disclosed in this thesis.

Finally, the funding from the Norwegian Research Council through Petromaks with project number 203404/E30 is acknowledged. Among the partners, I would like to thank Bo Ivarsson and Geir Nevestveit (Siemens Industrial Turbomachinery AB, Finspång, Sweden), for providing the dynamic model of the SGT-500 gas turbines and the necessary technical documentation. I am also grateful to Morten Hana (A/S Norske Shell) for the collection of the operational data from the Draugen oil and gas platform, and to Peter Breuhaus (IRIS A/S) for answering technical questions .

List of publications

Journal articles

Pierobon L, Benato A, Scolari E, Haglind F, Stoppato A. "Waste heat recovery technologies for offshore platforms." Applied Energy 136 (2014): 228–241. PDF file

Pierobon L, Casati E, Casella F, Haglind F, Colonna P. "Design methodology for flexible energy conversion systems accounting for dynamic performance." Energy 68 (2014): 667-679. PDF file

Pierobon L, Haglind F. "Design and optimization of air bottoming cycles for waste heat recovery in off-shore platforms." Applied Energy 118 (2014): 156-165. PDF file

Pierobon L, Nguyen T V, Larsen U, Haglind F, Elmegaard B. "Multi-objective optimization of organic Rankine cycles for waste heat recovery: Application in an offshore platform." Energy 58 (2013): 538-549. PDF file

Pierobon L, Rokni M, Larsen U, Haglind F. "Thermodynamic analysis of an integrated gasification solid oxide fuel cell plant combined with an organic Rankine cycle." Renewable Energy 60 (2013): 226-234. PDF file

Pierobon L, Rokni M. "Thermodynamic analysis of an integrated gasification solid oxide fuel cell plant with a Kalina cycle." International Journal of Green Energy 12 (2015): 610-619. PDF file

Pierobon L, Mazzucco A, Nguyen T V, Larsen U, Haglind F. "Part-load performance of a wet indirectly fired gas turbine integrated with an organic Rankine cycle turbogenerator." Energies 7 (2014): 8294-8316. PDF file

Larsen U, **Pierobon L**, Wronski J, Haglind F. "Multiple regression models for the prediction of the maximum obtainable thermal efficiency of organic Rankine cycles." Energy 65 (2014): 503-510. PDF file

Larsen U, **Pierobon L**, Haglind F, Gabrielii C. "Design and optimisation of organic Rankine cycles for waste heat recovery in marine applications using the principles of natural selection." Energy 55 (2013): 803-812. PDF file

Nguyen T V, **Pierobon L**, Elmegaard B, Haglind F, Breuhaus P, Voldsund M. "Exergetic assessment of energy systems on North Sea oil and gas platforms." Energy 62 (2013): 23-36. PDF file

Andreasen J G, Larsen U, Knudsen T, **Pierobon L**, Haglind F. "Selection and optimization of pure and mixed working fluids for low grade heat utilization using organic Rankine cycles." Energy 73 (2014): 204-213. PDF file

Barbazza L, **Pierobon L**, Mirandola A, Haglind F. "Optimal design of compact organic Rankine cycle units for domestic solar applications." Thermal Science 18 (2014): 811-822. PDF file

Peer-reviewed Conference Papers

Pierobon L, Wronski J, Elmegaard B, Haglind F, Bell I H. "DNA - an integrated open-source optimization platform for thermo-fluid systems." In Proceedings of 55th SIMS conference on Simulation and Modelling, pages 1-14, Ålborg, Denmark, October 2014.

Pierobon L, Schlanbusch R, Kandepu R, Haglind F. "Application of unscented Kalman filter for condition monitoring of an organic Rankine cycle turbogenerator." In Proceedings of 2014 Annual Conference of the Prognostics and Health Management Society, pages 1-8, Fort Worth, Texas, October 2014. PDF file

Pierobon L, Breuhaus P, Haglind F, Iyengar K, Kandepu R, Hana M. "Dynamic performance of power generation systems for off-shore oil and gas platforms." In Proceedings of ASME Turbo Expo 2014, pages 1-11, Düsseldorf, Germany, June 2014.

Pierobon L, Rambabu K, Haglind F, Fermi A, Rossetti N. "Technologies for waste recovery in off-shore applications." In Proceedings of ASME 2013 International Mechanical Engineering Congress & Exposition, pages 1-10, San Diego, California, November 2013.

Pierobon L, Nguyen T V, Larsen U, Haglind F. "Optimization of organic Rankine cycles for off-Shore applications." In Proceedings of ASME Turbo Expo 2013, pages 1-11, San Antonio, Texas, June 2013.

Pierobon L, Rambabu K, Haglind F. "Technologies for waste heat recovery in off-shore applications." In Proceeding of ASME 2012 International Mechanical Engineering Congress & Exposition, pages 1-10, Houston, Texas, November 2012.

Nguyen T V, Elmegaard B, **Pierobon L**, Haglind F, Breuhaus P. "Modelling and analysis of offshore energy systems on North Sea oil and gas platforms." In Proceedings of

53rd SIMS conference on Simulation and Modelling, pages 1-16, Reykjavik, Iceland, October 2012. PDF file

Nguyen T V, **Pierobon L**, Elmegaard B. "Exergy analysis of offshore processes on North Sea oil and gas platforms." In Proceedings of 3rd International Conference on Contemporary Problems of Thermal Engineering, pages 1-9, Gliwice, Poland, September 2012. PDF file

Nomenclature

A	area [m^2]
C_T	turbine constant [$kg \cdot K^{0.5} \cdot s^{-1} \cdot Pa^{-1}$]
F	factor in Equation A.14
F_{cu}	copper loss fraction
F_h	fin height [m]
F_l	fin length [m]
F_p	fin pitch [m]
F_t	fin thickness [m] temperature correction factor
G	mass flow velocity [$kg \cdot m^{-2} \cdot s^{-1}$]
H	inertia constant [s]
I	yearly income [$\$ \cdot s^{-1}$]
M	mass [kg]
M_f	maintenance factor
N	rotational speed [$rad \cdot s^{-1}$]
N_r	average number of tubes in a vertical tube row
N_{tp}	number of tube passes
P_l	longitudinal pitch [m]

R_{ct}	thermal conduction resistance [K · W^{-1}]
T	temperature [K]
U	overall heat transfer coefficient [W · m^{-2} · K^{-1}]
V	volume [m^3]
W	weight [kg] transfer function
X	steam moisture content
$\dot{G}$	corrected mass flow rate [kg · K$^{0.5}$ · s^{-1} · Pa^{-1}]
$\dot{N}$	corrected rotational speed [rad · s^{-1} · K$^{-0.5}$]
$\dot{P}$	power [W]
$\dot{V}$	volumetric flow rate [m^3 · s^{-1}]
$\dot{m}$	mass flow rate [kg · s^{-1}]
$\dot{n}$	corrected rotational speed ratio
$\dot{q}$	heat rate [W]
a_i	coefficients in Equation B.12
c	speed of sound [m · s^{-1}] specific cost [$ · kg^{-1}] heat capacity [J · kg^{-1} · K^{-1}]
c_1, c_2, c_3, c_4	coefficients in Equations B.2 and B.6
c_p	isobaric specific heat capacity [J · kg^{-1} · K^{-1}]
d	diameter [m]
f	Fanning factor or frequency [s^{-1}]
$f_m, f_p, f_{eta}, f_{sp}$	map scaling factors
h	heat transfer coefficient [W · m^{-2} · K^{-1}] specific enthalpy [J · kg^{-1}]
h_u	capacity factor
i	discount rate
j	Colburn factor
k	time index

l	length [m]
m	coefficient in Equations B.3 and B.5
m_{CO_2}	carbon dioxide emissions [$kg \cdot s^{-1}$]
n	number of stages life-time [s] polytropic exponent
p	pressure [Pa] coefficient in Equations B.3 - B.5 prediction horizon [s]
r_c	compression ratio
r_e	expansion ratio
s	specific entropy [$J \cdot kg^{-1} \cdot K^{-1}$] complex operator
t	time [s]
u	velocity [$m \cdot s^{-1}$] specific internal energy [$J \cdot kg^{-1}$]
v_{st}	specific volume in standard conditions [$m^3 \cdot kg^{-1}$]
z	summation index
LHV	lower heating value [$J \cdot kg^{-1}$]
Load	electric generator load
NPV	net present value [$]
Np	number of plates
Nt	number of parallel tubes
Nu	Nusselt number
PEC	purchased-equipment cost [$]
Pr	Prandtl number
Re	Reynolds number
SF	shaping factor
TCI	total capital investment [$]

nf	number of fins per meter [m^{-1}]

Abbreviations

ABC	air bottoming cycle
AC	air compressor
AMA	arithmetic mean average
AT	air turbine
CC	combustion chamber
CO_2	carbon dioxide
CSSA	Cerri's stage stacking analysis
DC	direct cost
FCI	fixed-capital investment
FH	fire hazard
FPHE	finned-plate heat exchanger
FRC	frequency controller
GB	gear box
GEN	electric generator
GWP	global warming potential
HEX	heat exchanger
HH	health hazard
HMIS	hazardous materials identification system
HPC	high pressure compressor
HPT	high pressure turbine
HRSG	heat recovery steam generator
IC	indirect cost
LPC	low pressure compressor
LPT	low pressure turbine
MD	measured disturbance

MO	measured output
MPC	model predictive control
MRE	mean relative error
MV	manipulated variable
NA	not available
NGL	natural gas liquid
ODP	ozone depletion potential
ORC	organic Rankine cycle
OTB	once-through boiler
PAT	power air turbine
PEC	purchased-equipment cost
PH	physical hazard
PI	proportional-integral controller
PT	power turbine
RSD	relative standard deviation
SRC	steam Rankine cycle
TCI	total capital investment
TEG	triethylene glycol
TUR	organic and steam Rankine cycle expander
UD	unmeasured disturbance

Greek letters

$\bar{\eta}$	normalized efficiency
$\bar{\phi}$	normalized flow coefficient
$\bar{\psi}$	normalized pressure coefficient
Δ	difference
ϵ	slack variable
η	efficiency

γ	exponent in Equation A.12
Γ_h	tube loading [$kg \cdot m \cdot s^{-1}$]
κ	isentropic exponent
λ	thermal conductivity [$W \cdot m^{-1} \cdot K^{-1}$]
μ	viscosity [$kg \cdot m^{-1} \cdot s^{-1}$]
ρ	density [$kg \cdot m^{-3}$]
ρ_e	weight on the slack variable
ξ	friction factor

Arrays and matrices

$\boldsymbol{R}_{\Delta u}$	weights on the rate of the manipulated variables
$\boldsymbol{J}$	objective functions
$\boldsymbol{Q}$	weights on the set-point deviations
$\boldsymbol{r}$	set-points
$\boldsymbol{R}_u$	weights on the deviation of the manipulated variables
$\boldsymbol{u}$	manipulated variables
$\boldsymbol{V}$	constraint relaxation
$\boldsymbol{X}$	variables
$\boldsymbol{y}$	measured outputs

Subscripts

a	air
b	baffle
c	cold side compressor condenser
f	fouling
h	hot side
i	inner
l	liquid

p	pump
r	recuperator
S	thermodynamic static state
T	thermodynamic total state
t	turbine tube
v	vapor
w	metal wall
CO_2	carbon dioxide
cr	critical point
des	design-point
eco	economizer
el	electric
eva	evaporator
exh	exhaust gases
gen	generator
in	inlet
is	isentropic
lm	logarithmic mean
max	maximum
min	minimum
ng	natural gas
off	off-design
out	outlet
ref	reference point
sh	shell-and-tube
sup	superheater

th	throat
wet	wet

Contents

Chapter 1

Introduction

This chapter provides the framework and motivations of the present Ph.D. thesis. It introduces the reader to the relevance and the large opportunities of energy optimization on offshore oil and gas platforms. A literature review delineates the state-of-the-art on the main topics of the present work, i.e., the design of waste heat recovery systems, the dynamic flexibility and the model predictive control. Subsequently, the author states the hypotheses which formed the leading thread of his investigation. This survey serves to present the novel contributions in terms of design methods and operational strategies.

1.1 Background and motivation

Despite recent advances in the performance of power plant technologies, inefficient power systems supply the energy demand on offshore oil and gas facilities. The primary scope of platform operators is to ensure a continuous fuel production with minimum risk of failure for the plant in the entire lifetime of a reservoir. Compactness and weight are pivotal design aspects to cut installation costs and maximize the economic revenue. Moreover, severe standards for the electric power supply, e.g., those on the frequency tolerance and recovery time, represent an additional challenge for offshore

plant designers. Gas turbine-based power systems can comply with these requirements by virtue of their open-cycle configuration and the internal combustion process. These features enable to design low-weight and compact units, and to attain a high dynamic flexibility. Nonetheless, large ratios of the work-to-heat demand impede to adequately use the exhaust energy for heating purposes. Moreover, conservative operational strategies deteriorate further the energy conversion efficiency during part-load activities.

Pollutant reduction and sustainable production are slowly arising as important concerns in the oil and gas sector [4]. Carbon tax on combustibles has constituted the primary resource for governments to explore the vast potentials in fuel saving. For instance, Norway levies carbon tax on hydrocarbon fuels since 1991. Its parliament has recently adopted a forceful measure to alleviate the environmental footprint in the oil and gas industry, with doubling the taxation to 55 $ per ton of carbon dioxide (CO_2) in 2013 [25]. Thus, sustainability of offshore power systems is nowadays regarded as strategic research area both from an environmental and economic point of view. Energy savings in the oil and gas sector are not to be regarded as a drop in the bucket. Statistics report that 14 % of the total greenhouse gas emissions of Norway in 2013 derived from this industrial activity [32]. The strongest efforts should be directed on the power system. These plants are responsible for the largest share of the CO_2 emissions offshore, as shown in Figure 1.1.

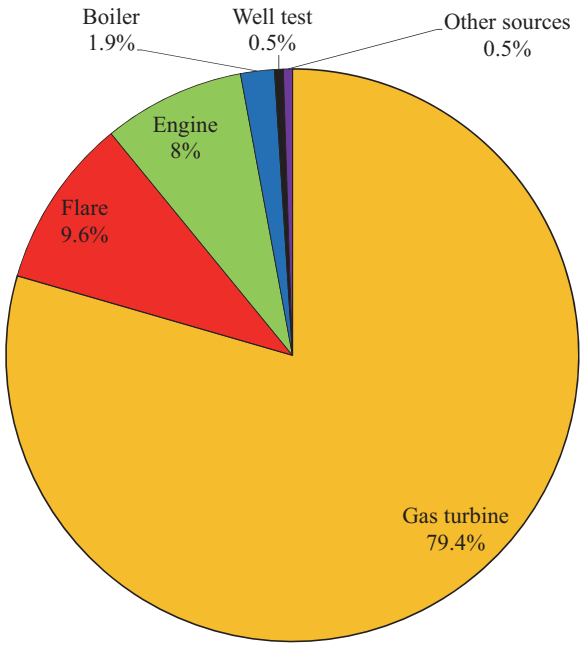

Figure 1.1: Carbon dioxide emissions from the petroleum activities in 2012 by source [33].

A direct remedy is the removal of on board power generators, relaying on conveyance of electricity from onshore. Recent surveys [10, 15] and gained operational experience

on actual facilities (for instance on the Troll A platform in the North Sea [19]) proved the economic feasibility of high-voltage direct current systems for low transportation ranges ($\approx 300\,\mathrm{km}$). However, advances in this technology are essential to extend the transmission distances, which platform operators foresee to increase in the near future. New research efforts aim attention at integrating renewable energies, e.g., wind power, in offshore facilities [16]. The solution appears attractive owing to uniform distribution of wind speed and space availability. On the other hand, the high installation costs limit the applicability in water depth of around hundred meters. Furthermore, a possible sudden loss of wind power constitutes a criticality which may arouse instabilities in the stand-alone electric grid [16]. Opportunities for diminishing emissions offshore may also derive by exploiting techniques for CO_2 capture and storage. For instance, the Sleipner gas field in the North Sea comprises a sequestration plant. Its task is the removal of CO_2 from the produced natural gas and its injection into the Utsira geological formation, see Torp and Gale [34]. Floating plants with large power outputs (up to 450 MW) for offshore electrification integrating compression, pre-conditioning and CO_2 capture are currently under investigations [17, 35]. As drawback, the sequestration process penalizes the plant efficiency (up to 9 %-points [17]). Moreover, it does not cope with the removal of other pollutants such as sulfur and nitrogen oxide.

Given the aforementioned research activities, this Ph.D. thesis focuses on exploring the opportunity of implementing conventional and novel bottoming units to recuperate the heat dispersed by offshore power stations. Onshore plants based on the combined cycle technology integrate Brayton and Rankine engines to attain performances exceeding the 60 %-barrier [12]. Nevertheless, these systems have been conceptually designed for steady-state operations and connection to vast electric grids. They can, therefore, afford heavy and bulky components, e.g., three-pressure level heat recovery steam generators (HRSGs), due to the vast accessibility of land. Advances in design methods are thus necessary to adapt these systems to offshore applications. This may allow to: 1) design compact and low-weight waste heat recovery units, 2) increase the energy conversion efficiency, 3) maintain a high plant reliability. The fourth task is to deliver a dynamic flexibility comparable to that of gas turbines. This requires to alleviate the effect of the thermal inertia of the heat exchangers harvesting the exhaust heat. Tackling this problem requires the use of dynamic metrics, e.g., rise time and maximum frequency deviation, as primary criteria from the very beginning of the design phase. A second possible measure is the implementation of more sophisticated controllers, e.g., the model predictive control (MPC).

1.2 Literature review

This part reviews the literature in the research fields outlined in Section 1.1. The first part focuses on the design and optimization of the bottoming cycle units. The section then presents, from a generic perspective, previous works related to the enhancement of dynamic flexibility in power plants. Finally, the state-of-the-art on the control systems of offshore facilities is traced, paying attention to the regulation of the power plant.

1.2.1 Waste heat recovery systems

Waste heat recovery systems are not a novelty in the offshore research field. To the author's knowledge, the first article dates back to 1996. Bolland et al. [8] performed a feasibility study on an air bottoming cycle (ABC) unit boosting the performance of the LM2500PE gas turbine. This engine is commonly used for offshore purposes. The ABC system, invented by Farrell [11] in 1988, comprises, in the basic configuration reported in Figure 1.2, two air compressors with intercooling, a heat exchanger recovering the exhaust heat and an air turbine. Bolland et al. [8] calculated that such system can add 10.5 %-points to the thermal efficiency of the LM2500PE engine. The weight and package cost were estimated to be 154 t and 9.4 M$, respectively. Recent studies [14, 26], however, underlined the need for novel configurations to further use the discharged power.

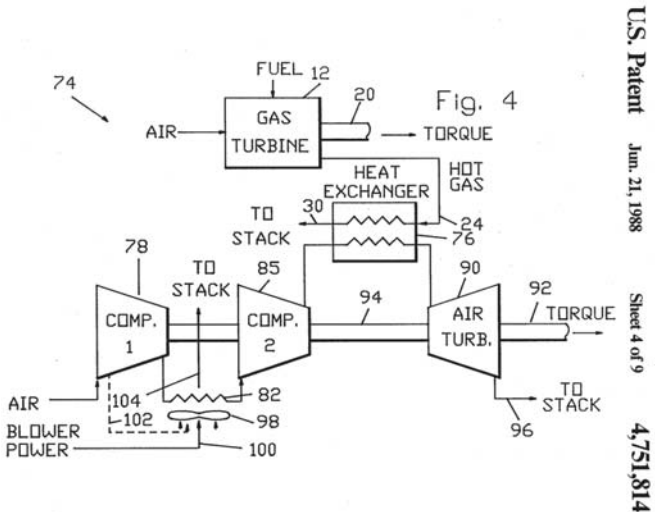

Figure 1.2: Original drawing of the US 4751814 patent of the air bottoming cycle system (Source: Farrell [11]).

A competitor is the steam Rankine cycle (SRC) technology. This engine detains a long operational history onshore. Few units are also present on offshore facilities. Kloster [21] reported challenges and functional experience of the existing SRC units in the Oseberg, Eldfisk and Snorre B platforms. For instance, the Oseberg field center was upgraded by constructing a new bridge-linked platform. A double-inlet heat recovery steam generator (see Figures 1.3(a) and 1.3(b)) recovers the heat from two LM2500+ gas turbines. The SRC unit was able to cut the fuel consumption by approximately $36 \cdot 10^6$ $Sm^3 \cdot yr^{-1}$ and the CO_2 emissions of about $80 \cdot 10^3$ $t \cdot yr^{-1}$ [21]. The double-inlet HRSG resulted in an additional load of 125 t. The design experience matured with the Oseberg project proved that new technologies and the simultaneous optimization of efficiency, investment and the design of the components could reduce weight and volume in the range of 30 - 50 % [21]. Aiming at reducing further the weight of the heat transfer equipment, Nord and Bolland [27] suggested the use of single-pressure once-through boilers (OTBs), instead of the heavier drum-type HRSGs. Simulations forecast that the implementation of the OTB technology enables the saving of approximately 30 t [27], compared to the drum-type single pressure HRSG.

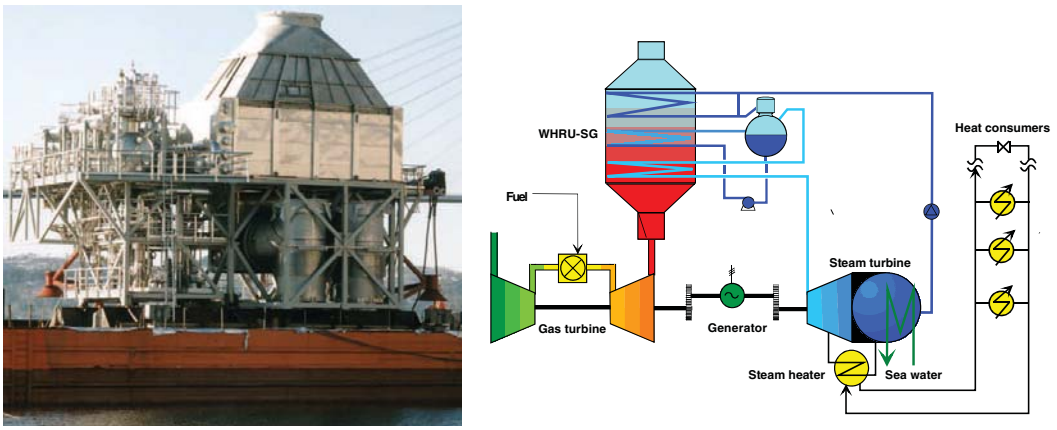

(a) (b)

Figure 1.3: Power system on the Oseberg field center (Source: Kloster [21]). 1.3(a): Double-inlet heat recovery steam generator. 1.3(b): Layout of the offshore combined heat and power cycle plant.

A third option to recuperate the exhaust heat is the use of organic Rankine cycle (ORC) power modules. These units operate in principle similarly to SRC units. The working fluid is instead an organic compound characterized by lower critical temperatures and pressures than water. This feature makes these systems suitable for low and medium temperature waste heat recovery, see Angelino et al. [3]. The ORC technology has recently acquired operational practice with geothermal and biomass plants. Few theoretical studies [2, 6, 7] related to offshore applications are present in the literature. The prospect of lighter and more compact systems is foreseen, given the high density of the working fluid. This characteristic could make this alternative more attractive than a SRC unit. Operating in supercritical conditions may decrease further the volume of the components. In this region, organic compounds, e.g., carbon dioxide, present specific

volumes comparable to those of liquid water. Contextually, supercritical CO_2 power units are a promising solution. Their possible implementation is currently under research in the EFFORT project [31], led by important players of the Norwegian oil and gas industry. Walnum et al. [36] obtained significant decrements of greenhouse emissions and pollutants both at design- and part-load conditions, by placing supercritical CO_2 modules at the bottom of the LM2500+ engine. Mazzetti et al. [24] demonstrated that the performance of the power system incorporating a dual-stage supercritical CO_2 bottoming unit is comparable with the values achieved by SRC modules.

1.2.2 Dynamics as design criterion

Operational flexibility is mandatory on offshore facilities where a limited number of generators powers a stand-alone electric grid. However, this feature is becoming increasingly important also for onshore power plants. The recent liberalization of the electricity markets, along with the rapid expansion of the utilization of non-dispatchable renewable energy sources, such as wind and solar radiation, is stressing the necessity-opportunity for improving the flexibility of conventional power systems [22]. New plant technologies play, therefore, a significant role in providing such adaptability. The electricity industry has acknowledged that this need will increase in the near future [5]. In the case of base-load power plants, new scheduling procedures are leading to the latest combined cycle units being designed to operate efficiently and reliably under a large range of rapidly varying conditions. Furthermore, both new coal and nuclear power plants are, nowadays, conceived with increased capability of operating under fast-load variations. In addition, older power stations are retrofitted to increase the performance during dynamic operations [20].

In this framework, dynamic modeling and simulation are becoming a powerful design tool, especially if the level of detail of system and component models can be tuned to the design needs. In a recent work, Garcia et al. [13] investigated options to increase the robustness of energy networks by simulating power flow scenarios in which multiple forms of energy commodities, e.g., electricity and chemical products, may be exchanged. Concerning the detailed study of advanced power systems, Zhu and Tomsovic [39] analyzed distributed combined cycle plants based on micro gas turbines and fuel cells. The aim was the reduction of the costs related to ancillary services in a deregulated market. As last example, Alobaid et al. [1] developed a detailed model of a complete combined cycle to study and optimize its start-up procedure.

1.2.3 Control strategies

On offshore installations, the gas turbines commonly operate in load sharing mode, i.e., two or more engines divide the load equally. Some others are on stand-by or on maintenance. The engines typically run at fairly low loads ($\approx 50\,\%$) to minimize the risk of failure. Such event can induce a high economic loss to the platform operator. Gas turbines deliver fast start-up times ($\approx 10\,\text{min}$). The addition of a bottoming cycle unit increases the time constant of the system by virtue of the thermal inertia of the heat exchangers. Moreover, the system reliability inherently decreases. This obligates to carefully monitor new process variables and to explore novel control strategies.

In this regard, the use of the model predictive control is a valuable tool to enhance the dynamic flexibility of the plant and to ensure its safe operation. These control systems act similarly to car drivers who know the desired reference trajectory (i.e. the road) for a finite horizon, and operate on the control devices (i.e. accelerator, break and gear) to follow such trajectory [9]. In analogy, the controller of a gas turbine opens/closes the fuel valve to provide a certain load and to maintain constant the frequency of the grid. Briefly summarized, the advantage compared to purely feedback controllers is that MPCs look ahead in time by counting on internal models. In the case of a gas turbine, these models set the correspondence between the valve position and the network frequency. In a similar way, a driver relays on many years of experience to press the break and keep the car on track. The reader may refer to Camacho and Alba [9] for a comprehensive description of the MPC theory.

As surveyed by Qin and Badgwell [28], model predictive control systems have been primarily applied in refining and petrochemical industries. However, the recent need for plant flexibility (see Section 1.2.2) has led to an increasing interest for its application to onshore power plants. Sáez et al. [30] developed a MPC unit to control the start-up, normal operation, and shut-down of a combined cycle power plant. The proposed algorithm was tested in a model of a real system. The results indicated improved tracking capacities and the possibility to decrease the fuel consumption by $3\,\%$ [30]. Control techniques based on the MPC for the same type of power plant were dealt with by Lopez-Negrete et al. [23]. Concerning the application to ORC units, Quoilin et al. [29] employed a dynamic model based on first principles to optimize the steady-state performance of the system for a number of operating conditions. Optimal process variables, e.g., evaporating temperature, were selected as set-points of properly tuned feedback controllers. Similarly, Zhang et al. [38] developed a MPC unit to efficiently control an ORC module. The reference trajectories were derived with a steady-state optimizer.

Few studies about the applicability of the MPC on offshore platforms are available in

the literature. Imsland et al. [18] integrated a dynamic model of an offshore processing plant with a MPC simulation tool to control a four-stage oil separation process. The results demonstrated smoother responses for the measured outputs (i.e. oil and water levels in the separator inlet) compared to the use of feedback controllers. Willersrud et al. [37] studied the application of MPCs for optimizing the oil generation of an offshore installation with particular focus on the production manifold. Findings suggested that the total oil export could raise by around $70\,Sm^3 \cdot d^{-1}$, corresponding to a yearly increased revenue of 16 M$.

1.3 Objectives and methods

This section introduces the scope of this thesis by listing the five hypotheses under investigation. Subsequently, a brief summary of the modeling instruments is presented with respect to the research works introduced in Section 1.2.

1.3.1 Thesis hypotheses

The main scope of this study is to propose novel design methodologies and control systems to facilitate the implementation of waste heat recovery technologies in offshore oil and gas facilities.

More specifically, this work aims at answering the following questions:

i) Is it possible to define the optimal waste heat recovery technology for existing and future oil and gas platforms?

ii) What is the optimal working fluid for the organic Rankine unit?

iii) Can the integration of dynamic criteria in the design procedure discard infeasible designs which do not meet the requirements of stand-alone electric grids?

iv) Is it feasible to devise a controller based on the model predictive control which can track the optimal energy conversion efficiency of the plant and preserve its availability?

v) Can this controller enhance the dynamic flexibility of the power system?

1.3.2 Modeling instruments

As far as hypotheses i) and ii) are concerned, this work proposes the use of a novel approach to design the waste heat recovery system. The design method uses a multi-objective optimization coupled with the genetic algorithm to search for the optimal system designs of each technology. The optimization routine performs the detailed design of the heat transfer equipment. It thus includes geometric quantities (e.g. tube length and diameter) among the optimization variables. This enables to estimate the weight of the heat transfer equipment. Moreover, the implementation of part-load and economic models within the optimization procedure enables to evaluate the yearly CO_2 emissions, and to estimate the profitability of the alternative investments. The objective functions are accordingly the economic revenue, the weight of the bottoming cycle unit and the daily CO_2 emissions.

The integration of dynamic performance criteria into the design process of power systems is proposed to address hypothesis iii). The multi-objective procedure is thus interfaced with a dynamic simulator. The tool can evaluate the transient performance of the system together with other typical design requirements. The approach is applied to size the ORC turbogenerator. More specifically, such method may discard plant configurations featuring unacceptable dynamic performance at an early design phase. This may avoid the risk of discovering criticality of transient operation after the commissioning of the offshore facility.

The present study proposes a novel controller to answer hypotheses iv) and v). The control system consists of a MPC and a steady-state optimizer. These two units ensure reliable operations and high performances over the entire lifetime of the facility. The regulator minimizes the frequency excursions during load changes. At the same time, a steady-state optimization algorithm tracks the peak efficiency of the plant for the new power duty. Additionally, the control system monitors crucial process variables, i.e., the highest temperature of the working fluid in the ORC unit and the exhaust gas temperature at the outlet of the once-through boiler. The controller also identifies in real-time the appropriate operational strategy for the bottoming cycle unit. The MPC can also ensure that practical limits on the control variables are respected. Tests on the robustness of the regulator are performed to verify the control stability in the presence of unpredictable events, e.g., fouling inside the heat exchangers of the bottoming cycle unit.

Bibliography

[1] F. Alobaid, R. Postler, J. Ströhle, B. Epple, and H.-G. Kim. Modeling and investigation start-up procedures of a combined cycle power plant. *Applied Energy*, 85 (12):1173 – 1189, 2008.

[2] T. Andresen, Y. Ladam, and P. Nekså. Simultaneous optimization of power cycle and heat recovery heat exchanger parameters. In *Proceedings of Supercritical* CO_2 *Power Cycle Symposium*, pages 1–7, Boulder, Colorado, May 2011.

[3] G. Angelino, M. Gaia, and E. Macchi. A review of Italian activity in the field of organic Rankine cycles. *VDI-Berichte*, 539(539):465–482, 1984.

[4] L. Arscott. Sustainable development in the oil and gas industry. *Journal of Energy Resources Technology*, 126(1):1–5, 2004.

[5] L. Balling. Flexible future for combined cycle. *Modern Power Systems*, 30(12): 61–65, 2010.

[6] J. E. Barrera, A. A. Sahlit, and E. Bazzo. Exergy analysis and strategies for the waste heat recovery in offshore platform. In *Proceedings of 22nd International Congress of Mechanical Engineering*, pages 1674–1682, Ribeirão Preto, Brasil, November 2013.

[7] R. Bhargava, M. Bianchi, L. Branchini, A. De Pascale, F. Melino, A. Peretto, and E. Valentini. Thermo-economic evaluation of ORC system in off-shore applications. In *Proceedings of ASME Turbo Expo 2014*, pages 1–13, Düsseldorf, Germany, June 2014.

[8] O. Bolland, M. Førde, and B. Hånde. Air bottoming cycle: use of gas turbine waste heat for power generation. *Journal of Engineering for Gas Turbines and Power*, 118:359–368, 1996.

[9] E. F. Camacho and C. B. Alba. *Model predictive control*. Springer, London, Great Britain, 2013. ISBN: 9781852336943.

[10] I. M. de Alegría, J. L. Martín, I. Kortabarria, J. Andreu, and P. I. Ereño. Transmission alternatives for offshore electrical power. *Renewable and Sustainable Energy Reviews*, 13(5):1027–1038, 2009.

[11] W. M. Farrell. Air cycle thermodynamic conversion system, June 1988. US Patent 4,751,814.

[12] R. Fischer, P. Ratliff, and W. Fischer. SGT5-8000H - product validation at Irsching 4 test center. In *Proceeding of PowerGen Asia*, pages 1–10, Kuala Lumpur, Malaysia, October 2008.

[13] H. Garcia, A. Mohanty, W.-C. Lin, and R. Cherry. Dynamic analysis of hybrid energy systems under flexible operation and variable renewable generation - Part I: Dynamic performance analysis. *Energy*, 52:1–16, 2013.

[14] M. Ghazikhani, M. Passandideh-Fard, and M. Mousavi. Two new high-performance cycles for gas turbine with air bottoming. *Energy*, 36(1):294–304, 2011.

[15] T. M. Haileselassie, M. Molinas, T. Undeland, et al. Multi-terminal VSC-HVDC system for integration of offshore wind farms and green electrification of platforms in the North Sea. In *Proceedings of Nordic Workshop on Power and Industrial Electronics*, pages 1–8, Espoo, Finland, June 2008.

[16] W. He, G. Jacobsen, T. Anderson, F. Olsen, T. D. Hanson, M. Korpås, T. Toftevaag, J. Eek, K. Uhlen, and E. Johansson. The potential of integrating wind power with offshore oil and gas platforms. *Wind Engineering*, 34(2):125–138, 2010.

[17] J. Hetland, H. M. Kvamsdal, G. Haugen, F. Major, V. Kårstad, and G. Tjellander. Integrating a full carbon capture scheme onto a 450MW_e NGCC electric power generation hub for offshore operations: Presenting the Sevan GTW concept. *Applied Energy*, 86(11):2298–2307, 2009.

[18] L. Imsland, P. Kittilsen, and T. S. Schei. Model-based optimizing control and estimation using Modelica model. *Modeling, Identification and Control*, 31(3): 107–121, 2010.

[19] P. Jones, L. Stendius, and A. Sweden. The challenges of offshore power system construction. Troll A, electrical power delivered successfully to an oil and gas platform in the North Sea. In *Proceedings of European Wind Energy Conference & Exhibition*, pages 75–78, Athens, Greece, February-March 2006.

[20] P. Keatley, A. Shibli, and N. Hewitt. Estimating power plant start costs in cyclic operation. *Applied Energy*, 111:550–557, 2013.

[21] P. Kloster. Energy optimization on offshore installations with emphasis on offshore combined cycle plants. In *Proceedings of Offshore Europe Conference*, pages 1–9, Aberdeen, Great Britain, September 1999.

[22] W. Lise, J. van der Laan, F. Nieuwenhout, and K. Rademaekers. Assessment of the required share for a stable EU electricity supply until 2050. *Energy Policy*, 59 (0):904 – 913, 2013.

[23] R. Lopez-Negrete, F. J. D'Amato, L. T. Biegler, and A. Kumar. Fast nonlinear model predictive control: Formulation and industrial process applications. *Computers & Chemical Engineering*, 51(0):55 – 64, 2013.

[24] M. Mazzetti, P. Nekså, H. T. Walnum, and A. K. Hemmingsen. Novel energy efficiency technologies for reduction of offshore CO_2 emissions. In *Proceedings of Offshore Technology Conference*, pages 1339–1350, Houston, Texas, May 2013.

[25] Ministry of the Environment. The Government is following up on the Climate Agreement. Press release, October 2012. [accessed: 01/07/2014].

[26] Y. S. Najjar and M. S. Zaamout. Performance analysis of gas turbine air-bottoming combined system. *Energy Conversion and Management*, 37(4):399–403, 1996.

[27] L. O. Nord and O. Bolland. Steam bottoming cycles offshore - Challenges and possibilities. *Journal of Power Technologies*, 92(3):201–207, 2012.

[28] S. J. Qin and T. A. Badgwell. An overview of industrial model predictive control technology. In *Proceedings of Fifth International Conference on Chemical Process control*, pages 232–256, Tahoe city, California, January 1996.

[29] S. Quoilin, R. Aumann, A. Grill, A. Schuster, V. Lemort, and H. Spliethoff. Dynamic modeling and optimal control strategy of waste heat recovery organic Rankine cycles. *Applied Energy*, 88(6):2183–2190, 2011.

[30] D. Sáez, R. Zúniga, and A. Cipriano. Adaptive hybrid predictive control for a combined cycle power plant optimization. *International Journal of Adaptive Control and Signal Processing*, 22(2):198–220, 2008.

[31] SINTEF. The EFFORT project. Website, December 2012. [accessed: 10/05/2014].

[32] Statistics Norway. Emissions of greenhouse gases, 2013, preliminary figures. Website, May 2014. [accessed: 01/07/2014].

[33] Y. Tormodsgard. FACTS 2014 - The Norwegian petroleum sector. Technical Report Y-0103/15 E, Ministry of Petroleum and Energy, May 2014.

[34] T. A. Torp and J. Gale. Demonstrating storage of CO_2 in geological reservoirs: The Sleipner and SACS projects. *Energy*, 29(9):1361–1369, 2004.

[35] H. Undrum, O. Bolland, and E. Aarebrot. Economical assessment of natural gas fired combined cycle power plant with CO_2 capture and sequestration. In *Proceedings of Fifth International Conference on Greenhouse Gas Control Technologies*, pages 1–6, Cairns, Australia, August 2000.

[36] H. T. Walnum, P. Nekså, L. O. Nord, and T. Andresen. Modelling and simulation of CO_2 (carbon dioxide) bottoming cycles for offshore oil and gas installations at design and off-design conditions. *Energy*, 59(0):513 – 520, 2013.

[37] A. Willersrud, L. Imsland, S. O. Hauger, and P. Kittilsen. Short-term production optimization of offshore oil and gas production using nonlinear model predictive control. *Journal of Process Control*, 23(2):215–223, 2013.

[38] J. Zhang, Y. Zhou, R. Wang, J. Xu, and F. Fang. Modeling and constrained multivariable predictive control for ORC (organic Rankine cycle) based waste heat energy conversion systems. *Energy*, 66:128–138, 2014.

[39] Y. Zhu and K. Tomsovic. Development of models for analyzing the load-following performance of microturbines and fuel cells. *Electric Power Systems Research*, 62:1–11, 2002.

Chapter 2

The case study

This chapter describes the main characteristics of the Draugen oil and gas platform and of its power system. The author presents the integration of the bottoming cycle units in the gas turbine-based plant configuration, outlining major design considerations and relevant assumptions.

2.1 The reservoir

The Draugen oil field lies in the Haltenbanken province of the Norwegian Sea, and it is part of the Norwegian continental shelf, see Figure 2.1(a). The site, proved in 1984 [13], is situated around 150 km north of Kristiansund (Norway). Draugen started the operations in October 1993 under direction of Norske Shell. It, currently, constitutes a milestone for the Norwegian oil industry as the first field to begin production north of the 62nd parallel. The reservoir comprises two separated zones, i.e., Garn West and Rogn South. It consists of sandstones dating back to the late Jurassic Rogn formation. Both sites are relatively large, flat and homogeneous. These features facilitate oil and gas extraction operations which are executed with the aid of gas lift and pressure maintenance through water injections. A concrete gravity base structure supports the

platform sustained by means of a deep water construction with a single-shaft (mono-tower) arrangement. The expected average production was around $90 \cdot 10^3$ barrels per day of oil with peak exports of $225 \cdot 10^3$ barrels per day. The gas exports in 2008 totaled roughly $500 \cdot 10^3$ $Sm^3 \cdot d^{-1}$. The installation consists of 13 wells, six horizontal ones drilled from the platform and seven sub-sea completions. The platform produces

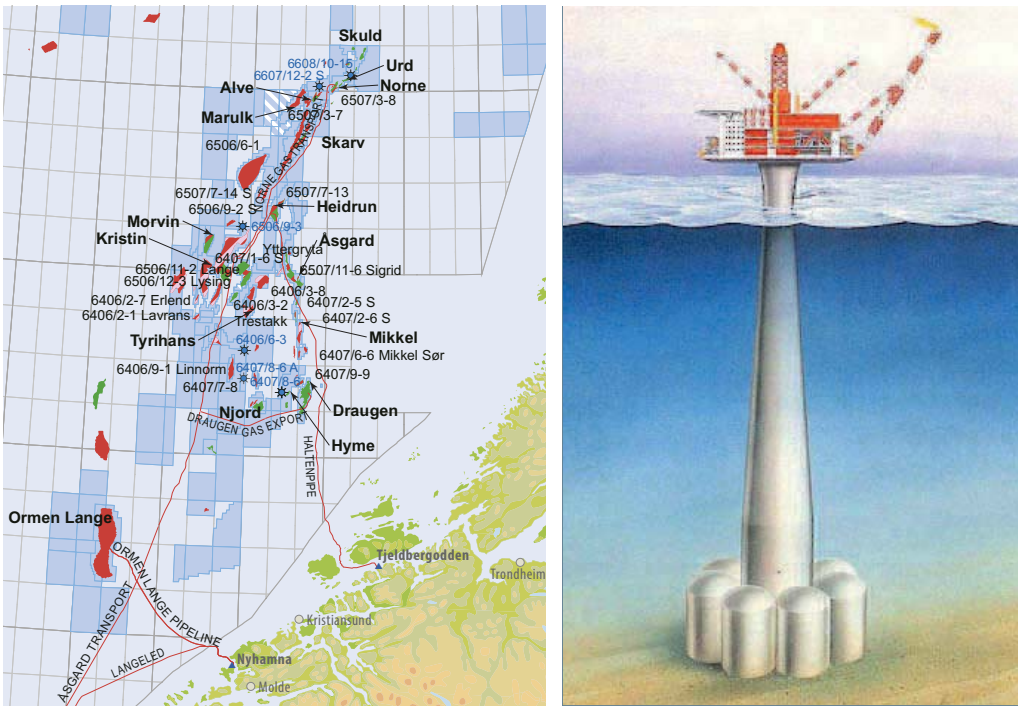

(a) (b)

Figure 2.1: The Draugen oil field (Source: Tormodsgard [16]). 2.1(a) The Norwegian Sea oil field and the gas pipelines. 2.1(b) The single shaft (mono-tower) platform and oil cells.

gas exported via Åsgard gas pipeline (see Figure 2.1(a)) to Kårstø (Norway). Here the natural gas and condensate from the fields in the northern parts of the North Sea are processed and delivered to the European gas network. Seven cells arranged around the concrete monocolumn contain the oil from Draugen. A floating buoy loads the petroleum into a shuttle tanker which ships the fuel onshore, typically once every 1-2 weeks. Table 2.1 resumes the main characteristics of the Draugen site.

Table 2.1: Characteristics of the Draugen oil and gas field (Source: Norske Oljemuseum [13]).

Site	Draugen
Block	6407/9
Production license	093
Awarded	1984
Total recoverable reserves	900 millions of oil barrels
	1.5 billions of Sm^3
	2.4 millions of tonnes of natural NGL*
Remaining at 31/12/2008	133.3 millions of oil barrels
	0.1 billions of Sm^3
	0.4 millions of tonnes of NGL*
Discovery year	1984
Approved for development	19/12/1988
On stream	19/10/1993
Operator	Norske Shell
Operations organization	Kristiansund
Main supply base	Kristiansund
Licensees	Norske Shell (26.20 %), Petoro (47.88 %)
	BP Norge (18.36 %), Chevron Norge (7.56 %)

*NGL: Natural gas liquids, i.e., components separated in the form of liquids.

2.2 The power system

Figure 2.2 shows the layout of the power system on Draugen. The plant comprises three Siemens SGT-500 gas turbines to cover the electric power demand. Major electric consumers ($\approx$ 15 MW) are: i) the three-stage compression unit which builds up the gas pressure from 7-8 to 180 bar, ii) the oil export pumps, iii) the sea-water lift and injection pumps, and iv) the gas re-compression module. Process and utilities consume around 4 MW of electricity. Two turbines run at a time covering 50 % of the load each. The third one is kept on standby, allowing for maintenance work. Despite the low performances (20 - 25 %), this strategy ensures the necessary reserve power for peak loads and the safe operation of the engines. Figure 2.3 reports the duration curve of the electric load in 2012 on the Draugen platform. The values on the ordinate are normalized with respect to the yearly average load, i.e., 19 MW. The curve allows to determine the number of days per year when the load was larger than the value selected on the ordinate. The plot indicates that the power demand exceeded the nominal value for less than 50 days. The peak value (25 MW) was due to oil export activities (ZONE 1). The load was constant and equal to 19 MW (ZONE 2) for most of the time ($\approx$ 80 %). In the remaining operating hours, the power system was shut-down for maintenance operations (ZONE 3).

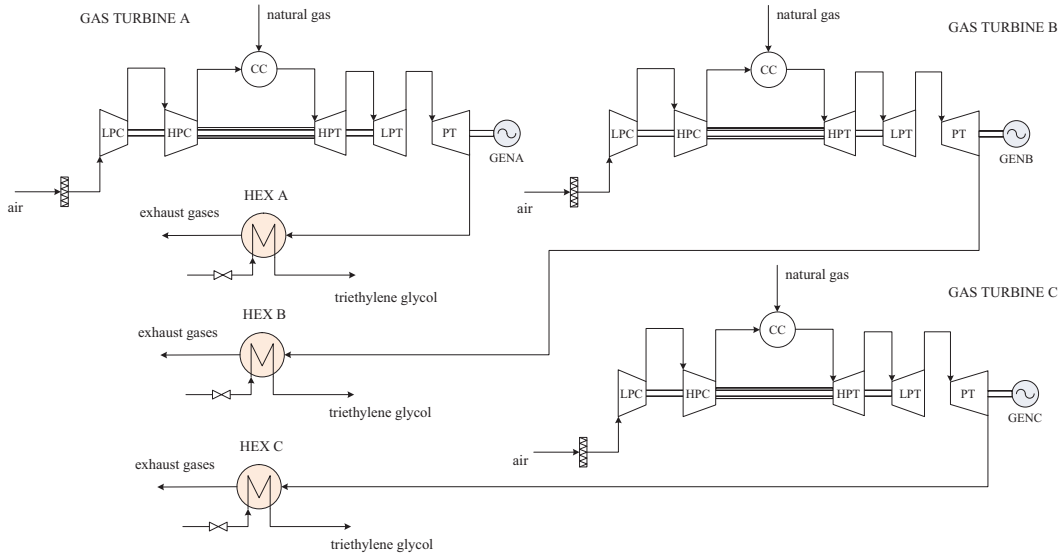

Figure 2.2: Simplified layout of the power system on the Draugen offshore oil and gas platform. Three twin-spool gas turbines produce the electric power demand. Three heat exchangers supply the heat used in the oil separation units.

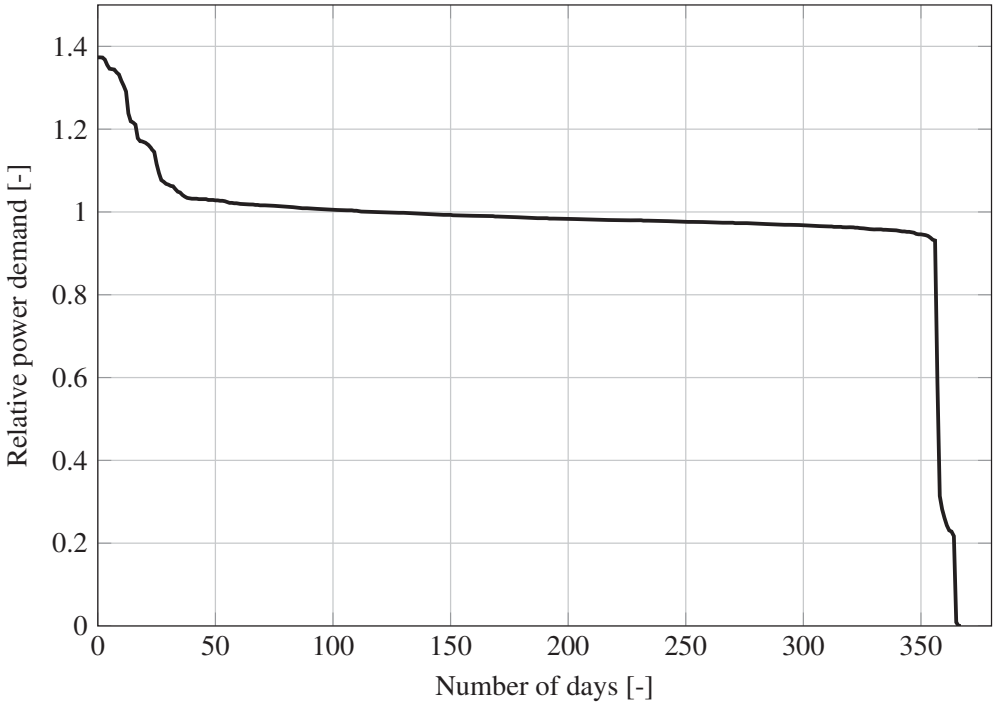

Figure 2.3: Duration curve of the electric load in 2012 on the Draugen oil and gas platform. ZONE 1 (0 → 50 d): oil exports activities with a peak load of 25 MW, ZONE 2 (50 → 355 d) nominal operation with a power demand of 19 MW, and ZONE 3 (355 → 365 d) shut-downs for maintenance procedures.

Table 2.2 lists the design-point specifications of the gas turbines as provided by the manufacturer. The engine model is the C-version launched in the beginning of the 1980's. The engines can work with different fuels (natural gas, naphtha, heavy fuel oil and syngas) owing to the relatively low turbine inlet temperature (850 °C). This feature ensures high reliability and short maintenance periods (no blade cooling). The twin-spool engines employ two coaxial shafts coupling the low pressure compressor (LPC) with the low pressure turbine (LPT) and the high pressure compressor (HPC) with the high pressure turbine (HPT). The power turbine (PT) transfers mechanical power through a dedicated shaft to the electric generator (GEN). Natural gas is the fuel used in the combustion chamber (CC). The air intake filter protects the gas turbine components from degradation caused by exposure to outdoor air pollutants.

Table 2.2: Design-point specifications of the twin-spool gas turbine installed on the Draugen offshore oil and gas platform.

Model	**Siemens SGT-500**
Turbine inlet temperature	850 °C
Exhaust gas temperature	379.2 °C
Exhaust gas mass flow rate	91.5 $kg \cdot s^{-1}$
Electric power output	16.5 MW
Thermal efficiency	31.3 %
Fuel	Natural gas

Three heat exchangers (HEXs) disposed in parallel recuperate the exhaust energy using triethylene glycol as heating medium. The heat demand is relatively low (4-6 MW). The oil heater and the condensate re-boiler are the major consumers of the thermal power. Additionally, the platform features two dedicated SGT-200 Siemens gas turbines. The engines drive mechanically the water injection pumps via gear box (GB) connection. Following the principle of redundancy, one engine runs at a time, while the other is on standby.

2.3 Integration of the bottoming cycle units

This section shows the implementation of the waste heat recovery technologies (i.e. steam Rankine cycle, air bottoming cycle and organic Rankine cycle) in the existing power system supplying the Draugen platform. Supercritical CO_2 cycle configurations (see Section 1.2.1), although potentially interesting in a long-term perspective, are not analyzed in this work. These systems are still in the development phase, and only few small-scale experimental facilities have been constructed yet.

2.3.1 The steam Rankine cycle

Figure 2.4 shows the layout of the power system where an additional SRC unit recovers the thermal power discharged by gas turbine A. The three gate valves permit to switch operation between the heat production module and the bottoming cycle unit. Moreover, this arrangement enables to recuperate the waste heat alternatively from the other two engines. This practice ensures high performances when switching the gas turbines on operation. Preliminary calculations suggest that this configuration is the most suitable from an economic perspective and in terms of space and weight requirements. Incrementing the performance of the plant by adding one unit for each gas turbine, or designing the SRC module for the exhaust heat of three engines does not compensate for the lower capacity factor, thus resulting in a poor economic revenue. Moreover, these alternatives lead to larger volumes and heavier power systems.

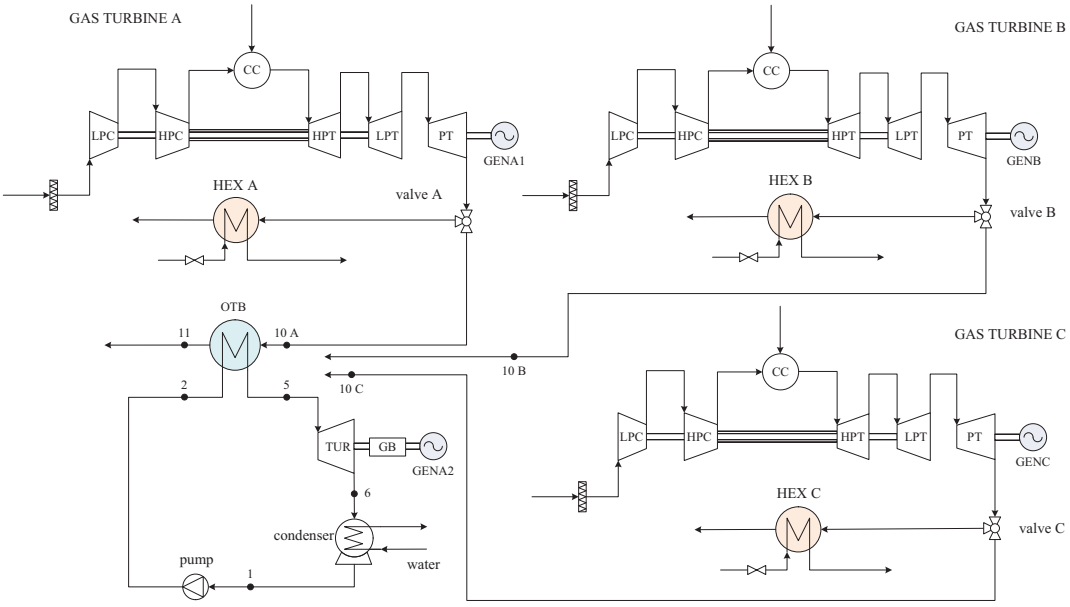

Figure 2.4: Simplified layout of the power system on the Draugen offshore oil and gas platform. The steam Rankine cycle module recovers the thermal power released with the exhaust gases of one engine, in this case gas turbine A.

The SRC unit comprehends the single-pressure non-reheat once-through boiler (OTB), the steam turbine, the sea-water cooled shell-and-tube condenser and the feed-water pump. As surveyed by Nord and Bolland [12], this basic configuration attains slightly lower efficiencies (-3 %) compared to the use of dual-pressure HRSGs. On the other hand, it allows to minimize the space requirement and the total weight. A vacuum deaerator directly coupled with the condenser (see Athey et al. [2]) removes the non-condensible gases from the vapor exiting the steam turbine and the make-up water. The latter addition compensates for the amount of expelled gases and steam leakages in the high-pressure section. Forecasting a net power output for the bottoming unit between

3 and 6 MW, the steam turbine requires rotational speeds around 7500 rpm [15]. This angular velocity enables to design reasonable stage geometries, especially with respect to the blade height, and to attain relatively high isentropic efficiencies. The SRC unit is thus equipped with a gear box connecting the expander to the electric generator (GENA2).

2.3.2 The organic Rankine cycle

In Figure 2.5, the bottoming cycle unit is an ORC turbogenerator using an organic compound as working fluid. Its selection constitutes a decisive aspect to design highly-efficient and cost-competitive ORC power modules. As surveyed by Trapp and Colonna [17], the ideal candidate should be available at low costs, have low environmental impact, flammability and toxicity. After a preliminary pre-screening procedure based on these criteria, the optimization of the plant performance and the feasibility of the component designs lead to designate the optimal fluid, see Section 4.1.2.

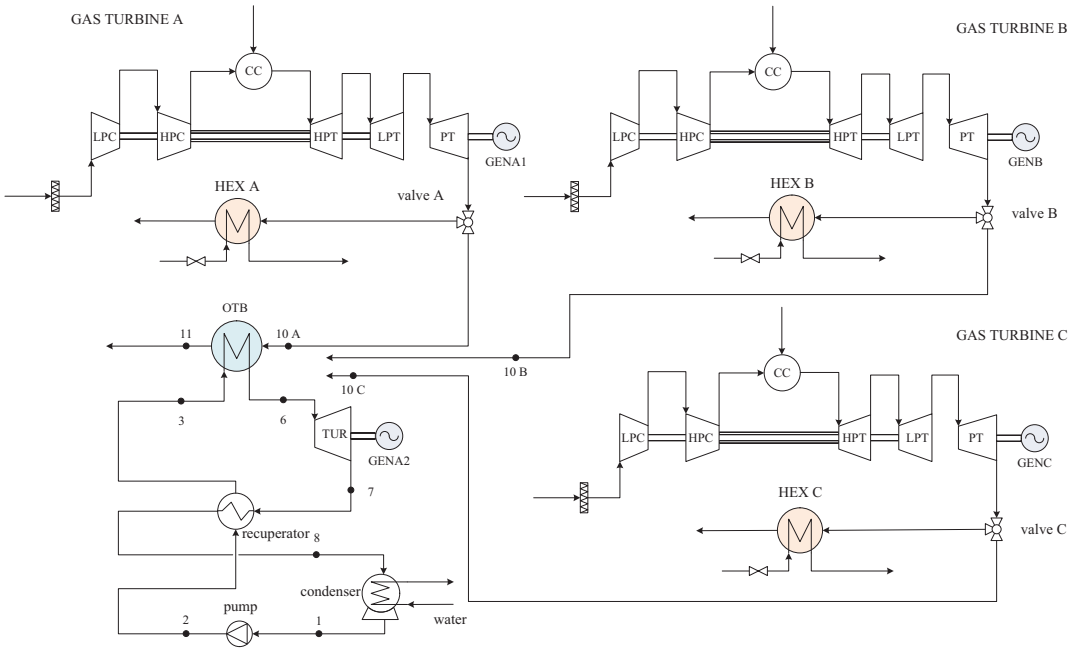

Figure 2.5: Simplified layout of the power system on the Draugen offshore oil and gas platform. The organic Rankine cycle module recovers the thermal power released with the exhaust gases of one engine, in the case gas turbine A.

The layout is similar to that of the SRC power module. Unlike water (wet fluid), the slope of the saturation curve of organic compounds is positive (dry fluid). The expansion process terminates with largely superheated vapor, see Figure 2.6. A shell-and-tube recuperator is thus added to decrease the energy contained in the stream exiting

the ORC turbine. This technique enhances the performance of the unit by virtue of the lower irreversibility in the heat addition process and during condensation. Organic compounds exhibit lower speeds of sound and higher molecular weights compared to water. The enthalpy drop during expansion is thus lower. This allows to design low-cost single- or two-stage turbines with lower tangential speeds and larger blade heights compared to water. These benefits translate in the opportunity to couple directly the expander to the electric generator, thus avoiding the use of a gear box. The reader may consult Quoilin et al. [14] for a more exhaustive comparison between the use of water and organic compounds as working fluid in power plants.

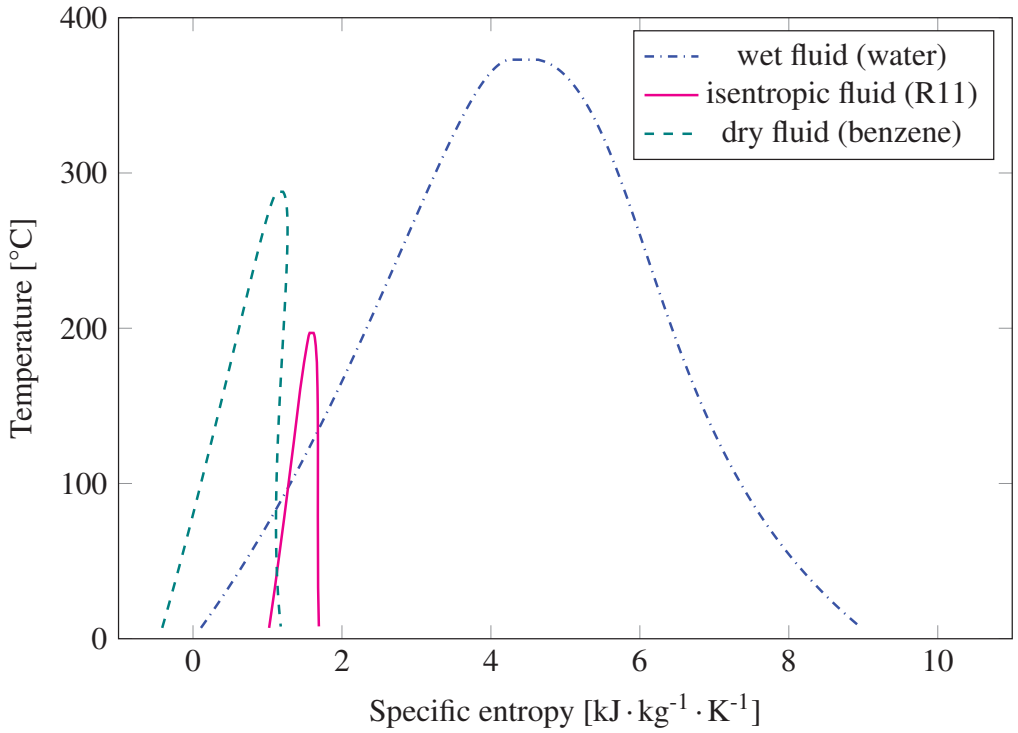

Figure 2.6: Examples of saturation domes in a $T - s$ diagram for wet fluid (water), isentropic fluid (R11) and dry fluid (benzene).

Given the temperature level of the exhaust gases (see Table 2.2), stability of the working fluid arises as important concern. Organic fluids experience chemical deterioration and decomposition at high temperatures ($\approx 300\,°C$). This criticality is owed to the breakage of chemical bonds between the molecules and the formation of smaller compounds which can then react to create other hydrocarbons. The system performance strongly relates to the transport and physical properties of the working fluid. Therefore, those chemical phenomena can severely reduce the net power output and the lifetime of the components. Five hydrocarbons are thus pre-selected as possible candidates. Table 2.3 lists their thermodynamic properties at the critical point, the health, physical and environmental hazards, the ozone depletion potential (ODP) and the global warming potential (GWP) in 100 years.

Table 2.3: Hazard ratings, global warming potential, ozone depletion potential and thermodynamic state at the critical point of the working fluid candidates for the organic Rankine cycle unit.

Fluid	HH/FH/PH[1]	GWP[2]	ODP	T_c [K]	p_c [bar]	M_c [g · mol^{-1}]
Cyclopentane	2/3/0	≈3.0	0	511.7	45.7	70.1
Cyclohexane	1/3/0	<3.5	0	553.6	40.8	84.1
Isopentane	1/4/0	<3.0	0	460.3	33.7	72.1
Benzene	2/3/0	<2.6	0	562.0	49.0	78.1
Isohexane	2/3/0	<3.5	0	497.7	30.4	86.1

[1] Hazard classification based on the hazardous materials identification system (HMIS) developed by the American coatings association [11]. HH = health hazard, FH = fire hazard, PH = physical hazard.
[2] Global warming potential over a period of 100 years.

The fluid hazards are quantified according with the hazardous materials identification system (HMIS) developed by the American coatings association [11]. Figures for the GWP and ODP of the hydrocarbons are obtained from the open literature [4, 6]. For two of these compounds (i.e. benzene and cyclopentane), the thermal stability was experimentally verified up to a temperature of 300 °C, see Andersen and Bruno [1] and Ginosar et al. [7], respectively. Cyclopentane is currently adopted for operating ORC systems in this range of temperature, see Del Turco et al. [5]. Note that chemical compounds belonging to the siloxane family and toluene were not considered in this study, despite their chemical stability was proved at operating temperatures higher than 300 °C, see Heberle et al. [8] and Larjola [10], respectively.

2.3.3 The air bottoming cycle

Figure 2.7 shows the power plant configuration with the ABC unit at the bottom of gas turbine A. The first compressor (AC1) intakes ambient air which is then cooled down in the intercooler. This technique decreases the specific work of the second compressor (AC2) owing to the lower air inlet temperature. The AC2 increases further the pressure of the working fluid which then harvests the exhaust energy from the gas turbine in the finned-plate heat exchanger (FPHE). As reported in Kays and London [9], this device offers higher performances and compactness for gas-to-gas heat transfer processes compared to shell-and-tube and flat-plate heat exchangers. The air then expands through the air turbine (AT2) which drives the second compressor and, afterwards, through the air turbine (AT1) mechanically connected to AC1. Finally, the power air turbine (PAT) produces electric power driving the generator. Figure 2.7 shows the twin-spool arrangement with one intercooler. On the other hand, more simple or advanced

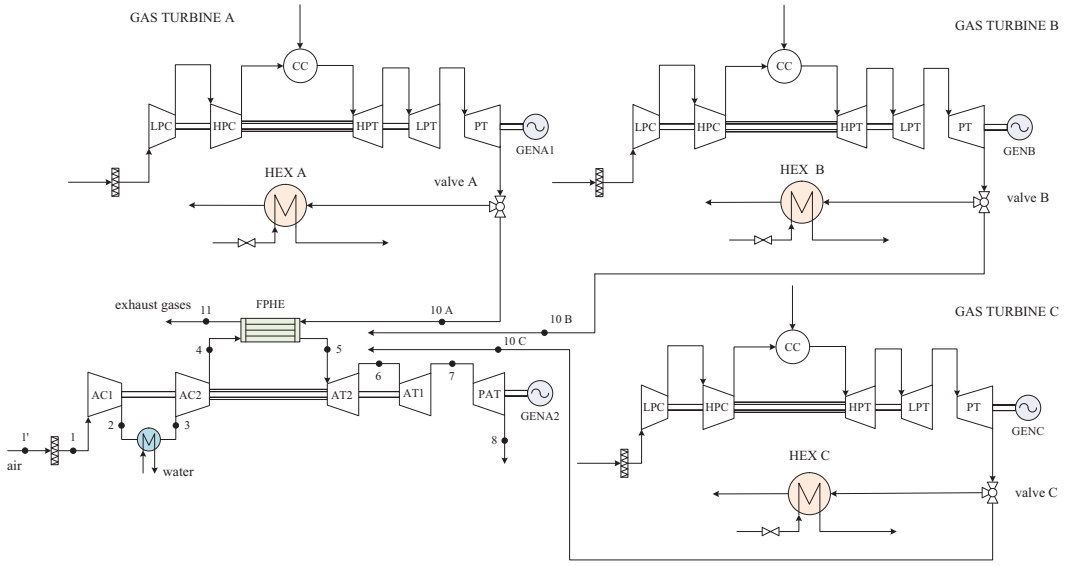

Figure 2.7: Simplified layout of the power system on the Draugen offshore oil and gas platform. The air bottoming cycle module with the intercooler recuperates the exhaust energy from gas turbine A.

configurations are available, e.g., two intercoolers with a single-spool, no intercooler with two spools, etc.. The motivation for the selection of the arrangement proposed in Figure 2.7 is discussed in details in Bolland et al. [3].

Bibliography

[1] W. C. Andersen and T. J. Bruno. Rapid screening of fluids for chemical stability in organic Rankine cycle applications. *Industrial & Engineering Chemistry Research*, 44(15):5560–5566, 2005.

[2] R. E. Athey, B. J. Martin, and E. Spencer. Condensate oxygen control in a combined cycle system without a conventional deaerator - test results. In *Proceedigs of Electric Power Research Institute Condenser Technology Conference*, pages 1–8, Boston, Massachusetts, September 1990.

[3] O. Bolland, M. Førde, and B. Hånde. Air bottoming cycle: use of gas turbine waste heat for power generation. *Journal of Engineering for Gas Turbines and Power*, 118:359–368, 1996.

[4] W. Collins, R. Derwent, C. Johnson, and D. Stevenson. The oxidation of organic compounds in the troposphere and their global warming potentials. *Climatic Change*, 52(4):453–479, 2002.

[5] P. Del Turco, A. Asti, A. Del Greco, A. Bacci, G. Landi, and G. Seghi. The ORegen waste heat recovery cycle: Reducing the CO_2 footprint by means of overall cycle efficiency improvement. In *Proceedings of ASME Turbo Expo 2011*, pages 547–556, Vancouver, Canada, June 2011.

[6] P. Forster, V. Ramaswamy, P. Artaxo, T. Berntsen, R. Betts, D. W. Fahey, J. Haywood, J. Lean, D. C. Lowe, G. Myhre, et al. Changes in atmospheric constituents and in radiative forcing. Chapter 2. Technical report, Cambridge University Press, Cambridge, United Kingdom, 2007. ISBN: 9780521880091.

[7] D. M. Ginosar, L. M. Petkovic, and D. P. Guillen. Thermal stability of cyclopentane as an organic Rankine cycle working fluid. *Energy & Fuels*, 25(9):4138–4144, 2011.

[8] F. Heberle, M. Preißinger, T. Weith, and D. Brüggemann. Experimental investigation of heat transfer characteristics and thermal stability of siloxanes. In *Proceedings of 2nd International Seminar on ORC Power Systems*, pages 1–35, Rotterdam, The Netherlands, October 2013.

[9] W. M. Kays and A. L. London. *Compact heat exchangers*. McGraw-Hill, New York City, New York, 1984. ISBN: 9780070333918.

[10] J. Larjola. Electricity from industrial waste heat using high-speed organic Rankine cycle (ORC). *International Journal of Production Economics*, 41(1–3):227 – 235, 1995.

[11] National Paint and Coatings Association. *Hazardous Materials Identification System Implementation Manual*. J. J. Keller & Associates, Inc., Neenah, Wisconsin, 2001. ISBN: 1579439861.

[12] L. O. Nord and O. Bolland. Steam bottoming cycles offshore - Challenges and possibilities. *Journal of Power Technologies*, 92(3):201–207, 2012.

[13] Norske Oljemuseum. Oil and gas fields in Norway - industrial heritage plan - DRAUGEN. Website, March 2010. [accessed: 01/08/2014].

[14] S. Quoilin, M. V. D. Broek, S. Declaye, P. Dewallef, and V. Lemort. Techno-economic survey of organic Rankine cycle (ORC) systems. *Renewable and Sustainable Energy Reviews*, 22:168–186, 2013.

[15] Siemens AG. Industrial Steam Turbines - The comprehensive product range from 2 to 250 megawatts. Website, 2013. [accessed: 01/08/2014].

[16] Y. Tormodsgard. FACTS 2014 - The Norwegian petroleum sector. Technical Report Y-0103/15 E, Ministry of Petroleum and Energy, May 2014.

[17] C. Trapp and P. Colonna. Efficiency improvement in precombustion CO_2 removal units with a waste–heat recovery ORC power plant. *Journal of Engineering for Gas Turbines and Power*, 135(4):1–12, 2013.

Chapter 3

Methods

This chapter embeds the modeling instruments created to answer the research questions of this thesis. The method for the steady-state optimization of the bottoming cycle units is first introduced. This part introduces also the approach adopted to size the heat transfer equipment and to assess the economic potential of the waste heat recovery units. The dynamic model of the power system integrating one gas turbine with the organic Rankine cycle turbogenerator is then presented. Subsequently, the chapter discloses the features of the regulator based on the model predictive control. Finally, the last section is dedicated to the validation and verification of the steady-state and dynamic models.

3.1 Steady-state analysis

The present section exposes first the procedure used for the thermodynamic calculations in steady-state conditions of the bottoming cycle units presented in Section 2.3. Subsequently, the design methods for sizing the heat transfer equipment are outlined. The part-load models of the main plant components and the control strategies adopted for the waste heat recovery systems are then presented. The section concludes with an

overview of the correlations used to assess the economic feasibility of the alternative configurations. The aforementioned models were implemented using the Matlab language [34]. As regarding the fluid models, the exhaust stream is treated as a mixture of ideal gases. The thermodynamic and transport properties of water, air and organic compounds are calculated according with the models implemented in the open-source software developed by Bell et al. [3].

3.1.1 Thermodynamic state calculation

The design-point analysis commences with the thermodynamic cycle calculation for the power modules illustrated in Figures 2.4, 2.5 and 2.7. Such step is accomplished by applying the first principle of thermodynamics and the mass balance equation to each plant constituents. This yields the computation of the thermodynamic states at the inlet and outlet of each system component. For the sake of completeness, Figures 3.1(a), 3.1(b) and 3.1(c) illustrate the $T-s$ diagrams of one design candidate for each waste heat recovery technology. The nodes where the working fluid is in saturated conditions, i.e., nodes 3 and 4 in Figure 3.1(a) and 4, 5 and 9 in Figure 3.1(b), are not reported in the plant layouts. These nodes are located inside the once-through boiler and the shell-and-tube condenser, respectively. Liquid droplets may deteriorate the performance of the latter steam turbine stages (see point 6 in Figure 3.1(a)). The design-point isentropic efficiency $\eta_{\text{is,t}}$ is thus penalized employing a correction factor. This is expressed as a function of the steam moisture content at the turbine outlet X_6, see Cotton [12]. The wet isentropic efficiency $\eta_{\text{is,t,wet}}$ is expressed as

$$\begin{cases} \eta_{\text{is,t,wet}} = \eta_{\text{is,t}} - 2\,(1 - X_6) & 0.984 < X_6 < 1.0 \\ \eta_{\text{is,t,wet}} = \eta_{\text{is,t}} - 0.032 - 0.76\,[1 - (X_6 + 0.016)] & X_6 \leq 0.984\,. \end{cases} \tag{3.1}$$

An isobaric specific heat capacity of $1100\,\text{J}\cdot\text{kg}^{-1}\cdot\text{K}^{-1}$ is used for energy balance calculations involving the exhaust gases. The design-point temperature and mass flow rate of the exhaust stream exiting the gas turbine are set in accordance with Table 2.2.

3.1.2 Heat transfer equipment

The procedure for the heat exchanger design requires determining the surface area A by evaluating, through an iterative procedure, the overall heat transfer coefficient U,

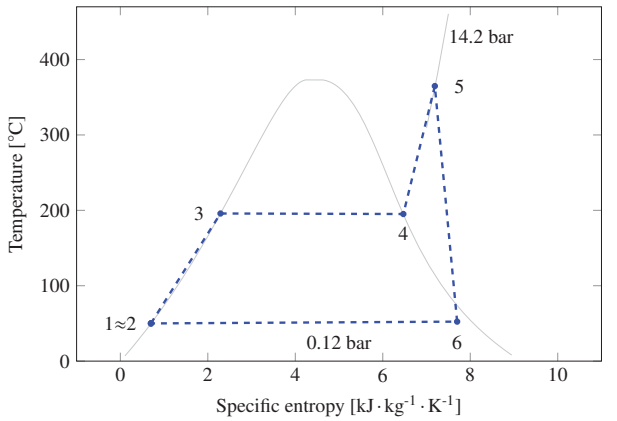

(a)

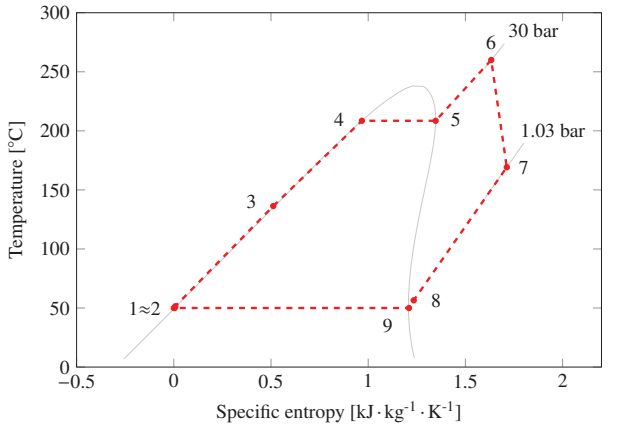

(b)

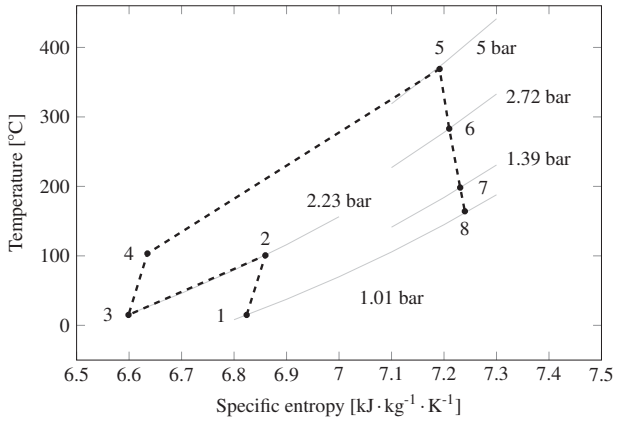

(c)

Figure 3.1: $T - s$ diagrams showing the thermodynamic cycle state points of one design candidate for each waste heat recovery technology. Isobaric lines are also reported and pressure drops are neglected. 3.1(a) $T - s$ diagram and saturation dome (water). 3.1(b) $T - s$ diagram and saturation dome (cyclopentane). 3.1(c) $T - s$ diagram for the ABC unit.

which reads

$$\frac{1}{UA} = \frac{1}{h_c A_c} + \frac{1}{h_{f,c} A_c} + R_{ct} + \frac{1}{h_h A_h} + \frac{1}{h_{f,h} A_h} \,, \tag{3.2}$$

where h is fluid film coefficient, and R_{ct} is the thermal conduction resistance. The subscripts "c" and "h" denote the cold and the hot side, while "f" refers to the fouling factor. The governing equation for the heat transfer across a surface is

$$\dot{q} = F_t \, UA \, \Delta T_{lm} \,, \tag{3.3}$$

where $\dot{q}$ is the heat rate, ΔT_{lm} is the logarithmic mean temperature difference, and F_t is the temperature correction factor. This variable accounts for co-current and cross-flow configurations. The standardized design procedure adopted for sizing the heat transfer equipment can be summarized in the following steps [13]

1. define main specifications, i.e., heat duties, inlet and outlet temperatures and mass flow rates,

2. evaluate physical properties, e.g., viscosity, density, thermal conductivity, etc.,

3. assume an initial guess value for the overall heat transfer coefficient U_0 and calculate F_t,

4. estimate the heat transfer area with Equation 3.3,

5. calculate the heat exchanger geometry,

6. compute the actual overall heat transfer coefficient U. In case U differs from U_0 by more than a certain tolerance, return back to step 4,

7. evaluate the pressure drops on both sides.

The design of the heat exchangers requires a precise estimation of the heat transfer coefficients. These variables strongly relate to the geometry and the physical properties of

the fluid. Therefore, the following three subsections present the correlations employed to compute the heat transfer coefficients and the pressure drops of each transfer device. Appendix A.1 includes the detailed list of equations.

The once-through boiler

Figure 3.2 illustrates the layout of the once-through boiler harvesting the exhaust heat from the gas turbines. The working fluid enters into the first rows of tubes on the exhaust gas outlet end. It is, subsequently, conducted by U-bends at each row to the hot inlet gas in a counter flow arrangement until it achieves the desired degree of superheating. A header collects the generated vapor which then proceeds to the turbine inlet. The working fluid is preheated and evaporated continuously within each of the parallel circuits. Gravity is not used to create the head. A centrifugal pump produces forced flow in the tubes so as to allow for both vertical and horizontal configurations. In brief, advantages compared to HRSGs are high flexibility, rapid response to load changes and easier operations during start-ups and low loads [22]. In OTBs, a thin-walled separator, not shown in Figure 3.2, replaces the function of the high-pressure drum of conventional heat recovery steam generators. This component enables to increase the tube diameter of the superheating section, and it is thus mandatory in steam Rankine engines due to the low density of the vapor. On the contrary, the separator and the intermediate headers are typically omitted using organic working fluids. This simplification is due to the shorter superheating section (see Figure 3.1(b)) and the relatively small difference between the specific volumes in liquid and vapor phase.

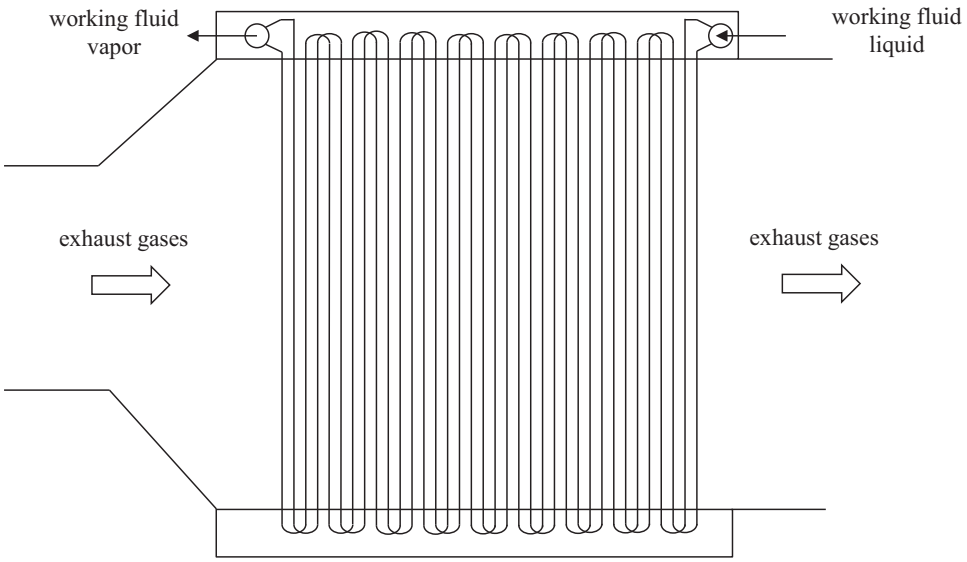

Figure 3.2: Layout of the once-through boiler. In the steam Rankine cycle unit, a thin-walled separator (not shown in the figure) replaces the function of the high-pressure drum of conventional heat recovery steam generators

The generic procedure outlined in Section 3.1.2 and implemented in accordance to Dumont and Heyen [16] is followed to design of the once-through boiler. Finned tubes are employed to enhance the heat transfer coefficient h_{h}, which is penalized by the high thermal resistance of the exhaust gases outside the tubes. This is modeled by replacing the heat transfer and the fouling coefficients on the hot side in Equation 3.2 with a term involving fin area and effectiveness. The heat transfer coefficient inside the tubes is assessed with the correlations proposed by Gnielinski [21] for sub-cooled liquid and superheated vapor. The heat transfer coefficient in the two-phase region is evaluated by discretizing the tubes into finite segments (50 elements are adopted) and applying the method proposed by Shah [44]. The gas-side heat transfer coefficient is computed using the approach proposed by Verein Deutscher Ingenieure [49], originally derived for air in circular finned-tube heat exchangers. The total pressure drops during evaporation are divided into three contributions: static, kinematic, and the one due to viscous friction. The three terms are evaluated using the equations proposed by Friedel [17] and Rouhani and Axelsson [42]. The correlation given by Haaf [23] is adopted for the pressure drops on the gas side. The equation is valid for banks of tubes in cross flow with plain transverse fins. It can be used for both staggered and in-line arrangements. A thermal conductivity of $0.0463\,\mathrm{W \cdot m^{-1} \cdot K^{-1}}$ and a density of $0.5763\,\mathrm{kg \cdot m^{-3}}$ are assumed for the exhaust gases.

The shell-and-tube heat exchanger

The condenser and the recuperator operating in the SRC and ORC modules are of the shell-and-tube type. Essentially, this device consists of a bundle of tubes surrounded by a cylindrical shell. The tubes are fitted into tube sheets at their extremes to separate the shell-side and tube-side fluids. Series of baffles are added to the shell to conduct the fluid flow and support the tubes, as shown in Figure 3.3(a). The tubes in the bundle are typically arranged in an equilateral triangular pattern, see Figure 3.3(b). The reader can refer to specialized textbooks, e.g., Coulson et al. [13], for a more complete description of this equipment. Shell-and-tube designers may select the Kern's bulk-flow method [28] or the Bell's procedure [4] to solve the design problem, see steps 1-7 in Section 3.1.2. The Kern's method does not account for bypass and leakage streams. However, it is simpler and accurate enough for preliminary design calculations [13]. This method is thus used in the present work.

The tubes of the ORC recuperator are equipped with fins to enhance the heat transfer coefficient on the shell side. Note that the fluid exiting the expander is in the superheated vapor state. The Nusselt number on the shell side is calculated using the equation reported in Coulson et al. [13]. The condenser model uses two distinct correlations as condensation occurs in both single- and two-phase regions. The approach reported in Coulson et al. [13] is adopted for the superheated vapor section. The heat transfer coefficient during condensation is computed as suggested by Kern [28]. The

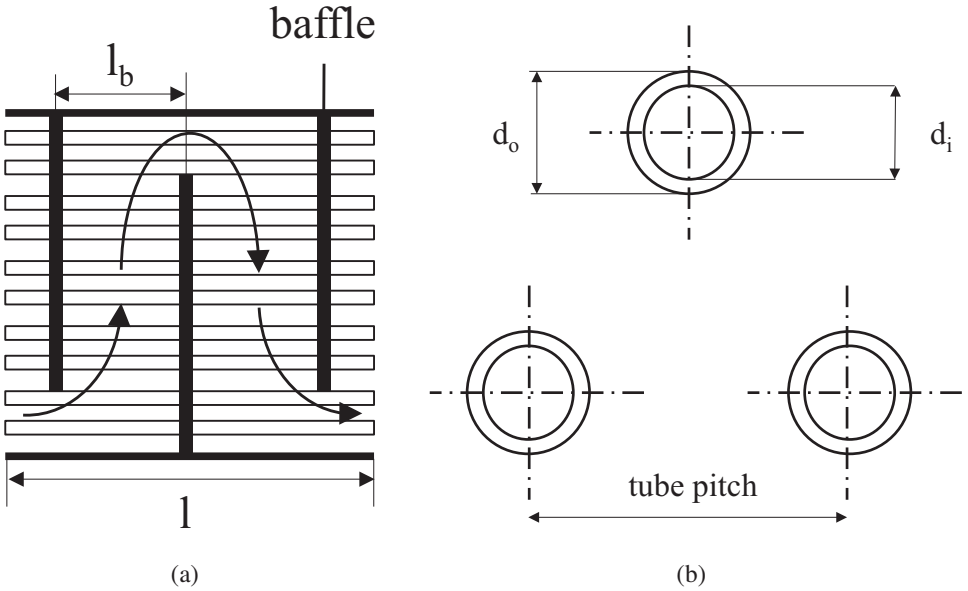

Figure 3.3: Layout of the shell-and-tube heat exchanger used for the condensation process and as recuperator in the organic Rankine cycle module. 3.3(a) Tube arrangement and shell flow pattern. 3.3(b) Triangular tube pattern.

sea-water heat transfer coefficient (tube side) is evaluated with the correlations proposed by Gnielinski [21]. The pressure drops in the single-phase regions are estimated according to Coulson et al. [13]. The friction losses on the condensing side are derived using the method proposed by Kern [28].

The finned-plate heat exchanger

The finned-plate heat exchanger serving the ABC power system consists of a stack of plates. The hot and cold fluids flow in the free space between the plates, typically in a cross flow arrangement, see Figure 3.4(a). The plates are equipped with a number of fins with the purpose of augmenting the surface area and attaining larger heat transfer area-to-volume ratios, i.e., high compactness. The use of high fin frequencies can enlarge the surface area by 5 to 12 times the primary transfer area [45]. The fins may have different shapes, e.g., wavy fins, offset fins and offset strip fins. The latter configuration (see Figure 3.4(b)) is the most widely adopted, and it is thus the one selected in the current work. It is worth mentioning that FPHEs can operate at lower pressures (8.3 bar) [45] compared to shell-and-tube heat exchangers and OTBs, depending on the process used to bond the metal plates. These limitations are not an issue for the present analysis, given the boundary conditions for the ABC unit (see Table 2.2).

The design approach is for this device the effectiveness – NTU method implemented as

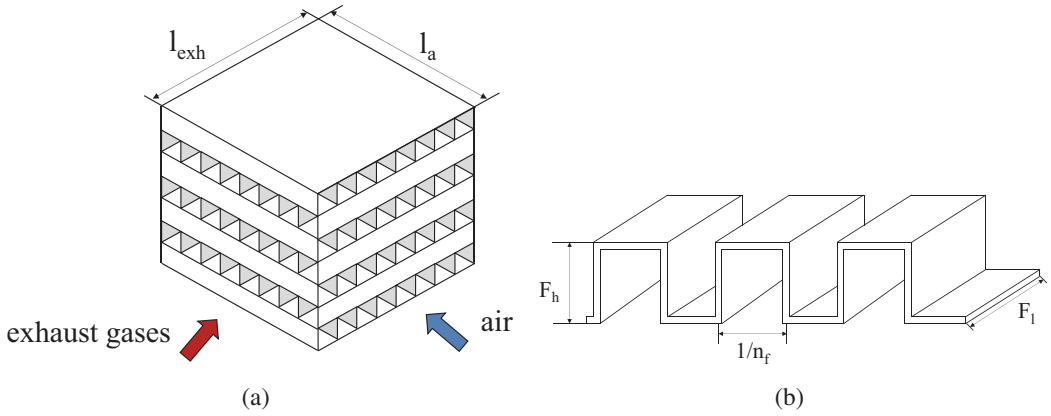

Figure 3.4: Layout of the finned-plate heat exchanger serving the air bottoming cycle power unit. 3.4(a) Exhaust gas and air flow pattern. 3.4(b) Details of the fin pattern.

reported in Yousefi et al. [51]. The heat transfer coefficients and the pressure drops on each side of the finned-plate heat exchanger are calculated in accordance to Manglik and Bergles [33].

3.1.3 Part-load models

The assessment of the part-load performance constitutes a crucial step of the design problem, see Section 1.2.1. It enables to estimate the total yearly CO_2 savings and to determine the economic feasibility of the alternative investments. For this purpose, the gas turbines are modeled using the data provided by the manufacturer. These cover the entire operating range of the engines (10 % to full load). The numerical data are replaced by interpolating functions, selected to ensure a compromise between computational cost and accuracy. The equations provide the fuel consumption, the temperature and the mass flow rate of the exhaust gases as a function of the engine load at constant ambient temperature (15 °C) and pressure (1.0132 bar). The coefficient of determination, measuring the discrepancy between the interpolating curves and the data points, is higher than 99.0 % for all functions. The gas turbine is thus considered as a black box model. The physical properties of the exhaust stream serve as inputs to the part-load model of the bottoming cycle unit.

For the once-through boiler, the intercooler, the ORC recuperator and the finned-plate heat exchanger, the heat transfer coefficients of the cold and hot side, in off-design conditions, are evaluated with the relation proposed by Incropera et al. [26]. In the once-through boiler and the shell-and-tube recuperator, the heat transfer resistance between the gas and the outer pipe surface is the dominant term. Therefore, the conductive term

and the heat transfer resistance of the cold stream are neglected in the part-load simulations. The condenser is trivially modeled as a fixed pressure component. This is justified considering the large availability of sea-water. This feature allows the cooling circuit to be controlled in such a way that the condenser pressure is nearly constant. The friction losses of the heat exchangers are lumped at the inlet of the component. A quadratic dependence with the volumetric flow rate is assumed.

The air compressors are modeled by employing the maps of axial machines provided with the commercial software developed by Kurzke [29]. These maps are represented by tables stating values for reduced flow, pressure ratio, isentropic efficiency and speed of revolution for the complete operating range of the component. The maps are scaled following the method proposed in Kurzke [30]. They can, in this way, represent the part-load characteristic of the compressors serving the ABC unit. The Stodola's cone law [46], expressing the relation between the pressure at the inlet and at the outlet of the expander with the mass flow rate and the turbine inlet temperature, is employed for the steam and air turbines. The expander is typically a one- or two-stage axial machine in megawatt-size ORC units. This leads to large pressure ratios across each stage. The flow is consequently supersonic at the outlet of the first stator. Therefore, the turbine is modeled as an equivalent choked de Laval nozzle. Its throat flow passage area is the sum of the throat areas of the nozzles constituting the first stator row. Isentropic expansion is assumed from the inlet section, where total conditions (i.e. total pressure $p_{T,6}$ and total temperature $T_{T,6}$) are assumed to be known by virtue of the thermodynamic state calculation, to the throat, where sonic conditions are attained, i.e., the flow speed equals the speed of sound c. The corresponding system of equations is

$$\begin{cases} s_6 = s(p_{T,6}, T_{T,6}) \\ h_{S,th} = h_{T,6}(p_{T,6}, T_{T,6}) - \frac{1}{2} c(h_{S,th}, s_6)^2 \\ \dot{m} = \rho_{S,th}(h_{S,th}, s_6) \cdot c(h_{S,th}, s_6) \cdot A_{th} \ , \end{cases} \tag{3.4}$$

where s_6 is the specific entropy at the turbine inlet. The subscript "S,th" indicates static conditions in the throat section. The continuity equation relates the mass flow rate through the nozzle $\dot{m}$ to the density $\rho_{S,th}$ and the flow passage area A_{th} in the throat section. The total nozzle throat area is known for given design-point conditions. The system of Equations 3.4 can be applied to relate the mass flow rate to the thermodynamic state at the turbine inlet.

The correlation relating the isentropic efficiency and the non-dimensional flow coefficient proposed by Schobeiri [43] is used to predict the turbine part-load performance. The isentropic efficiency of the pumps in off-design is derived using the method proposed by Veres [50]. The part-load characteristic of the electric generators is modeled

using the equation suggested by Haglind and Elmegaard [24]. Appendix A.2 reports the equations describing the off-design performance of the components constituting the bottoming cycle units.

3.1.4 Control strategies

The part-load characteristic of a combined cycle plant depends on the control strategy adopted for the topping unit and the waste heat recovery system. Unlike conventional combined cycle power plants, the SGT-500 compressors are not equipped with variable inlet guide vanes. The engine load can only be controlled by adjusting the fuel valve. As a consequence, the exhaust temperature drops down for decreasing loads. Consequently, it is decided to operate the SRC and ORC power modules in sliding-pressure mode. The evaporating pressures are governed by the system of Equations 3.4 and by the Stodola's cone law in the case of the SRC unit. A variable frequency electric motor regulates the rotational speed of the pump to keep constant the turbine inlet temperature. This strategy, currently used in ORC turbogenerators [11], ensures safe activities by tracking the hottest fluid temperature of the thermodynamic cycle. It is, instead, decided to maintain a constant superheating approach temperature difference for the SRC unit. As shown in Figures 3.1(a) and 3.1(b), the SRC turbogenerator may operate at higher turbine inlet temperatures compared to those of the ORC system. Operating the SRC unit at fixed turbine inlet temperatures could provide system configurations featuring an infeasible heat transfer process. This issue may occur at combined cycle loads where the exhaust gas temperature exiting the gas turbine approaches the steam turbine inlet temperature.

The pressure ratio and the rotational speed of the air compressors diminish with the load in the air bottoming cycle unit. This is the results of the interaction between the Stodola's equations and the compressor maps. The system does not present any degree of freedom. No decision on the operational strategy has to be taken. Preliminary calculations indicated that, for all the three technologies, the temperature of the exhaust gas stream exiting the primary heat exchanger remains at acceptable levels for combined cycle loads higher than 40 % of the nominal power. Hence, corrosion problems caused by the condensation of sulphuric acid vapor are avoided when operating at higher power duties. It is underlined that simple operational strategies are adopted for the design-point optimization. Section 3.4 presents a more advanced regulator based on the model predictive control.

3.1.5 Economic analysis

A feasibility study based on economic criteria requires to estimate the total capital investment (TCI) and compute the total revenue of such investment. The first step is accomplished by following the method described in Bejan et al. [2]. The procedure starts by evaluating the purchased-equipment cost (PEC) of the components constituting the bottoming cycle unit, and, subsequently, by incorporating the other direct costs (DC) and indirect costs (IC). The calculation terminates by estimating the total capital investment, whose breakdown is reported in Table 3.1. The installation of bottoming cycle units offshore does not require additional expenses related to the land and auxiliary facilities, e.g., fuel supply. The off-site costs are thus negligible.

Table 3.1: Breakdown of the total capital investment.

Total capital investment	
I. Fixed-capital investment (FCI)	
A. Direct costs	
Purchased - equipment costs (PEC)	
Purchased - equipment installation	15 %PEC
Piping	35 %PEC
Instrumentation and controls	12 %PEC
Electrical equipment and materials	13 %PEC
B. Indirect costs	
a) Engineering and supervision	4 %DC
b) Construction costs and contractor's profit	15 %DC
Contingencies	10 %(of a and b)
II. Other outlays	
Startup costs	4 %FCI
Working capital	15 %TCI
Costs of licensing, research and development	7.5 %FCI
Allowance for funds used during construction	7.5 %FCI

The purchased-equipment costs of the once-through boiler, the air compressors and the air turbines are acquired from Valero et al. [48]. The price of the pumps serving the SRC and the ORC power units and the cost of the electric generators are obtained from Lozano et al. [32] and Lian et al. [31], respectively. For the shell-and-tube heat exchangers and the FPHE, the cost is related to the heat transfer area using the equations reported in Hall et al. [25] and Genceli [19].

The ORC and SRC turbines considered in this work provide a similar range of power. On the other hand, the thermo-physical properties of the working fluids play a key role on determining the final design and the total expense. Consequently, the purchased-

equipment cost of the ORC expander is evaluated using the expression recently proposed by Astolfi et al. [1]. The equation was developed for multi-stage axial turbines employing organic vapors as working fluid. The price of the steam turbine is determined with the correlation reported in Lozano et al. [32]. The expense for the gear box serving the SRC module is assumed to be negligible compared to the other plant constituents. The equations for the component costs (see Appendix A.3) derive from different sources. Therefore, the PECs are adjusted for the same reference year (2014) using the historical price indexes reported in Table 3.2 [27].

Table 3.2: Price indexes and index factors for the calculation of the purchased-equipment costs. The reference price index is 233.916 (2014).

Year	Component	Price index	Index factor
1988	*shell-and-tube heat exchangers*	115.7	2.02
1993	*steam turbine, SRC and ORC pumps*	142.6	1.64
1994	*once-through boiler, ABC compressors and turbines*	146.2	1.60
1999	*finned-plate heat exchanger*	164.3	1.42
2010	*electric generators*	216.7	1.08
2014	*ORC turbine*	233.9	1.00

The profitability evaluation is carried out using the net present value (NPV) method, see Bejan et al. [2]. The bottoming cycle unit yielding the highest NPV is deemed to be optimal from an economic perspective. The net present value equation, specific to the power systems described in Section 2.3, reads

$$\mathrm{NPV} = \sum_{z=1}^{n} M_{\mathrm{f}} \frac{I_{\mathrm{CO_2}} + I_{\mathrm{ng}}}{(1+i)^z} - \mathrm{TCI}\,, \tag{3.5}$$

where $I_{\mathrm{CO_2}}$ and I_{ng} are the yearly incomes associated with the avoided CO_2 emissions and the fuel saving. Based on information provided by the platform operator, reasonable figures for the discount rate i and the life-time of the investment n are 6 % and 20 years. The factor M_f, equal to 0.9 [31], accounts for the operating and maintenance costs.

The incomes are assessed by computing first the yearly fuel consumption of two gas turbines providing 50 % load each. Secondly, the same quantity is evaluated for the novel configurations assuming that engine A feeds the bottoming cycle unit. The power

demand is also supported by gas turbine B. The last engine is on standby. It was decided to split the load so that in nominal operations the combined cycle unit provides 14 MW. Gas turbine B supplies the remaining 5 MW. Preliminary calculations proved that all three combined cycle technologies could cover alone the entire base-load power demand. This would allow to shut down gas turbine B. Nonetheless, this option is discarded as it would not permit to meet the necessary temperature level in the TEG circuit of HEX A, see Figure 2.5. The heat demand can be provided by HEX B operating gas turbine B at moderate loads, yet high enough the ensure a safe margin from surging and choking of the LPC compressor. Moreover, the proposed configuration facilitates maintenance activities. The platform operator can decide to stop the gas turbine serving the combined cycle unit, and replace its function with one of the remaining engines. The CO_2 savings $\Delta\dot{m}_{CO_2}$ can then be computed with the available fuel consumptions assuming a conversion factor of 2.45 $kg(CO_2) \cdot kg(fuel)^{-1}$. This figure was derived using the measured data from the Draugen platform.

Considering a fuel price (c_{ng}) of 0.68 $NOK \cdot Sm^{-3}$ and a carbon dioxide tax (c_{CO_2}) of 410 $NOK \cdot kg^{-1}$ [36], the two yearly incomes in Equation 3.5 can be expressed as

$$I_{ng} = 3.6\, c_{ng} v_{st} \Delta\dot{m}_{ng} h_u \,, \tag{3.6}$$

$$I_{CO_2} = 3.6\, c_{CO_2} \Delta\dot{m}_{CO_2} h_u \,, \tag{3.7}$$

where h_u is the capacity factor in $h \cdot yr^{-1}$, $\Delta\dot{m}_{ng}$ stands for the fuel savings, and c_{CO_2} is the price of natural gas. In Equation 3.6, v_{st} is the specific volume which, at 15 °C and 1.0132 bar, is equal to 1.314 $Sm^3 \cdot kg^{-1}$. The capacity factor is calculated assuming that the power system is halted due to maintenance activities for a period of two weeks per year (ZONE 3), see the duration curve reported in Figure 2.3. It operates at 25 MW (ZONE 1) and 19 MW (ZONE 2) for 14 % and 80 % of the time, respectively.

3.2 Dynamic modeling

This section outlines the features of a novel approach which aims at integrating the fulfilling of dynamic requirements in the preliminary design of power systems. The method, employed to address hypothesis iii), is also applicable to traditional power plant technologies. It consists of two main steps. Firstly, N performance metrics are

selected (e.g. the thermal efficiency, the overall system weight, the net present value). A multi-objective optimization problem is then defined employing the design models introduced in Section 3.1. This step enables to identify a set of preliminary plant designs which deliver the optimal steady-state metrics, typically given in the form of a N-dimensional Pareto front. In the second step, the dynamic performance of the system is assessed by simulating critical transients for each design candidate. Dynamic metrics, e.g., rise time and frequency tolerances, are measured to see if they satisfy requirements and constraints. The solutions which do not meet the dynamic standards are discarded.

The end-result of the procedure is a reduced set of optimal system designs complying with the trade-offs between different objectives, while ensuring proper operation during severe transients. This, in turns, allows plant designers to take properly informed decisions about the final system design. Moreover, they avoid the risk of discovering criticalities of transient operation at later project stages, i.e., during detailed design, or even commissioning, when corrective actions might be very expensive or impossible.

This section presents first the modeling language used for the transient calculations. It then describes the dynamic model of the plant consisting of one gas turbine and an ORC turbogenerator. This technology is, for the purpose of the transient analysis, the bottoming cycle unit under investigation. The selected working fluid of the ORC module is cyclopentane, see the results and the discussion given in Sections 4.1 and 5.1.

3.2.1 The modeling language

The second step of the design procedure requires the identification and simulation of critical scenarios involving system transients, e.g., sudden changes in the power demand, load rejections, or unit trips. A nonlinear dynamic model of the plant based on first principles is thus necessary. This should be implemented so that it can be parametrized from the optimal design candidates obtained in the first step of the procedure.

An effective manner to build it is to exploit the modularity of the Modelica language [18]. This enables an object-oriented approach to modeling as it uses advanced concepts such as inheritance, replaceability and reusability. These features facilitate the development of advanced models as pre-defined components (tubes) can be used as sub-components in more complex models (heat exchangers). Moreover, Modelica uses a declarative equation-based modeling approach. This allows to code declarative differ-

ential and algebraic equations. As a result, the user can avoid to manually convert the model to an ordinary differential equation by solving for the derivatives. The reader can refer to Fritzson [18] for a more comprehensive description of the Modelica language.

The library ThermoPower [10] is used and extended to characterize the components of the gas turbine and the ORC turbogenerator. The thermodynamic and transport properties of all working fluids involved in the dynamic models are calculated as for the steady-state analysis, see Section 3.1.

3.2.2 The gas turbine

Figure 3.5 shows the Modelica object diagram representing the layout of the twin-spool gas turbine. Compared to the components shown in Figure 2.2, this model includes a block for the control system (green rectangle), the inertias of the shafts, and a component accounting for the pressure losses in the combustion chamber. The input connection are: the air and fuel flanges (purple fill pattern circles) and the pins (blue triangles) measuring the load set-point, the frequency and the power output. The interfaces to the outside are: the exhaust gas flange (purple pattern circle), the electric power connector (red rectangle) and the control action pin (white triangle).

The part-load characteristic of the engine strongly depends on the compressors and turbines. Therefore, different methods to derive their off-design performance are tested. A decision on the best approach is taken by comparing the model results against the semi-empirical data provided by the gas turbine manufacturer, see Section 3.5.1. For the low and high pressure compressors, the approaches are: i) extrapolation, ii) map scaling, and iii) stage stacking analysis. The extrapolation method uses polynomial functions whose coefficients are selected by fitting the maps of existing machines. The expressions implemented are originally from Zhang and Cai [53]. The second approach is based on the procedure devised by Kurzke [30]. Published characteristics of compressors and turbines are used to estimate the part-load performance of other units with similar design-point specifications. At last, the stage stacking analysis uses generalized performance curves for each stage. This allows the compressor designer to predict the output variables of a given multi-stage machine [15].

The off-design characteristics of the turbines are evaluated with the global method introduced by Stodola [46] and Traupel [47]. The turbine stage is described as a nozzle using a set of algebraic equations, i.e., the Stodola's law. The isentropic efficiency can be calculated from the operating conditions using the method proposed by Schobeiri [43]. Appendix B describes in details the aforementioned methods.

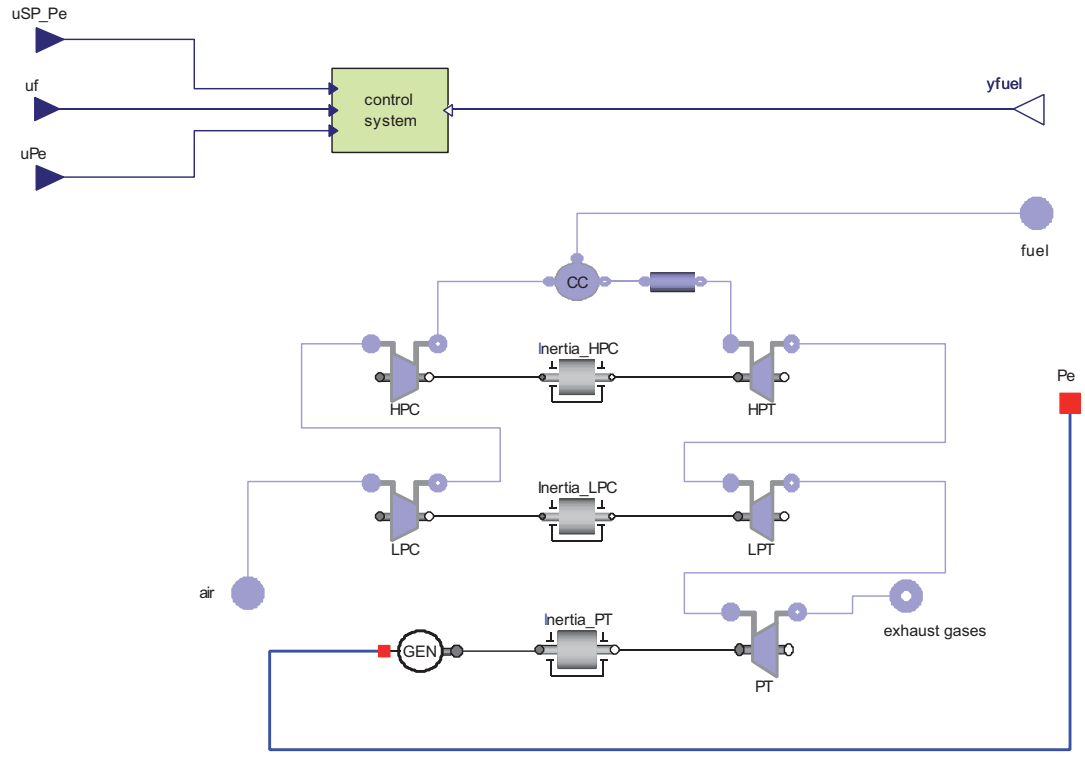

Figure 3.5: Modelica object diagram representing the layout of the twin-spool gas turbine installed on the Draugen platform.

The model of the combustion chamber assumes that mixing and chemical processes occur inside a constant volume, as suggested by Camporeale et al. [9]. The mass and the internal energy of the *plenum* are calculated using the thermodynamic properties of the combustion products at the outlet. Mass and energy dynamic balances are formulated by assuming complete combustion and no heat loss to the environment (adiabatic process). The pressure drops in the burner and at the inlet and outlet ducts are computed assuming a quadratic dependence with the volumetric flow rate. The mechanical connections (see Figure 3.5) between the compressors, shaft inertias, turbines, and generator connector allow to compute the variation of the angular speed of the three shafts. The values of the inertia of the rotating masses (shaft, blades, generator) and the volume of the combustion chamber are set according with the data provided by the gas turbine manufacturer.

Figure 3.6 shows that the control action of the gas turbines consists of two main contributions, i.e., the frequency and the droop deviation. At first, the frequency signal is filtered and compared to the set-point value (50 Hz), see the top leftmost of the figure. The difference is then measured and added to the contribution provided by the droop circuit. The latter determines the difference between the filtered signal containing the power output of the engine and the load set-point. A drooping factor of 0.125 is applied.

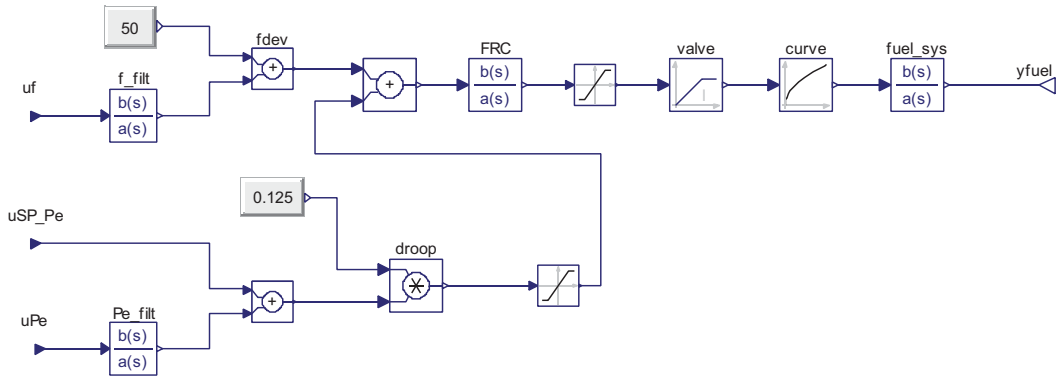

Figure 3.6: Modelica object diagram representing the control system of the twin-spool gas turbine as provided by the manufacturer.

The sum of the two signals passes to the frequency controller (FRC), and then to an integrator which sets the valve position (stroke). The characteristic curve of the orifice gives the actual fuel flow. Its injection is delayed by the *fuel_sys* block which accounts for the mechanic inertia of the valve. When running in parallel with other engines on stand-alone electric grids, one of the machines, i.e., the frequency-lead gas turbine, has both control actions activated. On the contrary, the remaining engines adapt their load according with the specified set-points through the droop circuit.

3.2.3 The organic Rankine cycle unit

Figure 3.7 shows the Modelica object diagram of the power system with gas turbine A and the ORC module. Note that the plant configuration does not show the remaining engines and the equipment providing the heat on board. The gas turbine model uses the sub-level diagram shown in Figure 3.5. The inputs for the control system and for the fuel and air are thus provided. Compared to the layout given in Figure 2.5, the object diagram includes the inertia of the ORC shaft, the components accounting for the pressure losses in the heat exchangers, and the blocks setting the thermodynamic states of the fuel and air. The proportional-integral (PI) controller (see the down leftmost side of the diagram) adjusts the pump speed to keep the temperature at the inlet of the expander constant. The power output required on board and load changes are specified with the input signal on the middle rightmost of Figure 3.7.

The models of the once-through boiler and the recuperator serving the ORC turbogenerator are implemented combining basic ThermoPower modules [10]. The hot side, the metal walls and the cold side are discretized by finite volumes. As shown in Figure 3.8, the tube wall model (middle) uses a one-dimensional dynamic heat balance

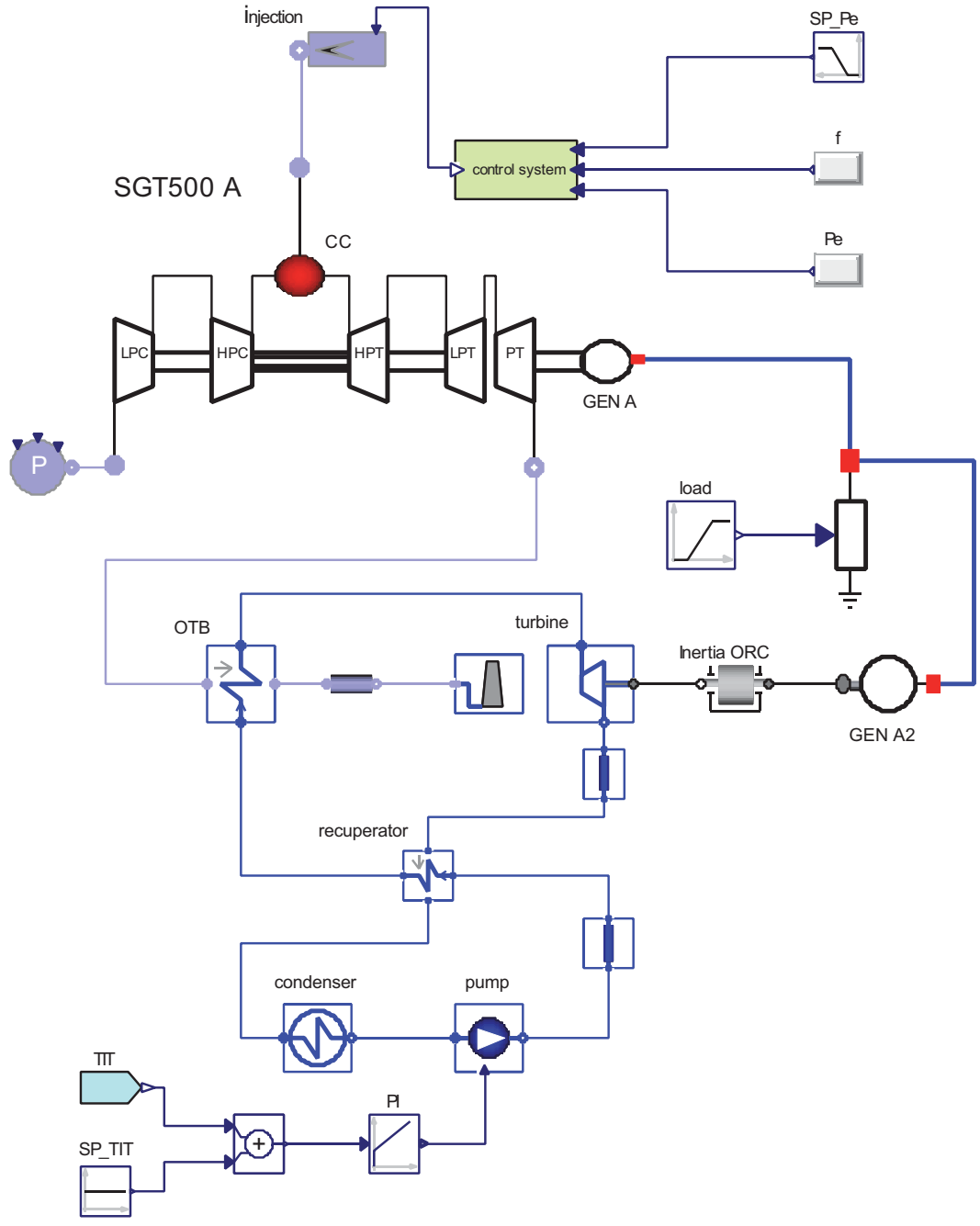

Figure 3.7: Modelica object diagram corresponding to the layout of the power system shown in Figure 2.5. The organic Rankine cycle module recovers the heat from gas turbine A. The engines B and C and the heat exchanger A are not reported for simplicity.

equation. The hot and cold flow models (top and bottom of the diagram) contain one-dimensional dynamic mass and energy balance equations. The exchange of heat is modeled with one-dimensional thermal ports (orange rectangles in Figure 3.8). The

counter-current model establishes the topological correspondence between the control volumes on the tube walls, and those of the gas flow model. The part-load characteristics of the turbomachinery, the heat transfer coefficients and the pressure drops are estimated as outlined in Section 3.1.3, see also Appendix A.2.

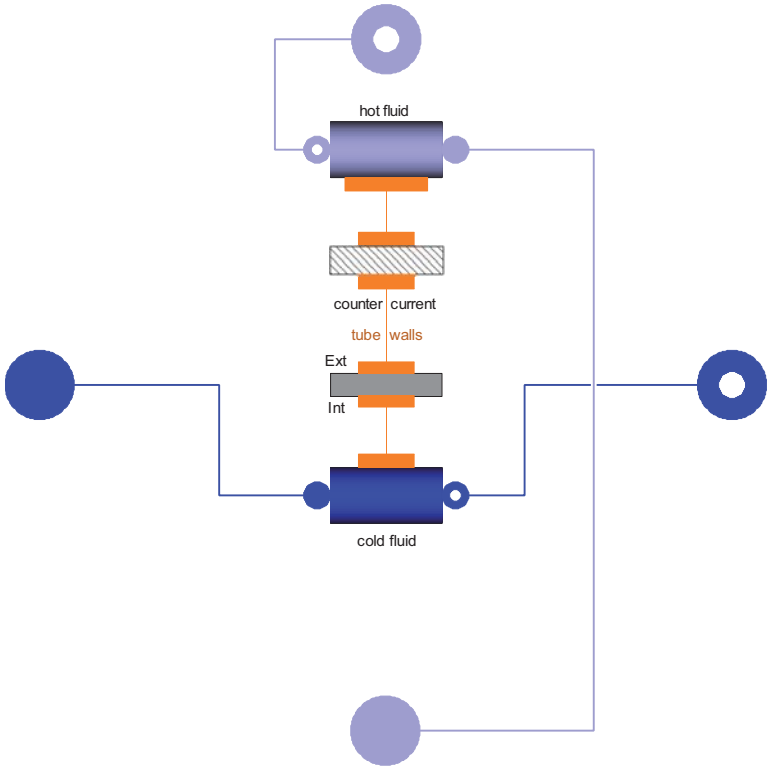

Figure 3.8: Modelica object diagram of the once-through boiler model.

The system under consideration operates off-grid, as explained in Chapter 2. When integrating the ORC unit, four synchronous generators are connected in parallel. They rotate at the same speed since the electrical connections are very short. The gas turbine exhibits the fastest load response. Therefore, it is used to control the network frequency (i.e. the rotational speed of the generators) using the feedback controller described in Section 3.2.2. Note that this system is embedded in the gas turbine package. Its parameters are neither modified nor tuned to cope with the presence of the ORC module. Assuming that gas turbine A and the ORC system are running in parallel with engine B, the most critical transient event for the combined cycle unit is the trip of gas turbine B. The rotational speed of the active generators drops during such event. The controller of gas turbine A responds opening the fuel valve to regain the reference frequency and to provide the new load set-point. Consequently, the exhaust mass flow rate and temperature rise. This leads to an increase of the temperature at the inlet of the ORC expander. The PI controller then counteracts by increasing the mass flow rate entering the OTB and the share of the load generated by the ORC system.

Preliminary simulations carried out with different designs of the system confirmed that the dynamic response of the ORC unit is far slower than that of the gas turbine. This phenomenon is observed even for aggressive designs of the PI controller. Moreover, the turbine inlet temperature is almost insensitive to the tuning of the ORC controller. Its peak is quickly reached due to the rapid response of the gas turbine. The mass flow rate through the turbine and the power output adapt slowly to the load, due to the large time constant of the bottoming cycle unit. This means that the contribution of the PI system to the limitation of the frequency drop is marginal. The ORC controller was thus tuned to obtain the minimum settling time of the controlled variable, avoiding the overshooting of the pump speed and pursuing well-damped responses for all involved variables. The calculations proved the feasibility of the tuning procedure when the proportional gain varies linearly with the weight of the once-thorough boiler. This procedure enables to account for the process gain variability with the design parameters, while maintaining the integral time at a suitable constant value.

3.3 The DYNDES tool

The DYNDES simulation program represents the *trait d'union* between the steady-state and the dynamic models presented above. The software is the present result of ongoing collaboration between the Technical University of Denmark and the Delft University of Technology (The Netherlands). Figure 3.9 shows the flowchart of the DYNDES tool. The software couples the steady-state and dynamic models to provide an integrated program for the optimal design of power systems, including dynamic criteria. The two computer programs are interfaced by means of shared files and command scripts. More in detail, the tool saves the results of the design optimization in an appropriate file. Then, the dynamic simulation program is run automatically to: i) extract information from the result file (e.g. the optimal designs relative to the geometry of the plant components), ii) convert the data into parameters and inputs for the dynamic models, iii) run the simulations, and iv) save the quantities of interest for further post-processing. Considering hypotheses i) - iii), the DYNDES tool constitutes the instrument to perform the steady-state optimization of the three power plant technologies. Furthermore, it enables to insert dynamic criteria in the design phase by virtue of the embedded interface with the dynamic simulator.

Given one of the three bottoming cycle units introduced in Section 2.3, the optimizer runs by acquiring first the array of the parameters. The upper and lower bounds limit the possible values for the vectors of the optimization variables $\boldsymbol{X}_{\mathrm{SRC}}$, $\boldsymbol{X}_{\mathrm{ORC}}$ and $\boldsymbol{X}_{\mathrm{ABC}}$, which at hand read

$$\boldsymbol{X}_{\mathrm{SRC}} = [p_5, \Delta T_{\mathrm{OTB}}, \Delta T_{\mathrm{c}}, T_{11}, d_{\mathrm{i,OTB}}, d_{\mathrm{i,OTB,sup}}, l_{\mathrm{OTB}}, Nt_{\mathrm{OTB}}, d_{\mathrm{i,c}}, l_{\mathrm{c}}, l_{\mathrm{b,c}}] \,, \tag{3.8}$$

$$\boldsymbol{X}_{\mathrm{ORC}} = [p_6, \Delta T_{\mathrm{r}}, \Delta T_{\mathrm{OTB}}, \Delta T_{\mathrm{c}}, T_{11}, d_{\mathrm{i,OTB}}, d_{\mathrm{i,OTB,sup}}, l_{\mathrm{OTB}}, Nt_{\mathrm{OTB}}, d_{\mathrm{i,r}}, l_{\mathrm{r}} \\ , l_{\mathrm{b,r}}, d_{\mathrm{i,c}}, l_{\mathrm{c}}, l_{\mathrm{b,c}}] \,, \tag{3.9}$$

$$\boldsymbol{X}_{\mathrm{ABC}} = [r_{\mathrm{c},1}, r_{\mathrm{c},2}, T_5, T_{11}, F_{\mathrm{h,a}}, nf_{\mathrm{a}}, F_{\mathrm{l,a}}, F_{\mathrm{h,exh}}, nf_{\mathrm{exh}}, F_{\mathrm{l,exh}}, Np_{\mathrm{exh}}, l_{\mathrm{exh}}] \,, \tag{3.10}$$

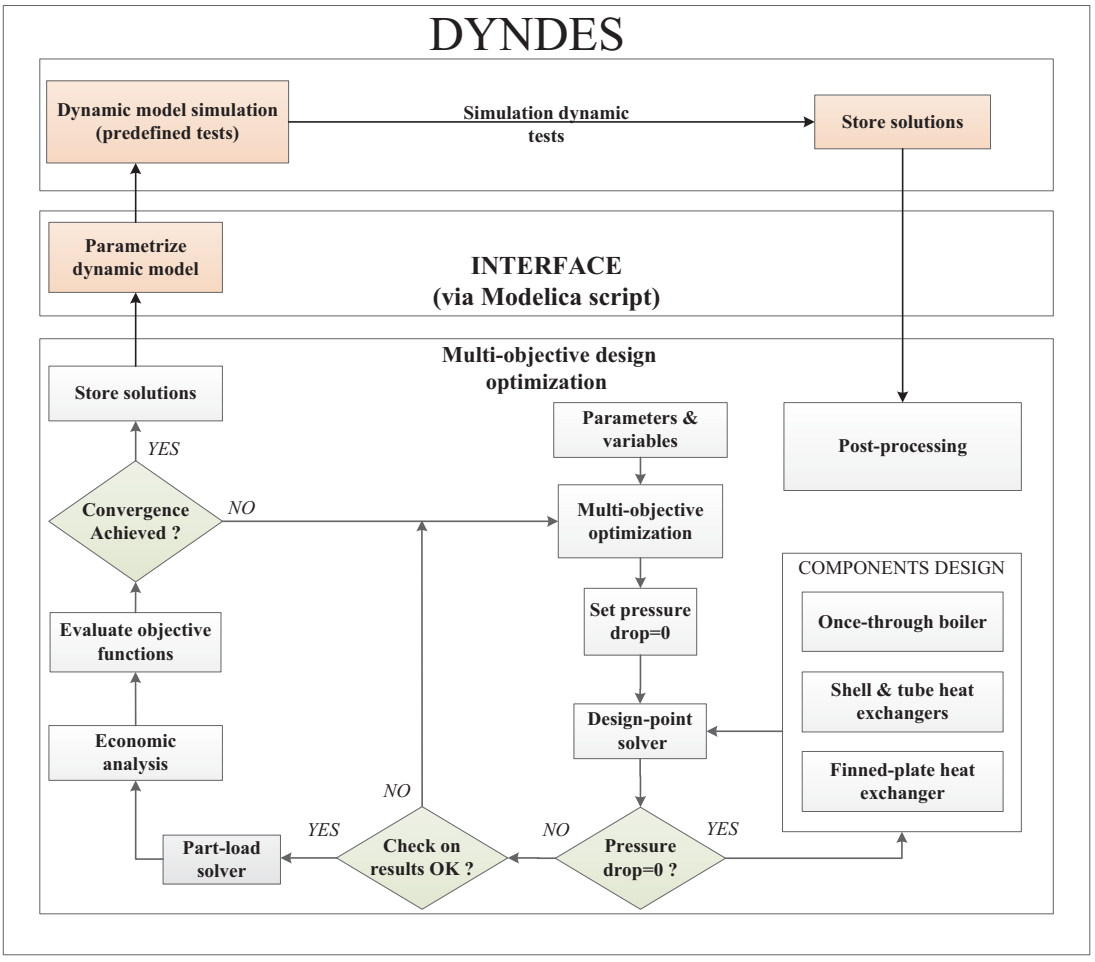

Figure 3.9: Architecture of the DYNDES simulation tool. The results of the design optimization are used as inputs for the dynamic simulations of the power system. The software integrates the steady-state and dynamic models via a scripting command.

where p_6 and p_5 are the turbine inlet pressures of the ORC and SRC units, T_{11} is the outlet temperature of the exhaust gases, and ΔT_c is the minimum temperature difference in the condenser. The quantity ΔT_{OTB} is the temperature difference between the two streams in the once-through boiler, at the location where the working fluid is in saturated liquid condition. The variable Nt_{OTB} is the number of tubes in parallel, while $d_{i,OTB}$ and $d_{i,OTB,sup}$ are the tube diameters of the preheater-evaporator and the superheater, respectively. The unknowns ΔT_r, l_b and l refer to the minimum temperature difference in the recuperator, the baffle spacing (given as a percentage of the shell diameter) and the length of the tubes. The subscripts "OTB", "r" and "c" denote the once-through boiler, the recuperator and the condenser. In Equation 3.10, $r_{c,1}$ and $r_{c,2}$ are the pressure ratios of the air compressors, and T_5 is the temperature at the inlet of AT2. The variables F_h, nf, F_l and Np are the fin height, the number of fins per meter, the fin length and the number of plates of the finned-plate heat exchanger. The subscripts "a" and "exh" refer to the air and the exhaust stream side.

The array of the objective functions $\boldsymbol{J}$ assumed in the present work is

$$\boldsymbol{J} = [W, m_{CO_2}, \mathrm{NPV}] \,, \tag{3.11}$$

where m_{CO_2} stands for the average daily CO_2 emissions of the power system being investigated. The metric W accounts for the weight of the bottoming cycle. This quantity is determined summing the weights of the heat exchangers. The latter function NPV is the net present value calculated as described in Section 3.1.5.

The multi-objective optimization uses a controlled elitist genetic algorithm to find for solutions which optimize simultaneously the three objective functions. Compared to gradient-based methods, a genetic algorithm is less prone to end its search in local minima of the problem, usually converging towards global optima. This, typically, comes at the cost of an increased computational effort, due to the large number of evaluation of the objective functions [14]. The parameters of the genetic algorithm are specified as follows: population size 1000, generation size 1000, crossover fraction 0.8, and migration fraction 0.2. These numerical values are selected to ensure the repeatability of the solution.

Table 3.3 lists the upper and lower bounds of the optimization variables. Note that the values related to the geometry of the heat exchangers are set accordingly to the

limits reported by Coulson et al. [13]. The upper and lower bounds are obtained from Yousefi et al. [51] for the FPHE serving the ABC unit. The minimum temperature of the exhaust gases exiting the once-through boiler is 140 °C, since the gas turbine can operate on a wide range of both liquid and gas fuels. Hence, the condensation of corrosive compounds is prevented, if other fuels (crude oil, heavy fuel oil and naphtha) than natural gas are combusted. The present work does not deal with supercritical ORC power modules. The upper bound for the turbine inlet pressure is set equal to 90 % of the critical value, depending on the working fluid under investigation, see Table 2.3.

Table 3.3: Lower and upper bounds for the multi-objective optimization variables of the three bottoming cycle units described in Section 2.3.

Variable	Lower bound	Upper bound
Turbine inlet pressure [bar]	5	$0.9 \cdot p_{cr}$
Pinch point recuperator [°C]	10	40
Temperature difference OTB [°C]	10	80
Pinch point condenser [°C]	10	50
Temperature at the AT2 inlet [°C]	250	350
Exhaust gas temperature [°C]	140	180
Inner diameter of the tubes [mm]	16	50
Length of the tubes [m]	1.83	7.32
Number of parallel tubes [-]	1	100
Baffle spacing [%]	20	120
Pressure ratios [-]	1.2	4
Fin height (FPHE) [mm]	2	50
Fin frequency (FPHE) [m^{-1}]	100	1000
Fin length (FPHE) [mm]	3	150
Number of plates (FPHE) [-]	1	200
Flow length gas side (FPHE) [m]	1.2	3

Table 3.4 lists the parameters which are maintained constant during the optimization. The geometry of the once-through boiler, the shell-and-tube recuperator and the finned-plate heat exchanger is retrieved from Dumont and Heyen [16], Coulson et al. [13] and Yousefi et al. [51], respectively. The condensing temperature of the working fluids in the SRC and ORC units is fixed to 50 °C. The risk of air infiltrations inside the piping from the surroundings is thus negligible.

The optimizer solves a design-point problem determining the thermodynamic states at the inlet and at the outlet of the components constituting the bottoming cycle unit. The pressure drops in the heat exchangers are initially set to zero. At this point, the design procedure of the heat transfer equipment (see Section 3.1.2) gives an estimate of the pressure drops and the component weights. The cycle calculation is thus run again considering the pressure losses in the heat exchangers. The results are then checked

Table 3.4: Parameters assumed for the multi-objective optimization.

Parameter	Value
Electric efficiency of the generators [%]	98
Ambient temperature [°C]	15
Ambient pressure [bar]	1.0132
Condensing temperature [°C]	50
Steam Rankine cycle	
Mechanical efficiency of the gear box [%]	99
Pump isentropic efficiency [%]	80
Turbine isentropic efficiency [%]	80
Organic Rankine cycle	
Working fluid	see Table 2.3
Pump isentropic efficiency [%]	72
Turbine isentropic efficiency [%]	80
Air bottoming cycle	
Air compressors isentropic efficiency [%]	87
Air turbines isentropic efficiency [%]	89.5
Coolant inlet temperature [°C]	5
Coolant outlet temperature [°C]	40
Once-through boiler	
Layout	in-line
Material	Stainless steel
Tube thickness [mm]	3.0
Longitudinal pitch [mm]	83
Transversal pitch [mm]	83
Fin pitch [mm]	4
Fin height [mm]	15
Fin thickness [mm]	0.4
Fin efficiency [%]	90
Recuperator	
Layout	triangular pitch
Material	Cupro-nickel
Tube pitch [-]	1.25
Tube thickness [mm]	3.0
Fin pitch [mm]	4
Fin height [mm]	15
Fin thickness [mm]	0.4
Fin efficiency [%]	90
Condenser	
Layout	triangular pitch
Material	Stainless steel
Temperature cooling water [°C]	5
Tube pitch [-]	1.4
Tube thickness [mm]	3.0
Finned-plate heat exchanger	
Material	Stainless steel
Fin and plate thickness [μm]	200

with respect to the first and second principle of thermodynamics. Furthermore, it is verified that the velocity on the hot and cold side of the heat exchangers lays within the ranges specified in Coulson et al. [13]. A lower limit of 84 % for the vapor quality at the steam turbine outlet must also be respected. If the test on the results is positive, the part-load simulation is performed using the models outlined in Section 3.1.3. Design-point constraints such as pinch points of heat exchangers and turbine inlet pressures are removed. The off-design characteristics of each component is a function of the operating conditions. The part-load solver computes the CO_2 emissions providing the inputs for the economic analysis. The process continues until the average change in the spread of the Pareto front is lower than the specified tolerance. A value of 10^{-3} is assumed.

The program stores the inputs of the dynamic models in a file when the multi-objective optimization ends. A scripting command then initializes the dynamic simulator. In this manner, the models are parametrized using the data for the heat exchangers and the turbine corresponding to the optimal bottoming cycle unit, as determined by the multi-objective optimization procedure. These models are then used to predict the dynamics of the complete system in a predefined transient scenario. Note that the number of dynamic simulations to be performed is equal to the number of points in the Pareto front. The dynamic test, conceived to assess the dynamics of the complete system, consists in the simulation of the failure of a gas turbine unit. This was defined according with the specifications of the platform owner. It represents the worst possible scenario the power system can possibly undergo without compromising the platform functionality. As mentioned in Section 3.1.5, the present study assumes that gas turbine A and the ORC unit run in parallel with engine B to provide the normal load (14 and 5 MW each). Gas turbine B trips at time t_0. The plant must take over the entire power demand until gas turbine C is ignited. Hence, the combined cycle unit undergoes a load set-point increment of $5.0\,\mathrm{MW}\cdot\mathrm{s}^{-1}$ (e.g. 5 MW in 1 s).

The process ends by storing the desired outputs of the dynamic analysis (e.g. the maximum undershooting of the network frequency) for each design candidate. Finally, post-processing is performed within the software environment for scientific computing.

3.4 The control system

The present section describes the implementation of the model predictive control. The final aim is to manage reliable and efficient electric power production on offshore installations, while pursuing a high plant flexibility, see also hypotheses iv) and v). The

dynamic model of the power system is programmed on a Simulink block-diagram environment [35]. The set of differential algebraic equations is equivalent to that of the Modelica models outlined in Section 3.2. However, additional programming efforts were justified, as the use of the Simulink language enabled the integration of the plant model with the commercial MPC toolbox [5]. The calculation of the thermodynamic and transport properties of the exhaust gases and the pure fluids is carried out as outlined in Section 3.1.

This section starts presenting the mathematical models of the gas turbine and the ORC turbogenerator. The bottoming engine uses cyclopentane as working fluid. After the description of the model predictive control, the section outlines the structure of the regulator.

3.4.1 Model description

The model of the topping unit derives from the original version belonging to the engine manufacturer. It uses non-physical transfer functions to represent the dynamics of the main gas turbine constituents, see Figure 3.10. The signal exiting the *fuel_sys* transfer function is the heat input to the engine. The heat rate is translated to the actual shaft power produced by the engine merely with a first order transfer function (*compressor*). This accounts for the inertia of the rotating masses, with the exception of the electric generators. The *exhaust gas* module provides the temperature and mass flow rate of the exhaust stream exiting the SGT-500 engine as a function of the ambient temperature and shaft power. In analogy to Section 3.1.3, the relations are based on interpolating functions covering a power range from 10 % to full load.

Figure 3.11 shows the top-level diagram of the plant with one gas turbine connected to the ORC turbogenerator. The mechanical powers of the two shafts are added together on the bottom right of the scheme. The sum is then subtracted to the load demand. Assuming small frequency deviations (≤ 5 %), the subsequent blocks convert the resulting signal to the frequency of the grid in per unit $\bar{f}$, adopting the following equation

$$\frac{d\bar{f}}{dt} = \frac{\dot{P}_{\text{out}} - \dot{P}_{\text{e}}}{2H} \,, \tag{3.12}$$

where H is the inertia constant of the rotating machines connected to the grid, $\dot{P}_{\text{out}}$ is the sum of the mechanical power of the gas turbine and the ORC unit, and $\dot{P}_{\text{e}}$ is the electric demand.

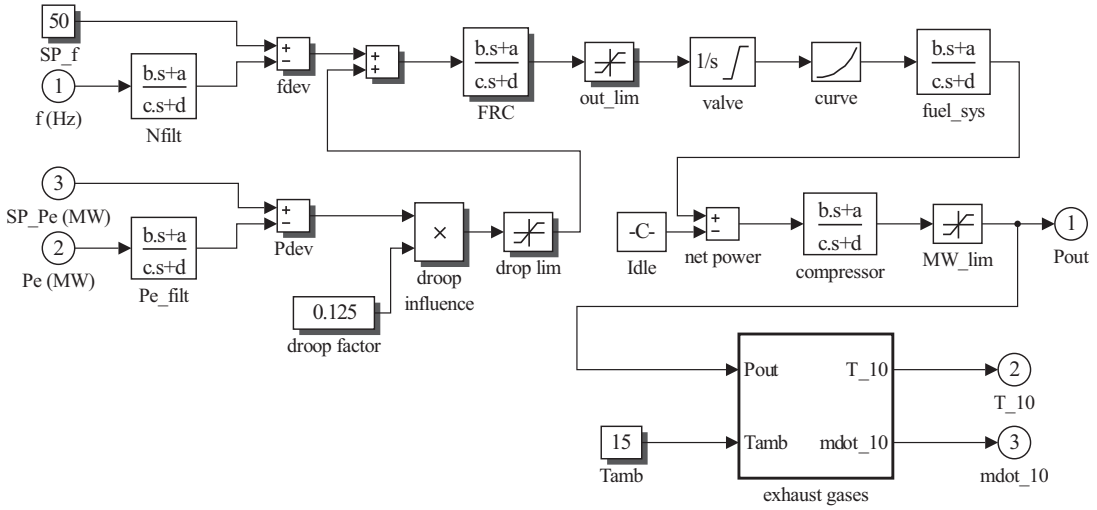

Figure 3.10: Transfer function model of the gas turbine on the Simulink block-diagram environment as provided by the manufacturer. Control system and power output of the engine.

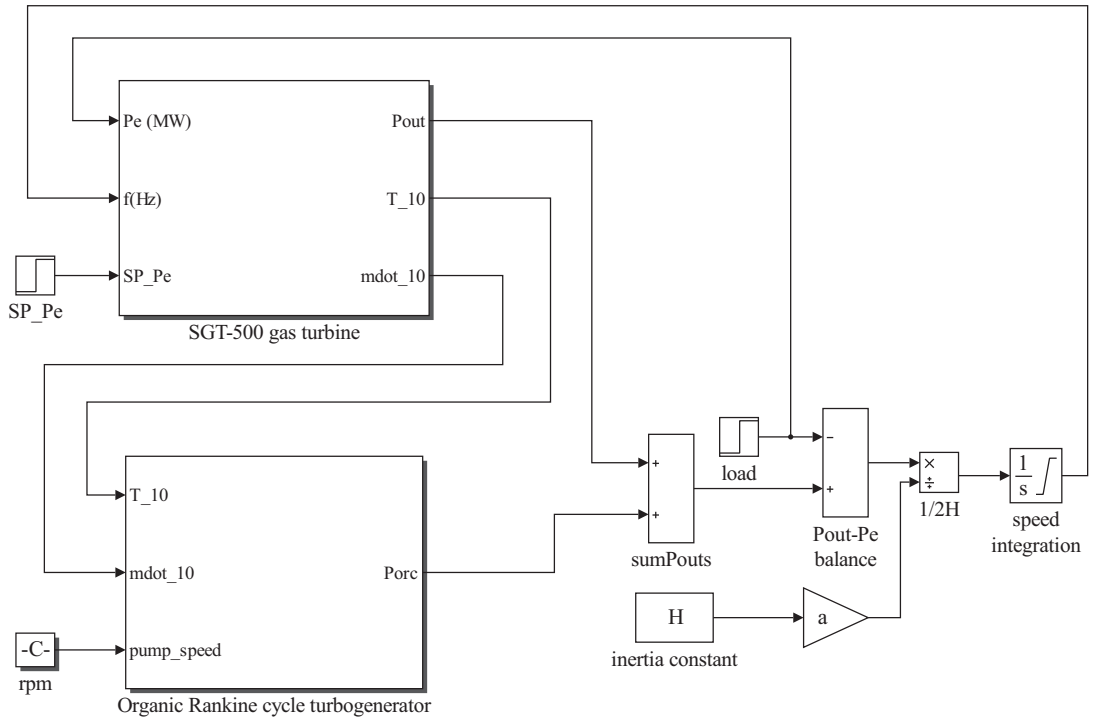

Figure 3.11: Top-level scheme of the gas turbine connected to the ORC power module on the Simulink block-diagram environment. The frequency of the grid is calculated using Equation 3.12.

The model of the ORC turbogenerator receives as inputs the temperature and the mass flow rate of the exhaust gases and the rotational speed of the pump. This variable is fixed in Figure 3.11. The ORC block is an extension of the part-load model developed in the Matlab language (see Section 3.1.3). The time-dependent terms are added to the steady-state energy and mass balances to account for the inertia of the system. The Matlab model is translated into the Simulink environment by exploiting the interpreted Matlab function block [35]. The transient performance of the ORC power system is considered to be driven only by the thermal inertia of the heat exchangers. Figure 3.12 shows the discretized model representing the once-through boiler and the recuperator. The model features a one-dimensional flow model for the hot side (top) and cold side (bottom), and a one-dimensional thermal model for the tube walls (middle). Counter-flow configuration and uniform pressure distribution are assumed.

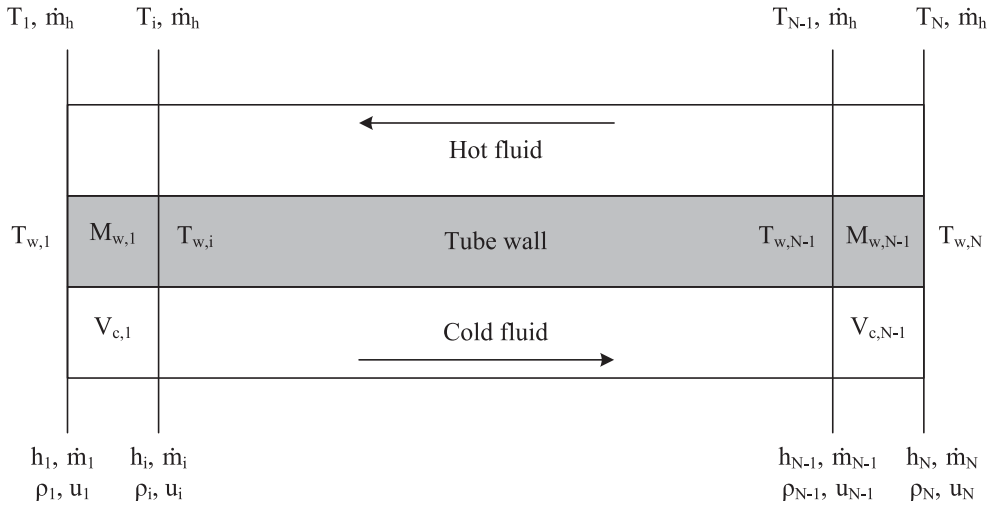

Figure 3.12: Heat exchanger discretized model.

The tube metal wall is modeled by a one-dimensional dynamic heat balance equation, which for the *i*th-cell can be written as

$$M_{\mathrm{w,i}}\, c_{\mathrm{w}} \frac{d\bar{T}_{\mathrm{w,i}}}{dt} = \dot{q}_{\mathrm{h}} - \dot{q}_{\mathrm{c}} \ , \tag{3.13}$$

where $M_{\mathrm{w,i}}$ and c_{w} are the mass and the heat capacity of the metal wall, and $\bar{T}_{\mathrm{w,i}}$ is the wall temperature at the *i*th-volume, calculated as the arithmetic average between the temperatures at the inner and outer node. The variable $\dot{q}_{\mathrm{h}}$ is the heat provided by the hot stream, and $\dot{q}_{\mathrm{c}}$ is the heat transferred to the cold side. The flow model for the cold side contains one-dimensional dynamic mass and energy balance equations, which can be expressed as

$$V_{\mathrm{c,i}} \frac{d(\bar{u}_{\mathrm{i}} \bar{\rho}_{\mathrm{c,i}})}{dt} = \dot{m}_{\mathrm{i}} h_{\mathrm{i}} - \dot{m}_{\mathrm{i+1}} h_{\mathrm{i+1}} + \dot{q}_{\mathrm{c}} \ , \tag{3.14}$$

$$V_{\mathrm{c,i}} \frac{d\bar{\rho}_{\mathrm{c,i}}}{dt} = \dot{m}_{\mathrm{i}} - \dot{m}_{\mathrm{i+1}} \ , \tag{3.15}$$

where $\dot{m}_{\mathrm{i}}$ and h_{i} represent the mass flow rate and the enthalpy at the ith-node. The variables $\bar{u}_{\mathrm{c,i}}$ and $\bar{\rho}_{\mathrm{c,i}}$ are the internal specific energy and the density of the volume $V_{\mathrm{c,i}}$, calculated as the arithmetic average between the values at the inner and outer node. Steady-state mass and energy balances are considered for the gas side, given the relatively small variations with time of the thermodynamic properties, see Equation 3.16.

$$\dot{q}_{\mathrm{h}} = \dot{m}_{\mathrm{h}} \, c_{\mathrm{p,h}} (T_{\mathrm{i+1}} - T_{\mathrm{i}}) \ . \tag{3.16}$$

The thermal resistance in the radial direction and thermal diffusion in the axial direction are neglected owing to their relatively small contributions. The overall heat transfer coefficient is assumed to be dependent on the hot side only. The heat transfer coefficient at the interface between the hot gas and the metal wall, in off-design conditions, is evaluated as proposed by Incropera et al. [26]. The condenser is considered a fixed-pressure component as outlined in Section 3.1.3. Appendix A.2 reports a full list of equations for the remaining components, i.e., pump, turbine and electric generator. Table 3.5 lists the parameters used to parametrize the state-space model of the ORC turbogenerator. The weight, volume and UA-values of the once-through boiler and the recuperator are set according with the design candidate with the highest net present value (see Figure 4.2).

The complete set of differential equations is approximated on a discretized domain by adopting a finite forward difference scheme. Considering, for instance, Equation 3.15, the finite difference estimation, derived from the Taylor series expansion truncated at the first order term, gives the following expression

$$V_{\mathrm{c,i}} \frac{\bar{\rho}_{\mathrm{c,i}}(t_{\mathrm{j}} + \Delta t) - \bar{\rho}_{\mathrm{c,i}}(t_{\mathrm{j}})}{\Delta t} = \dot{m}_{\mathrm{i}} - \dot{m}_{\mathrm{i+1}} \ , \tag{3.17}$$

where t_{j} is the time at which all state variables are known, and Δt is the sampling time. In this manner, the problem turns into an algebraic system of non-linear equations.

This is solved using a Newton's method scheme improved for robustness with the trust-region techniques developed by Rabinowitz [41].

Table 3.5: Design-point variables used to parametrize the state-space model of the organic Rankine cycle unit. The candidate, derived from the multi-objective optimization procedure described in Section 3.3, corresponds to the design with the highest economic revenue.

Component	Parameters
Once-through boiler	
Volume (cold side)	$8.5\,\mathrm{m}^3$
Weight (tube walls)	39.2 t
UA-value	$432.6\,\mathrm{kW}\cdot\mathrm{K}^{-1}$
Pressure drops (cold side)	103.1 kPa
Pressure drops (hot side)	1.0 kPa
Recuperator	
Volume (cold side)	$1.0\,\mathrm{m}^3$
Weight (tube walls)	8.8 t
UA-value	$167.7\,\mathrm{kW}\cdot\mathrm{K}^{-1}$
Pressure drops (cold side)	13.8 kPa
Pressure drops (hot side)[1]	41.5 kPa
Turbine	
Throat section	40.2 cm
Isentropic enthalpy drop	$116.94\,\mathrm{kJ}\cdot\mathrm{kg}^{-1}$
Electric generator	
Power output	5098.2 kW
Moment of inertia	$170\,\mathrm{kg}\cdot\mathrm{m}^2$
Pump	
Enthalpy rise	$6.51\,\mathrm{kJ}\cdot\mathrm{kg}^{-1}$
Volumetric flow	$0.0537\,\mathrm{m}^3\cdot\mathrm{s}^{-1}$

[1] The item includes also the pressure drops on the hot side of the shell-and-tube condenser.

3.4.2 The design

Figure 3.10 shows the feedback regulator on the Draugen platform . The control actions originate from information about past events. Improvements in the dynamic performance of the power system, as it is or with the ORC unit, can be attained by exploiting the model-based approach of the model predictive control. The regulator is design using the widely adopted toolbox described in Bemporad et al. [5], promptly implementable in a Simulink environment. Figure 3.13 shows the conceptual block-diagram of the model predictive control used to introduce the terminology. The scheme consists of two main blocks, i.e., the MPC and the power plant to be controlled. This is virtually

represented by the dynamic models described in Section 3.4.1. The main task of the MPC system is to hold the measured outputs (MOs) of the process, e.g., the frequency, at a reference value (or set-point) by acting on the manipulated variables (MVs), e.g., the valve position.

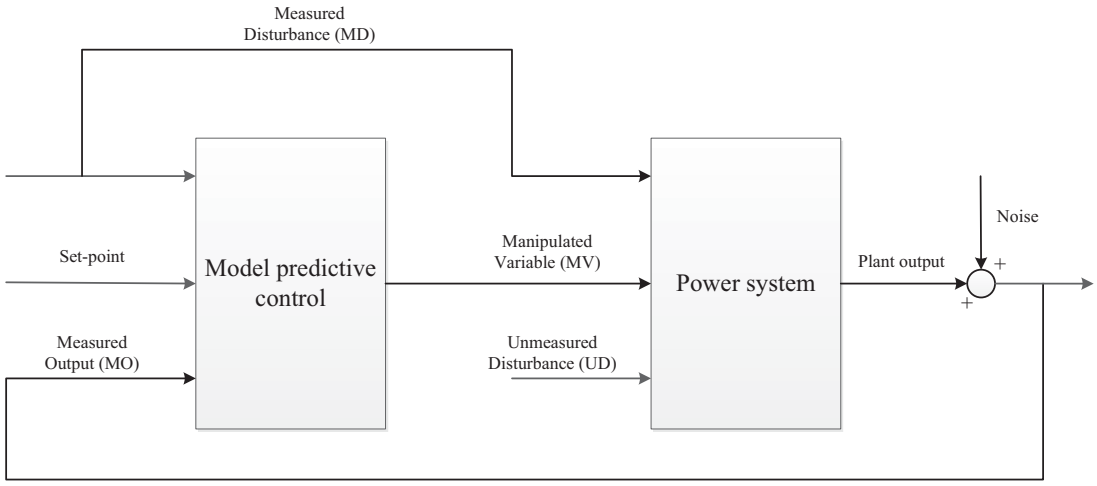

Figure 3.13: Generic block-diagram of the model predictive control including the terminology of the signals.

The second input affecting the actual performance of the power system is the unmeasured disturbance (UD). It accounts for all unknowns and unpredictable events that may perturb the plant operation. An example of UD in the ORC unit is fouling of the heat transfer equipment. On the contrary, a measured disturbance (MD) represents a gaugeable event (e.g. the variation of the power demand or ambient temperature), whose consequences can be predicted by the MPC. At this scope, the controller receives the MD signal as input (see Figure 3.13), thus enabling to directly compensate for the effect of the MDs on the MOs. Note that noise is added to the plant outputs to account for the inaccuracies of the measurements and for the measurement noise. The MPC requires the models relating the measured disturbances and the manipulated variables to each measured output. The higher the accuracy of the plant model, the faster the system responds to variations in MD. Considering the relatively low complexity of the power system, linear plant models derived with step response tests [8] are used.

The model predictive control action at time k is thus obtained by solving the following optimization problem [5]

$$
\begin{aligned}
&min\{J(\Delta \boldsymbol{u}, \epsilon)\} = \\
&\sum_{z=0}^{p-1} \left[\boldsymbol{y}(k+z+1|k) - \boldsymbol{r}(k+z+1)\right]^T \boldsymbol{Q} \left[\boldsymbol{y}(k+z+1|k) - \boldsymbol{r}(k+z+1)\right] \\
&+ \Delta \boldsymbol{u}(k+z|k)^T \boldsymbol{R}_{\Delta u} \Delta \boldsymbol{u}(k+z|k) \\
&+ \left[\boldsymbol{u}(k+z|k) - \boldsymbol{u}_{\text{target}}(k+z)\right]^T \boldsymbol{R}_u \left[\boldsymbol{u}(k+z|k) - \boldsymbol{u}_{\text{target}}(k+z)\right] + \rho_{\text{e}} \epsilon^2 ,
\end{aligned}
\tag{3.18}
$$

subject to the constraints

$$
\begin{cases}
\boldsymbol{u}_{\min} - \epsilon \boldsymbol{V}^u_{\min} \leq \boldsymbol{u} \leq \boldsymbol{u}_{\max} + \epsilon \boldsymbol{V}^u_{\max} \\
\Delta \boldsymbol{u}_{\min} - \epsilon \boldsymbol{V}^{\Delta u}_{\min} \leq \Delta \boldsymbol{u} \leq \Delta \boldsymbol{u}_{\max} + \epsilon \boldsymbol{V}^{\Delta u}_{\max} \\
\boldsymbol{y}_{\min} - \epsilon \boldsymbol{V}^y_{\min} \leq \boldsymbol{y} \leq \boldsymbol{y}_{\max} + \epsilon \boldsymbol{V}^y_{\max} \\
\Delta \boldsymbol{u}(k+z|k) = 0 \\
\epsilon \geq 0 ,
\end{cases}
\tag{3.19}
$$

where $\boldsymbol{y}$, $\boldsymbol{u}$ and $\boldsymbol{r}$ are the vectors of the measured outputs, the manipulate variables and the set-points, respectively. The integer p is the prediction horizon. The first term on the right side of Equation 3.18 represents the primary objective of the optimization, i.e., minimize the difference between the plant outputs and the reference points. The diagonal positive semi-definite matrix $\boldsymbol{Q}$ contains the weights on each set-point deviation. The second contribution in Equation 3.18 limits the velocity of the control action. If more MVs than MOs are available, the quantity $\boldsymbol{u}_{\text{target}}$ in the third term allows restricting the possible operating window of the MVs to conditions, which maximize, for instance, the economic revenue of the system. The slack variable ϵ supported by the weight ρ_{e} allows to adjust the impact of the constraint violations on the objective function J. In analogy to $\boldsymbol{Q}$, the diagonal and positive semi-definite matrices $\boldsymbol{R}_{\Delta u}$ and $\boldsymbol{R}_u$ weight the second and third term in Equation 3.18. The subscripts "min" and "max" refer to the lower and upper bounds on the manipulated variables and the measured outputs. The positive vectors $\boldsymbol{V}_{\min}$ and $\boldsymbol{V}_{\max}$ represent the concern for relaxing the corresponding constraint. The reader can refer to Bemporad et al. [5] for an in-depth description of the mathematical formulation of the optimization problem given in Equations 3.18 and 3.19.

Internal models - the gas turbine

The only available control action is the variation of the valve position. This quantity is, therefore, the manipulated variable in the diagram shown in Figure 3.13. The measured

output is the frequency of the electric grid. The most relevant measured disturbance is the platform load. Other sources, such as the ambient conditions, are not considered as they have a negligible contribution. Two step tests, performed at time $t_0 = 200\,\mathrm{s}$ in open-loop configuration, are necessary to relate the platform load and the valve stroke to the network frequency. The first test imposes a step change of the platform load (4 MW is assumed) at a fixed valve opening. The second one is performed by applying a step change of the stroke ($67.8 \cdot 10^{-3}$) at constant load. This procedure determines the two internal models of the MPC. The two transfer functions $W(s)$ are expressed as

$$W_{\mathrm{MD}\rightarrow\mathrm{MO}}(s) = \frac{-0.6966}{s}\,, \tag{3.20}$$

$$W_{\mathrm{MV}\rightarrow\mathrm{MO}}(s) = \frac{66.11\,s + 55.09}{s^3 + 3.73\,s^2 + 1.33\,s}\,, \tag{3.21}$$

where s is the complex argument of the Laplace transform. Figures 3.14(a) and 3.14(b) show the frequency trends over time of the *in silico* plant described in Section 3.4.1 and the transfer functions. Both step responses consist of an integrator part. Note that the normalized root mean square value is higher than 99.4 % for both transfer functions.

Internal models - the gas turbine and the ORC unit

The power system consists now of one gas turbine connected to the ORC turbogenerator. The degrees of freedom for the control logic are the valve position (MV_1) and the rotational speed of the pump (MV_2). This latter variable could be used to track different process variables related to the bottoming cycle module. For the reasons discussed in the section below, three alternatives are considered: i) the exhaust gas temperature T_{11}, ii) the degree of superheating $\Delta T_{\mathrm{sup}} = T_6 - T_5$, and iii) the turbine inlet temperature T_6. The measured disturbance is again the power set-point. The step changes of the load demand and stroke position are 2 MW and $25.3 \cdot 10^{-3}$, respectively. The transfer functions relating the measured disturbance and the first manipulated variable to the frequency are

$$W_{\mathrm{MD}\rightarrow\mathrm{MO}_1}(s) = \frac{-0.5350}{s}\,, \tag{3.22}$$

$$W_{\mathrm{MV}_1\rightarrow\mathrm{MO}_1}(s) = \frac{48.23\,s + 30.61}{s^3 + 2.64\,s^2 + 0.80\,s}\,. \tag{3.23}$$

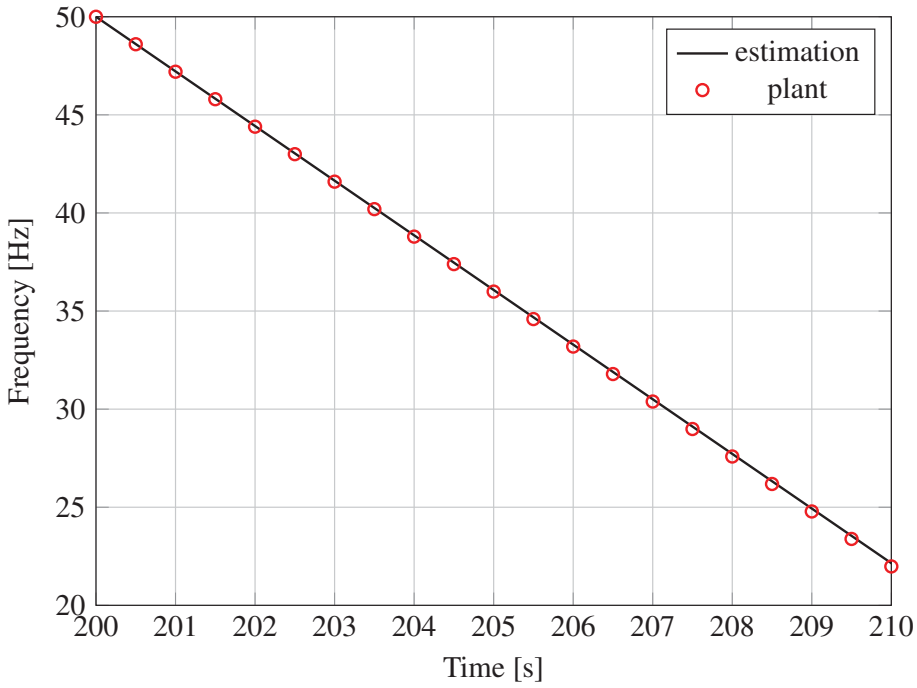

(a)

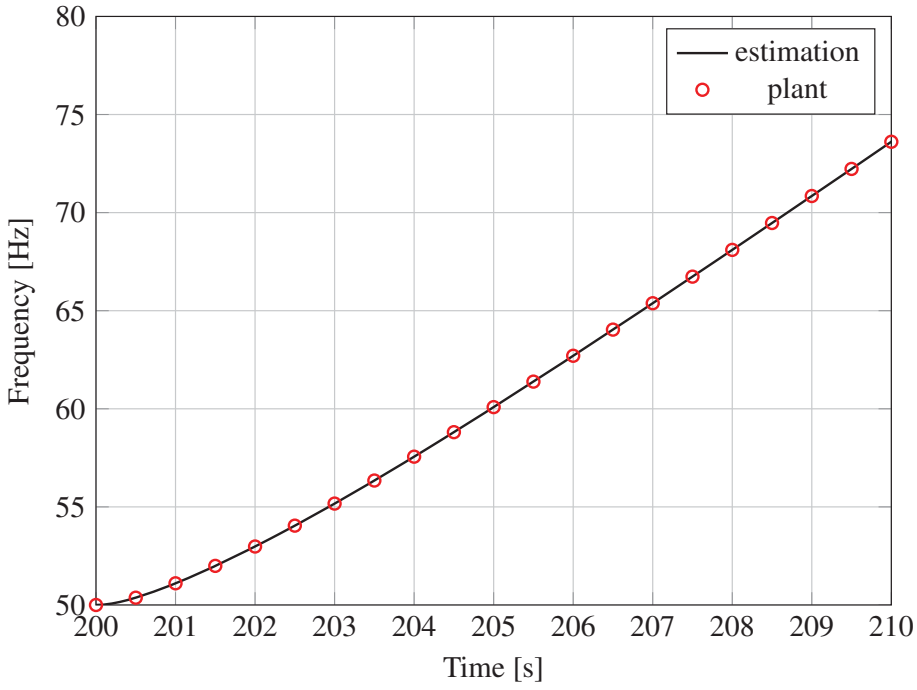

(b)

Figure 3.14: Plant response and transfer function. 3.14(a) Effect of the step change of the platform load (measured disturbance) on the frequency of the grid (measured output). 3.14(b) Effect of the step change of the valve position (manipulated variable) on the frequency of the grid (measured output).

Figure 3.15(a) shows the comparison between the frequency trends of the plant and the Laplace transforms for the two step tests (platform load and valve stroke). The normalized root mean square value is larger than 99.0 % in both cases. The expressions relating the pump speed to the other three measured outputs are evaluated assuming a step change of 300 rpm with the other inputs fixed. The transfer function for the temperature of the exhaust gases (MO_2) exiting the once-through boiler at hand reads

$$W_{MV_2 \rightarrow MO_2}(s) = \frac{-12.148 \cdot 10^{-3}\, s - 43.300 \cdot 10^{-3}}{s^2 + 28.905\, s + 0.843} \,. \tag{3.24}$$

Figure 3.15(b) shows the trends of the exhaust temperature T_{11} for the model outlined in Section 3.4.1 and the Laplace transform. The time when the change of the pump speed occurs is 200 s. As regarding the remaining measured outputs, the transfer functions for the degree of superheating (MO_3) and the turbine inlet temperature (MO_4) can be written as

$$W_{MV_2 \rightarrow MO_3}(s) = \frac{3.751 \cdot 10^{-3}\, s^2 - 1.348 \cdot 10^{-3}\, s - 6.968 \cdot 10^{-5}}{s^3 + 0.200\, s^2 + 46.599 \cdot 10^{-3}\, s + 8.961 \cdot 10^{-4}} \,, \tag{3.25}$$

$$W_{MV_2 \rightarrow MO_4}(s) = \frac{4.652 \cdot 10^{-3}\, s^2 - 2.086 \cdot 10^{-3}\, s - 8.553 \cdot 10^{-5}}{s^3 + 0.223\, s^2 + 46.028 \cdot 10^{-3}\, s + 8.603 \cdot 10^{-4}} \,. \tag{3.26}$$

Figures 3.16(a) and 3.16(b) show the time variation of the degree of superheating and the turbine inlet temperature for the plant and the Laplace transforms. Compared to the first measured output (i.e. grid frequency), higher order terms are required in the numerators to minimize the normalized root mean square value. This value is higher than 92.9 % for Equations 3.24 - 3.26.

It is underlined that the complete design of the MPC requires determining the relations between the pump speed and the frequency of the grid. Three transfer functions for the valve position and the other measured outputs are also necessary. However, as explained in Section 3.2.3, the control problem can be split in two sub-problems by virtue of the different time constants of the topping and bottoming engines. The primary task is to satisfy the platform load and regain rapidly the frequency set-point. This step can be accomplished using the fuel valve. No significant contribution can come from the pump speed due to the inertia of the ORC turbogenerator. On the other hand, the latter variable can deliver set-points for the process variables of the ORC engine (i.e. the

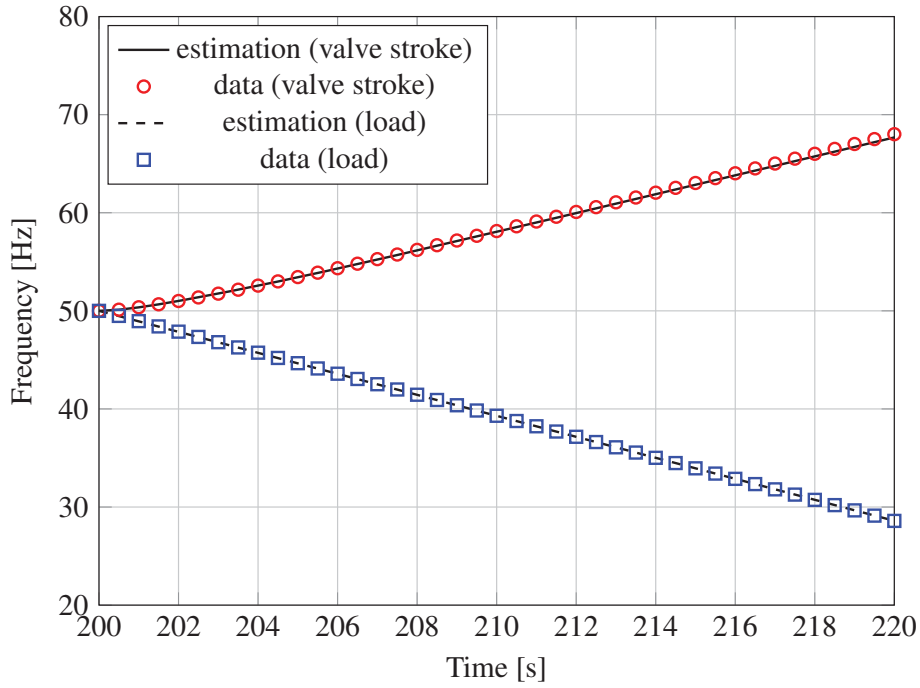

(a)

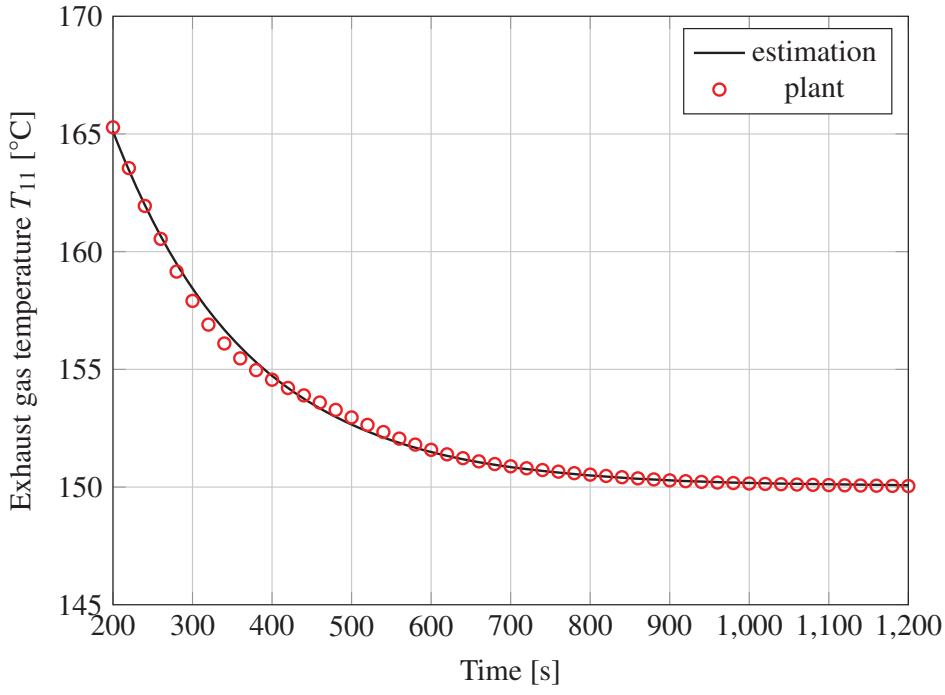

(b)

Figure 3.15: Plant response and transfer function. 3.15(a) Effect of the step change of the platform load (measured disturbance) and valve position (1st manipulated variable) on the frequency of the grid (1st measured output). 3.15(b) Effect of the step change of the pump speed (2nd manipulated variable) on the exhaust gas temperature T_{11} (2nd measured output).

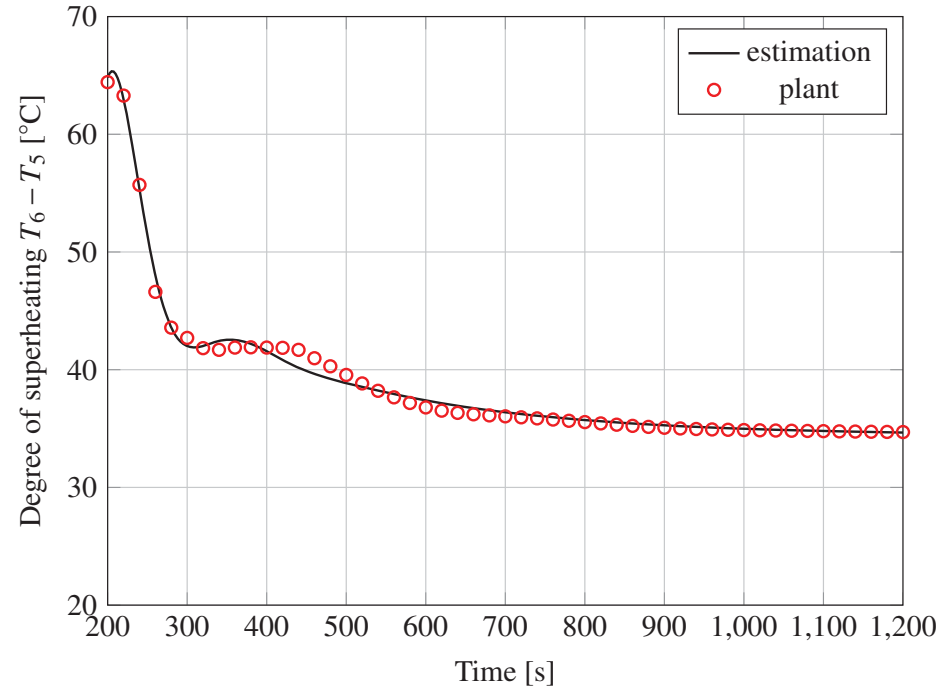

(a)

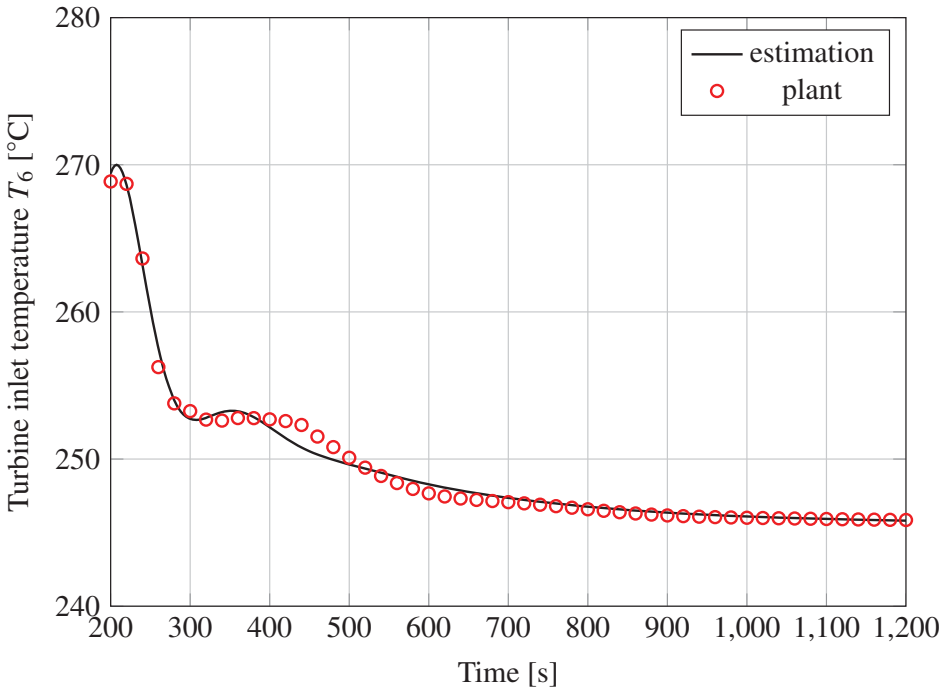

(b)

Figure 3.16: Plant response and transfer function. 3.16(a) Effect of the step change of the pump speed (2^{nd} manipulated variable) on the degree of superheating ΔT_{sup} (3^{rd} measured output). 3.16(b) Effect of the step change of the pump speed (2^{nd} manipulated variable) on the turbine inlet temperature T_6 (4^{th} measured output).

degree of superheating), with negligible impact on the valve position. These considerations led to set null-transfer functions for the valve position and the measured outputs related to the ORC module, as well as for the pump speed and the grid frequency. This implementation prevents the MPC to perform the regulation of the frequency using the pump speed, and to track a given turbine inlet temperature T_6 using the fuel valve.

The effect of the pump speed

The part-load and dynamic models of the power system outlined in Sections 3.1.4 and 3.2.3 imply the use of an electric motor. This device varies the pump speed to maintain a constant turbine inlet temperature. On the other hand, recent investigations [39, 52] suggested the presence, at any given load, of an operating condition which maximizes the performance of the ORC module. Considering one gas turbine connected to the ORC unit, the thermal efficiency of the system can be defined as

$$\eta_{\text{th}} = \frac{\dot{P}_{\text{GENA1}} + \dot{P}_{\text{GENA2}} - \dot{P}_{\text{p}}}{\dot{m}_{\text{ng}}\, LHV} \,, \tag{3.27}$$

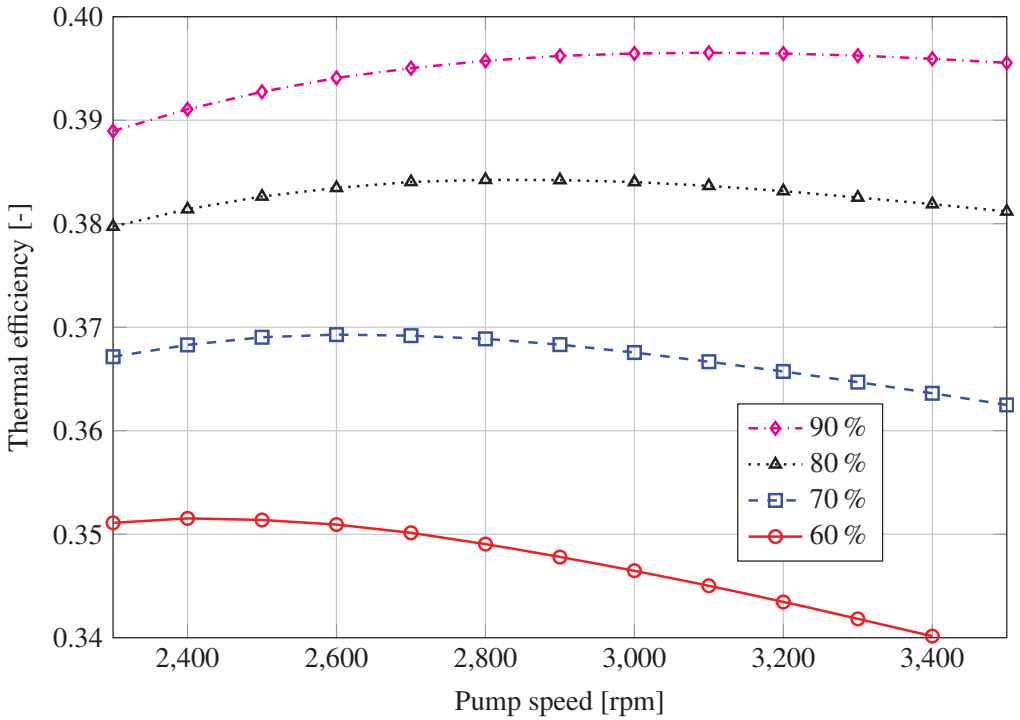

Figure 3.17: Effect of the pump speed on the performance of the power system (gas turbine and ORC unit). Plots relating the pump speed to the thermal efficiency at different load set-points expressed as a percentage of the nominal power.

where $\dot{P}_{\mathrm{p}}$ is the pump power consumption. The quantities $\dot{P}_{\mathrm{GENA1}}$ and $\dot{P}_{\mathrm{GENA2}}$ are the powers produced by the electric generators serving the gas turbine and the ORC unit, see Figure 2.5. The variables $\dot{m}_{\mathrm{ng}}$ and LHV are the mass flow rate and the lower heating value of the combustible. If the pumping work is negligible, the load demand fixes the value of the numerator in Equation 3.27. The system presents only the fuel input as degree of freedom at a given pump speed. The power shares of the topping unit and the ORC module are unique function of the valve position. If the pump speed is controlled to maximize the power produced by the bottoming module, the energy conversion efficiency of the combined cycle plant is at its maximum. The fuel consumption is minimized. Figure 3.17 shows the effect of the pump speed on the thermal efficiency of the combined cycle plant at different load set-points. The higher the power duty the larger the thermal efficiency and the pump speed maximizing the system performance.

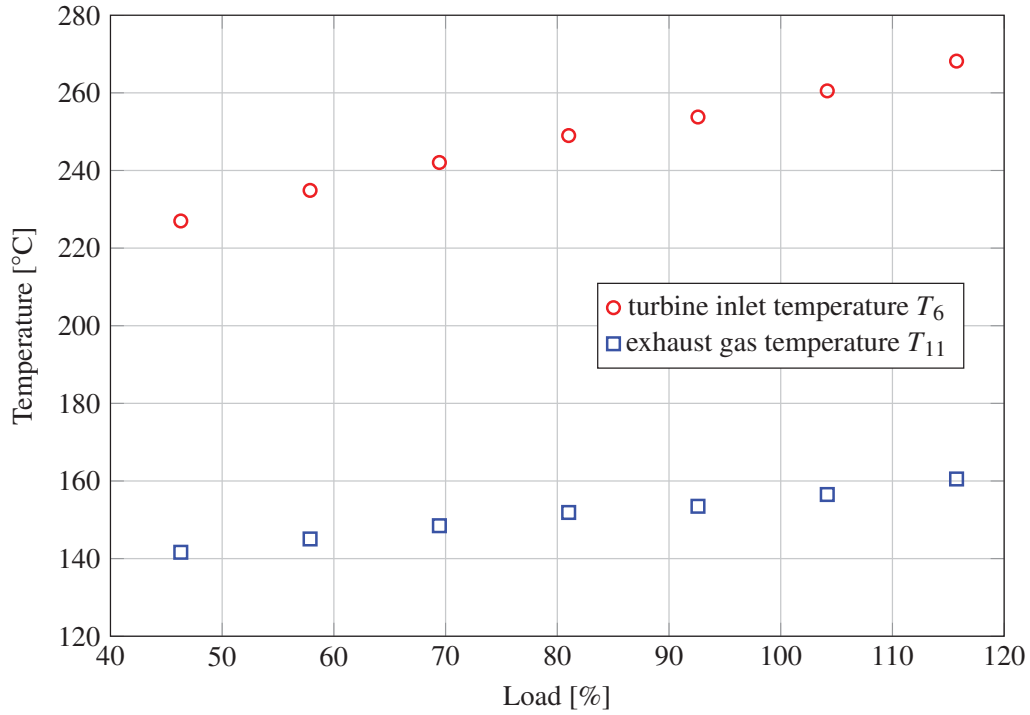

Figure 3.18: Turbine inlet temperature T_6 and exhaust temperature T_{11} as a function of the combined cycle load in percent. The rotational speed of the pump is set to the optimal value.

Preliminary calculations indicated that, when operating at the optimal pump speed, the ORC process is characterized by a relatively low degree of superheating ($\approx 35\,^{\circ}\mathrm{C}$). Fast load changes may lead the working fluid to enter the expander in vapor-liquid conditions. This event may damage the turbine blades owing to the formation of liquid droplets at the first turbine nozzle. To tackle the problem, the degree of superheating is the process variable used to follow the efficiency peaks. This choice allows to exploit

the capability of the MPC to handle hard constraints on the measured outputs. In such way, the control system can ensure that the organic compound enters the turbine in superheated vapor conditions, even during critical dynamic scenarios.

Figure 3.18 reports the steady-state trends of the exhaust temperature T_{11} and the turbine inlet temperature T_6 as a function of the load in percent. Note that the rotational speeds are set, in accordance with Figure 3.17, to achieve the optimal performance. The plot demonstrates that tracking the efficiency peaks at low duties ($< 40\,\%$) could lead to formation of acids in the terminal part of the once-through boiler. The problem is particularly harmful when other combustibles than natural gas are used to fire the SGT-500 engines. Moreover, demands exceeding the nominal power of the plant could increase the risk of working fluid decomposition. This event is due to the high temperatures reached by the fluid film in contact with the tube metal walls at the outlet of the OTB. In view of these operational problems, the MPC can also track the exhaust gas temperature T_{11} and the turbine inlet temperature T_6 with the linear models expressed by Equations 3.24 and 3.26.

3.4.3 The layout

Figure 3.19 shows the block-diagram of the MPC regulating the power system composed of one gas turbine connected to the ORC module. The MPC replaces the original

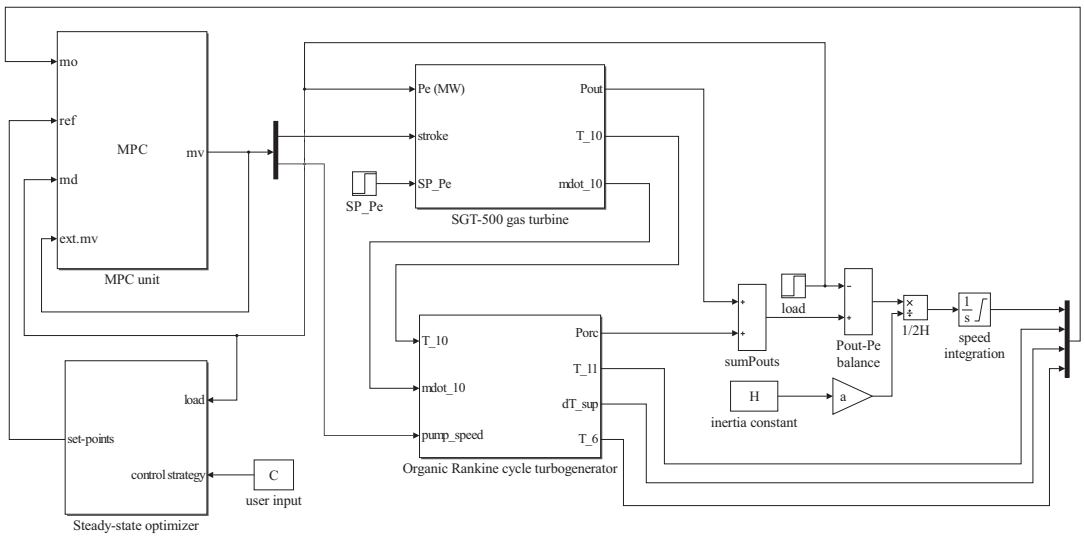

Figure 3.19: Block-diagram of the controller regulating the power system comprising one gas turbine and the ORC turbogenerator. The configuration includes the MPC and the steady-state optimizer. The latter block selects the operational strategy of the bottoming module.

control system, compared to the layout depicted in Figure 3.11. The regulator changes the valve stroke and the pump speed receiving as inputs the measured outputs and the load signal. The reference trajectories of the ORC unit are computed by the steady-state optimizer, shown at the bottom leftmost of the diagram. This component, activated by variations of the load set-point, uses a steady-state version of the plant model described in Section 3.4.1. Its task is to determine the plant configurations having the highest thermal efficiency. The optimizer solves an optimization problem with the rotational speed of the pump as variable. The mass flow rate of the fuel varies to satisfy the power demand. The algorithm is the simplex method for function optimization described in Nelder and Mead [37]. The optimizer commutes the control strategy to constant exhaust gas temperature, if the value T_{11} exceeds the limit for sulphuric acid formation. A limit of 140 °C is selected to preserve the fuel flexibility of the gas turbine. The same reasoning applies to the turbine inlet temperature, if the decomposition limit of

Table 3.6: Parameters, weights and bounds assumed to initialize the model predictive control unit.

Parameter[1]		**Value**
Sampling time [s]		0.5
Control horizon [s]		4
Prediction horizon [s]		20
Weight[2]		
Valve stroke rate [-]		0.1
Pump speed rate [-]		$2 \cdot 10^3$
Frequency [-]		1
Exhaust temperature [-]		$1.5 \cdot 10^3$
Turbine inlet temperature [-]		$5 \cdot 10^3$
Degree of superheating [-]		$1.5 \cdot 10^3$
Bound	**Minimum**	**Maximum**
Valve stroke [-]	0.145	0.6808
Valve stroke rate [s^{-1}]	-1.65	1.65
Pump speed [rpm]	1500	4000
Pump speed rate [$rpm \cdot s^{-1}$]	-10	10
Frequency tolerance [%]	-4	4
Exhaust temperature [°C]	140	-
Degree of superheating [°C]	5	-
Turbine inlet temperature [°C]	-	280

[1] For the operation of the gas turbine without the waste heat recovery unit the sampling time is reduced to 0.1 s. The prediction and control horizons are 20 s and 100 s, respectively. In accordance with the information provided by the engine manufacturer, the maximum limit for the valve stroke is set to 0.6608.

[2] The weights on the exhaust temperature, the degree of superheating and the turbine inlet temperature are set to zero depending on the operational mode selected for the organic Rankine cycle unit.

the working fluid is reached. Note that the platform operator has also the possibility to manually select the control strategy independently from the optimizer.

Table 3.6 lists the variables assumed to initialize the MPC. It is highlighted that the regulator and the ORC model act on a discrete domain with a sampling time of 0.5 s. Therefore, the blocks representing the gas turbine model and the continuous transfer functions disclosed in Section 3.4.2 are converted in the discrete domain. The control and the prediction horizons are defined considering the selected sampling time. The weights $r_{\Delta u\,i,i}$ and $q_{\mathrm{i,i}}$ of the matrices $\boldsymbol{R}_{\Delta u}$ and $\boldsymbol{Q}$ in Equation 3.18 are tuned. The scope is to ensure a compromise between well-damped responses of the measured outputs and rapid tracking of the reference trajectories. Note that the steady-state optimizer can switch the operational strategy of the ORC unit. For example, a constant exhaust gas temperature is selected by assigning the weight reported in Table 3.6 to the selected measured output (T_{11}), and imposing null-weights to the two other variables (T_6 and ΔT_{sup}). The third term in Equation 3.18 is not exploited in the present analysis as the number of MVs is lower than the available MOs. As for the bounds on the manipulated variables ($\boldsymbol{u}_{\min}$, $\Delta\boldsymbol{u}_{\min}$ and $\boldsymbol{u}_{\max}$, $\Delta\boldsymbol{u}_{\max}$) and on the measured outputs ($\boldsymbol{y}_{\min}$ and $\boldsymbol{y}_{\max}$), these are treated as soft constraints ($\boldsymbol{V}_{\min}$ and $\boldsymbol{V}_{\max}$ equal to 0). The numerical values are selected based on proprietary information provided by the gas turbine manufacturer and on data available in the open literature. Based on the experimental data devised by Ginosar et al. [20], the decomposition limit of cyclopentane is set to 280 °C.

3.5 Validation and verification

This section is dedicated to the validation and verification of the steady-state and dynamic models. At first, the validation of the gas turbine, performed using the information provided by the engine manufacturer and the platform owner, is described. The section concludes presenting the verification of the ORC dynamic and steady-state design models.

3.5.1 The gas turbine

Steady-state part-load performance

The dynamic model of the SGT-500 gas turbine outlined in Section 3.2.2 is verified, with respect to its steady-state part-load characteristic, by exploiting the engine curves

of the manufacturer. The Stodola's ellipse law and the correlation for the isentropic efficiency in Equation B.12 describe the off-design characteristics of the turbines. The part-load models of the burner and electric generator are those outlined in Section 3.2.2. The pressure drops at the inlet and outlet ducts are neglected. The results of three methodologies, i.e., the extrapolation method, the map scaling technique and the stage stacking analysis, are compared in modeling the compressors. The mean relative error (MRE) is the performance metric. The design-point parameters, e.g., the isentropic efficiencies, the pressure drops in the burner and the electric generator efficiency, are determined matching the design-point specifications provided by the manufacturer and the model results. Appendix C.1 gives the engine data and the trends of six variables as a function of the engine load for each modeling technique. The quantities are: the HPC outlet pressure, the HPT inlet temperature, the exhaust temperature, the exhaust mass flow rate, the fuel flow and the thermal efficiency .

Figure 3.20 shows the mean relative errors for the six engine variables. The quantities

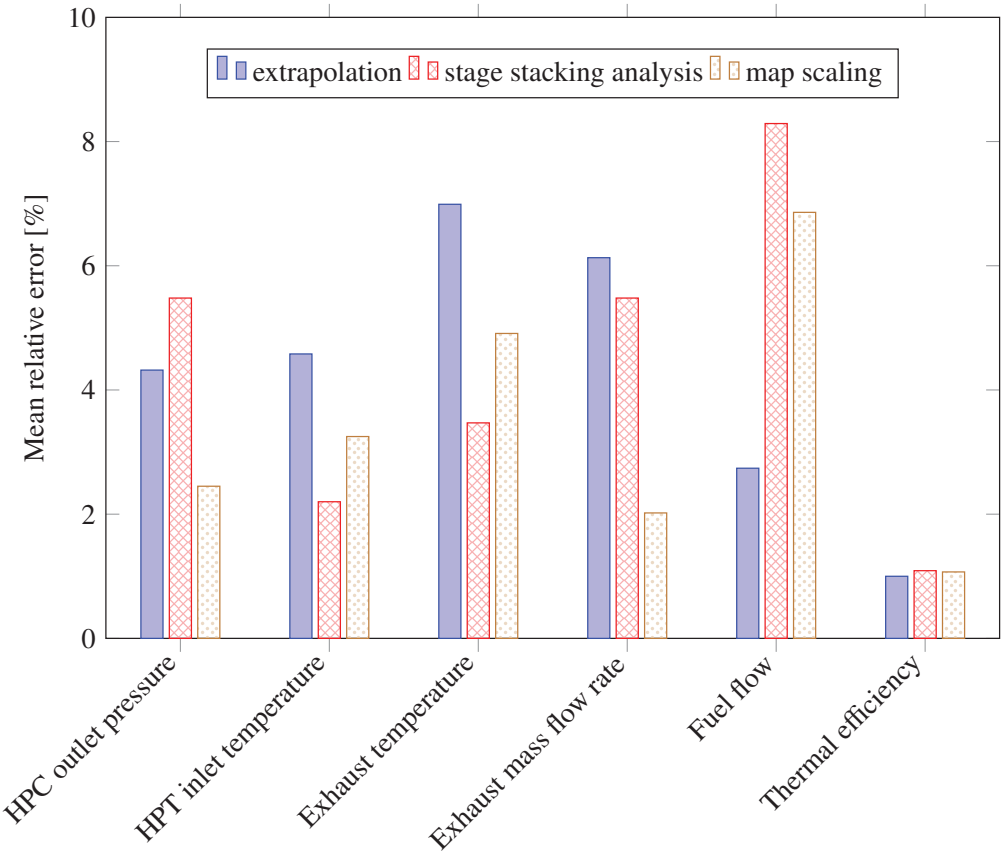

Figure 3.20: Mean relative error for the map scaling method, the stage stacking analysis and the extrapolation approach. The three methods refer to the compressor models. The turbines are modeled using the Stodola's law of the ellipse with variable isentropic efficiency.

giving the largest deviation ($\approx 8.0\,\%$) are the exhaust temperature and the fuel flow. The lowest discrepancy (1.0 %) is found assessing the thermal efficiency of the gas turbine. The extrapolation method exhibits poor performances (MREs higher than 6.0 %) in the estimation of the temperature and mass flow rate of the exhaust stream. The method is particularly inadequate at low loads, see Figures C.1 - C.6. The stage stacking analysis and the scaling map technique present both improved figures for the MREs. Larger deviations compared to the extrapolation approach occur computing the mass flow rate of the combustible. The error analysis demonstrates that the stage stacking method and the map scaling technique represent the most accurate methods to predict the part-load performance of the SGT-500 gas turbine. On the contrary, the extrapolation method is not appropriate, especially for low load calculations.

Dynamic characteristic

The operational data of the Draugen platform are used to assess the accuracy of the dynamic model of the gas turbine-based power system shown in Figure 2.2. The map scaling technique is used to model the compressors. The data were made available with all three engines in operation. However, the validation is performed by focusing on the operation of engine B with the purpose of limiting the amount of results. Nevertheless, the same methods are applicable to the other two gas turbines supplying the offshore facility. Gas turbine B operates initially at 45 % of the nominal power. The load then decreases first to 41 % in 10 s, and, subsequently, to 38 % in 20 s. The variables used for the comparison are the rotational speeds of the LPC and HPC shafts, the fuel flow, the PT outlet temperature, and the pressures at the outlet of the HPC and LPT. Appendix C.2 reports the accuracy metrics of the measuring equipment and data acquisition system.

Table 3.7 reports the minimum, the maximum and the mean relative error of the variables reported in Figure 3.21. The LPC rotational speed presents a relative error between 2.8 and 6.3 %. A mean relative deviation of around 10 % is found in the prediction of the pressure at the outlet of the second compressor. The dynamic model predicts

Table 3.7: Minimum, maximum, and mean relative error for the variables shown in Figure 3.21.

Variable	Minimum [%]	Maximum [%]	MRE [%]
PT outlet temperature	2.8	3.9	3.4
HPC outlet pressure	4.8	12.9	9.2
LPT outlet pressure	18.7	31.8	25.8
HP shaft speed	0.7	2.3	1.6
LP shaft speed	2.8	6.3	4.7
Fuel mass flow rate	0.1	12.6	5.5

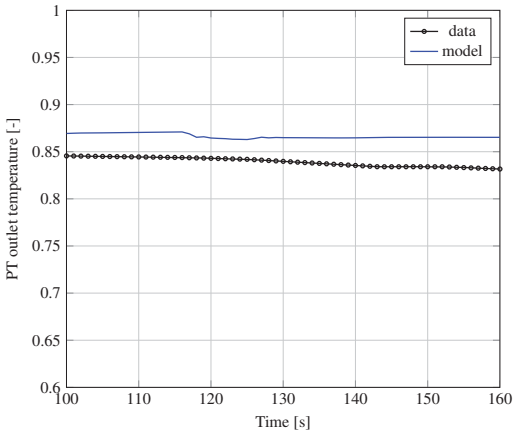

(a) Power turbine outlet temperature

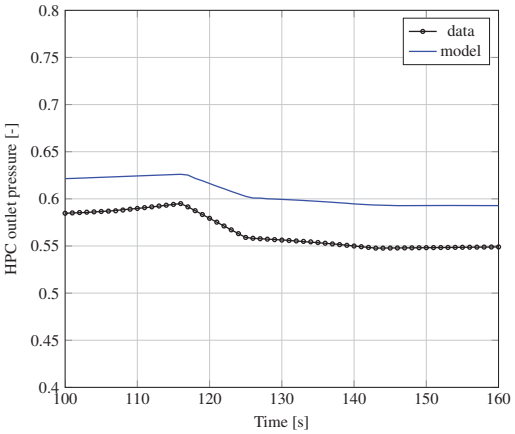

(b) High pressure compressor outlet pressure

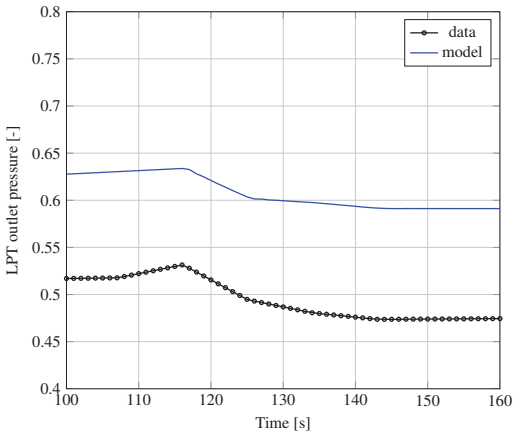

(c) Low pressure turbine outlet pressure

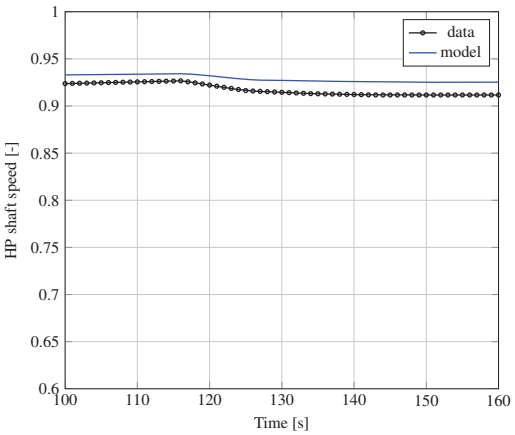

(d) High pressure shaft speed

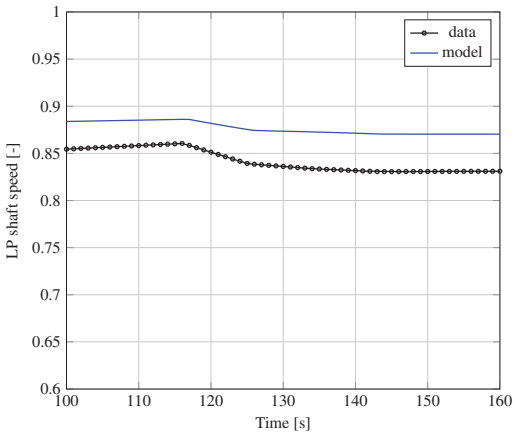

(e) Low pressure shaft speed

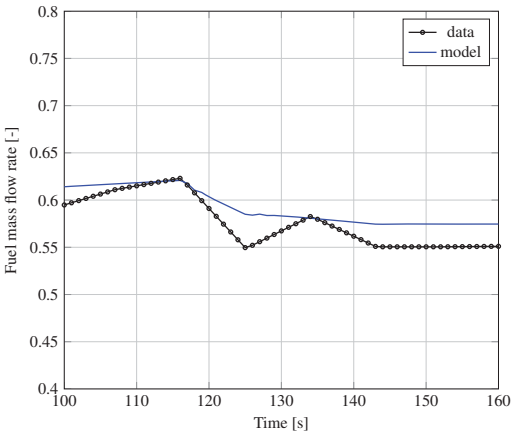

(f) Fuel mass flow rate

Figure 3.21: Comparison between the dynamic model outlined in Section 3.2.1 and the operational data provided by the platform operator. The variables in the ordinate are reported relative to the value at design-point.

the rotational speed of this component with a maximum error lower than 2.3 %. The largest MRE (25.8 %) occurs in the evaluation of the pressure at the outlet of the LPT. The relative error related to the fuel flow ranges from 0.1 to 12.6 %. The temperature at the outlet of the power turbine exhibits a MRE of 3.4 %. The highest mean relative errors is found estimating the pressure at the outlet of the HPC and LPT. The time-dependent trend of the pressures is in agreement with the operational data, despite the relatively high errors (9.2 % and 25.8 %). The high deviation has two reasons: i) inaccurate estimation of the thermodynamic states at the outlet of each component (possibly caused by aging of the engine), and ii) the low absolute value of the quantity being measured. Figures 3.21(d) and 3.21(e) show that the shaft speeds have the closest agreement with the measurements.

Figure 3.21(f) shows an unexpected increment of the fuel mass flow rate at around 130 s for the measured data at decreasing engine loads. The platform operator provided the fuel consumption as the volumetric flow rate. Yearly average values for the fuel composition, temperature and pressure were accessible. Consequently, a mean fuel density, evaluated with the Modelica ideal gas package, was used to convert the variable in $\mathrm{kg \cdot s^{-1}}$. The fuel mass flow rate reported in Figure 3.21(f) is thus insensible to variations in fuel temperature, pressure and composition. The density and the fuel mass flow rate could decrease with a change in the thermodynamic state of the combustible. Uncertainties of the system processing the data may also explain the unexpected increment of the fuel mass flow rate. Despite the presence of steady-state offsets, the results of the dynamic model are in agreement with the available measurements. The developed model is thus capable of capturing the transient and part-load characteristic of the power generation system on Draugen. It is underlined that the dynamic model in Modelica language was verified with the transfer-function-based model outlined in Section 3.4.1. Briefly summarized, the physical model can predict the fluctuations of the grid frequency with a deviation lower than 1.0 %, compared to the model developed by the gas turbine manufacturer.

3.5.2 The organic Rankine cycle module

The model of the ORC system is composed of software objects acquired from a library that was developed to model a 150 kW ORC system using toluene as the working fluid. This was successfully validated for transient operation against experimental data, as discussed in Casella et al. [11]. The model of the bottoming cycle unit is, therefore, deemed reliable, considering the similarity of the application at hand with the one presented in the cited reference. Furthermore, the model implementation in Modelica language was verified using the Simulink model described in Section 3.4.1. The comparison gave a relative error lower than 2 % for all the process variables of the ORC

module.

3.5.3 The steady-state models

The results of the thermodynamic state calculation for the Rankine and Brayton processes were compared with the values provided by the in-house open-source simulation tool Dynamic Network Analysis [38]. No appreciable difference in the process variables was observable between the results given by the two programs. Additionally, it was verified that the on- and off-design operating points predicted by the steady-state models were consistent with those of the dynamic tools described in Sections 3.2 and 3.4.

As for the heat transfer equipment, the design methods of the shell-and-tube heat exchanger, FPHE and once-through boiler were verified with the examples outlined in Coulson et al. [13], Yousefi et al. [51] and Dumont and Heyen [16], respectively. The differences between the model results and the data reported in the references are within 4.0 % for the overall heat transfer coefficient and pressure drops. The cause of the deviation was found to be the difference in the method used for the calculation of the thermodynamic and transport properties of the working fluids.

The accuracy of the economic analysis relates to the equations used to compute the purchased-equipment cost of the plant components. Preliminary investigations showed that the numerical results are within the values reported in Boyce [7] for the SRC unit, in Bolland et al. [6] for the ABC system, and in Quoilin et al. [40] for the ORC power module. On the other hand, the uncertainties of the economic calculations were estimated to be around 20 % for all financial indicators. The degree of uncertainty is high. The results of the economic study are thus used to carry out a qualitative comparison of the waste heat recovery technologies. No quantitative conclusion can be drawn without precise cost correlations from manufacturers.

Bibliography

[1] M. Astolfi, M. C. Romano, P. Bombarda, and E. Macchi. Binary ORC (Organic Rankine Cycles) power plants for the exploitation of medium–low temperature geothermal sources–Part B: Techno-economic optimization. *Energy*, 66(0):435–446, 2014.

[2] A. Bejan, G. Tsatsaronis, and M. J. Moran. *Thermal design and optimization*. John Wiley & Sons, Inc., Hoboken, New Jersey, 1996. ISBN: 9780471584674.

[3] I. H. Bell, J. Wronski, S. Quoilin, and V. Lemort. Pure and pseudo-pure fluid thermophysical property evaluation and the open-source thermophysical property library CoolProp. *Industrial & Engineering Chemistry Research*, 53(6):2498–2508, 2014.

[4] K. J. Bell. *Delaware method for shell-side design*. Taylor & Francis, New York, New York City, New York, 1988. ISBN: 9780891167297.

[5] A. Bemporad, M. Morari, and N. L. Ricker. *Model Predictive Control Toolbox For Use with MATLAB*. The MathWorks, Inc., Natick, Massachusetts, March 2014.

[6] O. Bolland, M. Førde, and B. Hånde. Air bottoming cycle: use of gas turbine waste heat for power generation. *Journal of Engineering for Gas Turbines and Power*, 118:359–368, 1996.

[7] M. P. Boyce. *Gas turbine engineering handbook*. Butterworth-Heinemann, Oxford, Great Britain, 2012. ISBN: 9780123838421.

[8] E. F. Camacho and C. B. Alba. *Model predictive control*. Springer, London, Great Britain, 2013. ISBN: 9781852336943.

[9] S. Camporeale, B. Fortunato, and M. Mastrovito. A modular code for real time dynamic simulation of gas turbines in Simulink. *Journal of Engineering for Gas Turbines and Power*, 128(3):506–517, 2006.

[10] F. Casella and A. Leva. Modelling of thermo-hydraulic power generation processes using Modelica. *Mathematical and Computer Modeling of Dynamical Systems*, 12(1):19–33, Feb. 2006.

[11] F. Casella, T. Mathijssen, P. Colonna, and J. van Buijtenen. Dynamic modeling of ORC power systems. *Journal of Engineering for Gas Turbines and Power*, 135: 1–12, 2012.

[12] K. C. Cotton. *Evaluating and improving steam turbine performance*. Cotton Fact, Rexford, New York, 1998. ISBN: 9780963995513.

[13] J. Coulson, J. Richardson, and J. Backhurst. *Coulson and Richardson's Chemical Engineering*. Chemical engineering. Butterworth-Heinemann, Oxford, Great Britain, 1999. ISBN: 9780750644440.

[14] K. Deb. *Multi-objective optimization using evolutionary algorithms*. John Wiley & Sons, Inc., West Sussex, Great Britain, 2001.

[15] M. Doyle and S. Dixon. The stacking of compressor stage characteristics to give an overall compressor performance map. *Aeronautical Quarterly*, 13:349–367, 1962.

[16] M.-N. Dumont and G. Heyen. Mathematical modelling and design of an advanced once-through heat recovery steam generator. *Computers & Chemical Engineering*, 28(5):651 – 660, 2004.

[17] L. Friedel. Pressure drop during gas/vapor-liquid flow in pipes. *International Chemical Engineering*, 20(3):352–367, 1980.

[18] P. Fritzson. *Principles of Object-Oriented Modeling and Simulation with Modelica 2.1*. John Wiley & Sons, Inc., Piscataway, New York, 2003. ISBN: 9780470937617.

[19] O. Genceli. *Heat exchangers*. Birsen Book Company, Turkey, 1999. ISBN: 9789755112183.

[20] D. M. Ginosar, L. M. Petkovic, and D. P. Guillen. Thermal stability of cyclopentane as an organic Rankine cycle working fluid. *Energy & Fuels*, 25(9):4138–4144, 2011.

[21] V. Gnielinski. On heat transfer in tubes. *International Journal of Heat and Mass Transfer*, 63(0):134 – 140, 2013.

[22] S. S. Godbole. Comparing dynamic responses of recirculating and once-through steam generators for next generation LWRs. *Trans. Am. Nucl. Soc*, 62:1–4, 1990.

[23] S. Haaf. *Wärmeübertragung in Luftkühlern*. Springer Verlag, Berlin, Germany, 1988. ISBN: 9783540154778.

[24] F. Haglind and B. Elmegaard. Methodologies for predicting the part-load performance of aero-derivative gas turbines. *Energy*, 34(10):1484 – 1492, 2009.

[25] S. Hall, S. Ahmad, and R. Smith. Capital cost targets for heat exchanger networks comprising mixed materials of construction, pressure ratings and exchanger types. *Computers & chemical engineering*, 14(3):319–335, 1990.

[26] F. P. Incropera, D. P. DeWitt, T. L. Bergman, and A. S. Lavine. *Fundamentals of Heat and Mass Transfer*. John Wiley & Sons, Inc., Jefferson City, Missouri, 6 edition, 2007. ISBN: 9780470501979.

[27] Inflationdata. Historical Annual U.S. Inflation Rate from 1913 to the present. Website, July 2014. [accessed: 10/07/2014].

[28] D. Q. Kern. *Process heat transfer*. McGraw-Hill, New York City, New York, 1950. ISBN: 9780070341906.

[29] J. Kurzke. Component Map Collection. Website, 2004. [accessed: 01/07/2014].

[30] J. Kurzke. How to create a performance model of a gas turbine from a limited amount of information. In *Proceedings of ASME Turbo Expo 2005*, pages 145–153, Reno-Tahoe, Nevada, June 2005.

[31] Z. Lian, K. Chua, and S. Chou. A thermoeconomic analysis of biomass energy for trigeneration. *Applied Energy*, 87(1):84–95, 2010.

[32] M.-A. Lozano, A. Valero, and L. Serra. Theory of exergetic cost and thermoeconomic optimization. In *Proceedings of the International Symposium ENSEC*, pages 339 – 350, Cracow, Poland, July 1993.

[33] R. M. Manglik and A. E. Bergles. Heat transfer and pressure drop correlations for the rectangular offset strip fin compact heat exchanger. *Experimental Thermal and Fluid Science*, 10(2):171–180, 1995.

[34] T. MathWorks. *Getting Started with MATLAB*. The MathWorks, Inc., Natick, Massachusetts, March 2014.

[35] T. MathWorks. *Getting Started with SIMULINK*. The MathWorks, Inc., Natick, Massachusetts, March 2014.

[36] Ministry of the Environment. The Government is following up on the Climate Agreement. Press release, October 2012. [accessed: 01/07/2014].

[37] J. A. Nelder and R. Mead. A simplex method for function minimization. *The Computer Journal*, 7(4):308–313, 1965.

[38] C. Perstrup. Analysis of power plant installation based on network theory. Master's thesis, Technical University of Denmark, Laboratory of Energetics, 1991.

[39] S. Quoilin, R. Aumann, A. Grill, A. Schuster, V. Lemort, and H. Spliethoff. Dynamic modeling and optimal control strategy of waste heat recovery organic Rankine cycles. *Applied Energy*, 88(6):2183–2190, 2011.

[40] S. Quoilin, M. V. D. Broek, S. Declaye, P. Dewallef, and V. Lemort. Techno-economic survey of organic Rankine cycle (ORC) systems. *Renewable and Sustainable Energy Reviews*, 22:168–186, 2013.

[41] P. Rabinowitz. *Numerical Methods for Nonlinear Algebraic Equations*. Gordon and Breach Science Publishers, 1970. ISBN: 9780677142357.

[42] S. Z. Rouhani and E. Axelsson. Calculation of void volume fraction in the subcooled and quality boiling regions. *International Journal of Heat and Mass Transfer*, 13(2):383–393, 1970.

[43] M. Schobeiri. *Turbomachinery flow physics and dynamic performance*. Springer Berlin, Berlin, Germany, 2005. ISBN: 9783540223689.

[44] M. Shah. Chart correlation for saturated boiling heat transfer: equations and further study. *ASHRAE Transaction*, 88(1):185–196, 1982.

[45] R. K. Shah and D. P. Sekulić. *Fundamentals of Heat Exchanger Design*. John Wiley & Sons, Inc., Hoboken, New Jersey, 2003.

[46] A. Stodola. *Dampf- und Gasturbinen: Mit einem Anhang über die Aussichten der Wärmekraftmaschinen*. Springer Berlin, Berlin, Germany, 1922. ISBN: 7352997563.

[47] W. Traupel. *Thermische Turbomaschinen. Band 1, 3. Auflage, 1977*. Springer-Verlag, Berlin, Germany, 1977. ISBN: 9783540079392.

[48] A. Valero, M. A. Lozano, L. Serra, G. Tsatsaronis, J. Pisa, C. Frangopoulos, and M. R. von Spakovsky. CGAM problem: definition and conventional solution. *Energy*, 19(3):279–286, 1994.

[49] Verein Deutscher Ingenieure. *VDI-Wärmeatlas: Berechnungsblätter für den Wärmeübergang*. Springer-Verlag, Berlin, Germany, 1953. ISBN: 9783540412014.

[50] J. P. Veres. Centrifugal and Axial Pump Design and Off-Design Performance Prediction. Technical report, NASA, Sunnyvale, United States of America, 1994. Technical Memorandum 106745.

[51] M. Yousefi, R. Enayatifar, and A. Darus. Optimal design of plate-fin heat exchangers by a hybrid evolutionary algorithm. *International Communications in Heat and Mass Transfer*, 39(2):258 – 263, 2012.

[52] J. Zhang, Y. Zhou, R. Wang, J. Xu, and F. Fang. Modeling and constrained multivariable predictive control for ORC (organic Rankine cycle) based waste heat energy conversion systems. *Energy*, 66:128–138, 2014.

[53] N. Zhang and R. Cai. Analytical solutions and typical characteristics of part-load performances of single shaft gas turbine and its cogeneration. *Energy Conversion and Management*, 43(9):1323–1337, 2002.

Chapter 4

Results

This chapter contains the results of this thesis. It consists of three main segments. The first part deals with the steady-state multi-objective optimization of the bottoming cycle units. The results of the dynamic simulations are then used to complement the design-point analysis by applying time-dependent metrics to discard infeasible designs. The performance of the model predictive control unit and steady-state optimizer is then assessed for the gas turbine-based power system with and without the ORC turbogenerator.

4.1 Steady-state multi-objective optimization

This section discloses the results of the steady-state multi-objective optimization applied to the three bottoming cycle technologies analyzed in this work. Additionally, the results of the optimization procedure are presented for the five fluid candidates listed in Table 2.3.

4.1.1 Waste heat recovery technologies

Table 4.1 lists the results of the multi-objective optimization procedure for the set of variables and objective functions given in Equations 3.8 - 3.11. The working fluid circulating in the ORC turbogenerator is cyclopentane. For each waste heat recovery technology, the table reports the calculation of the arithmetic mean average (AMA), the relative standard deviation (RSD) in percent, and the minimum and maximum values of the optimized variables. A low RSD implies that the variable does not vary significantly along the Pareto frontier of the waste heat recovery unit. Considering all three bottoming cycle units, the quantities showing the lowest RSDs are: the pinch point and the baffle length of the condensers, the temperature of the exhaust gases, and the temperature differences of the primary heat exchangers.

Figure 4.1 shows a two-dimensional prospect of the Pareto fronts. The average daily CO_2 emissions of the power systems are a function of the weight of the bottoming cycle unit. The three curves present a hyperbolic trend.

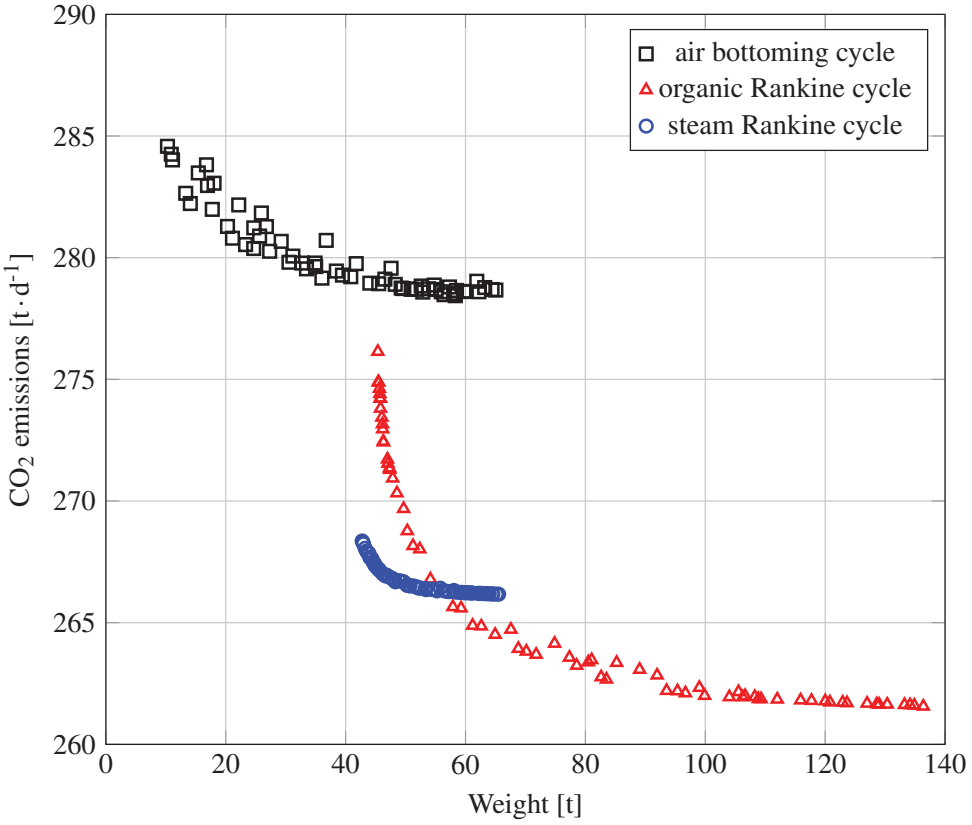

Figure 4.1: Pareto fronts of the three waste heat recovery technologies. The CO_2 emissions (first objective function) are related to the weight of the bottoming cycle units (second objective function). The working fluid serving the ORC unit is cyclopentane.

Table 4.1: Results of the multi-objective optimization. Maximum, minimum, arithmetic mean average, and relative standard deviation of the optimized variables.

Variable	Maximum	Minimum	AMA	RSD [%]
Steam Rankine cycle				
p_5 [bar]	14.3	14.1	14.2	0.35
ΔT_{OTB} [K]	24.9	22.7	23.3	2.60
T_{11} [K]	449.3	449.2	449.2	0.01
ΔT_{c} [K]	30.1	28.4	29.8	1.57
$d_{\mathrm{i,OTB}}$ [mm]	27.1	17.0	22.3	14.50
$d_{\mathrm{i,OTB,sup}}$ [mm]	45.7	34.5	40.0	8.57
l_{OTB} [m]	3.2	2.8	2.9	4.12
Nt_{OTB} [-]	74	63	67	6.39
$d_{\mathrm{i,c}}$ [mm]	49.9	42.2	45.3	6.20
l_{c} [m]	4.9	4.8	4.9	0.61
$l_{\mathrm{b,c}}$ [%]	117.7	117.6	117.7	0.03
Organic Rankine cycle				
p_6 [bar]	34.8	20.8	30.1	19.61
ΔT_{OTB} [K]	37.7	31.0	35.5	6.03
ΔT_{ir} [K]	32.2	28.8	30.5	3.81
T_{11} [K]	438.7	419.3	429.5	1.93
ΔT_{c} [K]	41.1	38.7	39.9	1.98
$d_{\mathrm{i,OTB}}$ [mm]	39.0	26.3	32.9	13.72
$d_{\mathrm{i,OTB,sup}}$ [mm]	44.1	34.2	40.8	4.54
l_{OTB} [m]	3.9	1.9	2.7	26.24
Nt_{OTB} [-]	76	53	63	14.52
$d_{\mathrm{i,r}}$ [m]	33.4	20.7	26.2	18.42
l_{r} [m]	7.1	4.1	5.1	16.33
$l_{\mathrm{b,r}}$ [%]	83.0	74.4	79.7	3.41
$d_{\mathrm{i,c}}$ [m]	43.5	31.1	35.6	11.54
l_{c} [m]	5.3	4.1	4.7	7.93
$l_{\mathrm{b,c}}$ [%]	92.9	82.5	87.7	4.36
Air bottoming cycle				
$r_{\mathrm{c,1}}$ [-]	2.2	1.5	1.8	8.44
$r_{\mathrm{c,2}}$ [-]	2.1	1.3	1.8	9.14
T_5 [K]	599.8	560.1	592.5	1.84
T_{11} [K]	442.8	412.5	424.6	2.42
$F_{\mathrm{h,a}}$ [mm]	25.6	13.6	19.4	15.04
nf_{a} [m^{-1}]	272	206	230	6.75
$F_{\mathrm{l,a}}$ [mm]	139.2	36.8	92.8	30.14
$F_{\mathrm{h,exh}}$ [mm]	37.4	22.9	30.5	12.71
nf_{exh} [m^{-1}]	329	266	296	5.09
$F_{\mathrm{l,exh}}$ [mm]	133.6	38.5	92.4	23.01
Np_{exh} [-]	146	118	138	4.59
l_{exh} [m]	2.98	1.67	2.23	16.67

The power system employing the ABC unit presents the lowest yearly plant performance (highest CO_2 emissions). This technology enables to achieve the lowest possible weight, i.e., 9 t. The SRC unit exhibits the narrowest Pareto front, spanning from 266 to 268 $t \cdot d^{-1}$ (40 to 65 t). On the contrary, the optimal designs of the ORC technology cover the largest range of daily CO_2 emissions and weights. Figure 4.2 shows the net present value as a function of the weight. The points associated to the ABC designs are not uniformly distributed. However, the curves of all three bottoming cycles initially increase and, subsequently, flatten out. Note that the net present value is a function of the total investment cost and the yearly incomes, ultimately dependent on the combined cycle performance. As regarding the ABC module, the net present value becomes negative at low and high weights. The peak is 0.3 M$ lower compared to that of the ORC module. The highest economic revenue (2.7 M$) occurs for a total power (gas turbine A and ABC unit) of 18.6 MW, with a design- and part-load efficiency of 35.1 % and 32.0 %. The waste heat recovery technology delivering the highest net present value (3.7 M$) is the steam Rankine cycle. The combined cycle power is 21.2 MW. The thermal efficiencies at design- and part-load are 40.1 % and 35.6 %. As for the ORC technology, the largest value of the third objective function (3.0 M$)

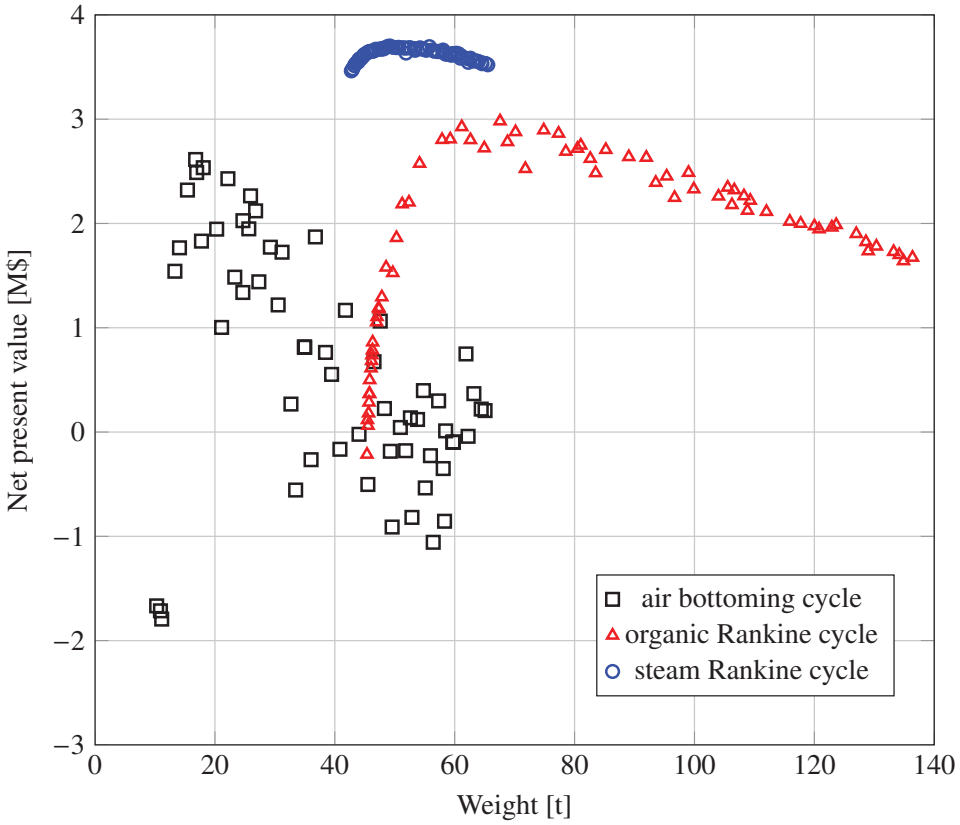

Figure 4.2: Pareto fronts of the three waste heat recovery technologies. The net present value (third objective function) is related to the weight of the bottoming cycle (second objective function). The working fluid serving the ORC unit is cyclopentane.

occurs for a net power output of 21.4 MW. The design- and part-load efficiencies are 40.4 % and 36.0 %. Figures 4.3 and 4.4 show the weight and the purchased-equipment cost breakdowns of the three bottoming cycle units. The set of variables giving the highest net present value is used. The lightest power unit is the air bottoming cycle system followed by the steam and organic Rankine engines.

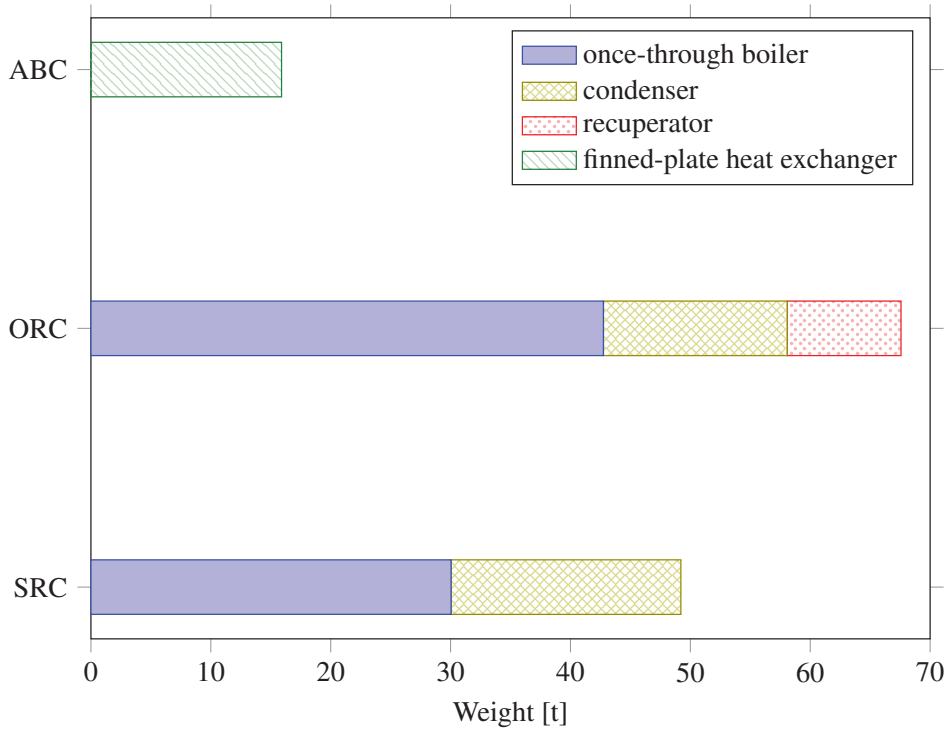

Figure 4.3: Breakdown of the weight for the three waste heat recovery technologies. The weight of the heat exchangers constituting the bottoming cycle units is reported.

The once-through boiler has the most significant impact on the total weight of the Rankine units. Stainless steel finned tubes are used to cope with the high heat transfer resistance of the exhaust gas stream. The water-cooled condensers and the ORC recuperator contribute with around 20 t each to the total weight. Neglecting the contribution of the intercooler, the heat transfer equipment serving the ABC unit consists only of the finned-plate heat exchanger. Its total weight is approximately 16 t.

Figure 4.4 demonstrates that the initial cost of the SRC and ORC unit is more than double the value of the air Brayton engine. The three turbines contribute with the largest share to the purchased-equipment cost of the ABC system. The air compressors and the heat transfer equipment require similar initial expenses. The once-through boiler and the turbine are the most expensive components in the Rankine engines. The primary heat exchanger has a larger impact (the relative share is $\approx 50\,\%$) on the cost of the ORC turbogenerator compared to the SRC unit.

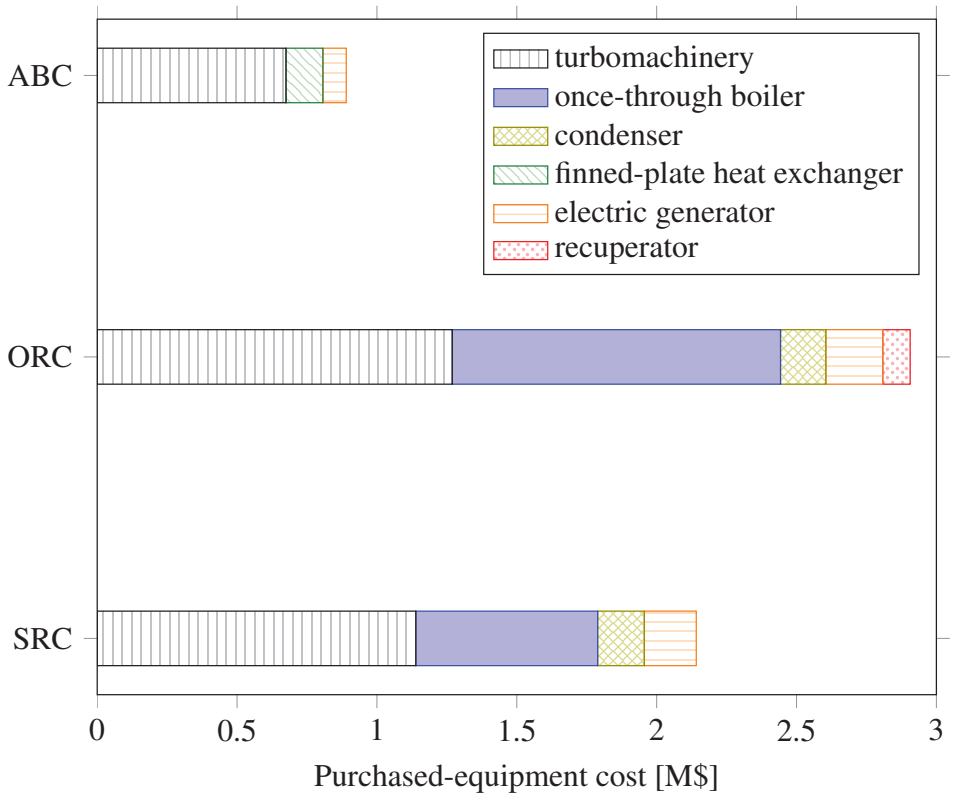

Figure 4.4: Breakdown of the purchased-equipment cost for the three waste heat recovery technologies. The purchased-equipment cost of the components constituting the bottoming cycle units is indicated. The bar for the turbomachinery includes the prices of turbines, compressors and pumps.

4.1.2 Working fluid selection

The results related to the ORC unit have been devised with cyclopentane as working fluid. Figure 4.5 shows, instead, the CO_2 emissions-weight Pareto fronts of the fluid candidates listed in Table 2.3. The two objective functions are in the range of 40 - 200 t and 255 - 280 $t \cdot d^{-1}$ for all organic compounds. The curves of cyclopentane and benzene lay in the region characterized by the lowest weight and emissions. Isohexane and isopentane cover approximately the same areas in the plot. On the contrary, the trend of cyclohexane starts from a CO_2 emission and weight of 270 $t \cdot d^{-1}$ and 92 t, to terminate at around 265 $t \cdot d^{-1}$ and 160 t. Cyclopentane allows to design the lightest power module for a CO_2 production of 270 $t \cdot d^{-1}$. In this regard, benzene performs better at lower emissions (higher performances). Considering a weight of 120 t, benzene is the compound attaining the greatest CO_2 savings. Cyclopentane, cyclohexane, isohexane and isopentane complete the ranking. For lighter units ($\leq$ 60 t), the working fluid ensuring the highest energy conversion efficiency is cyclopentane.

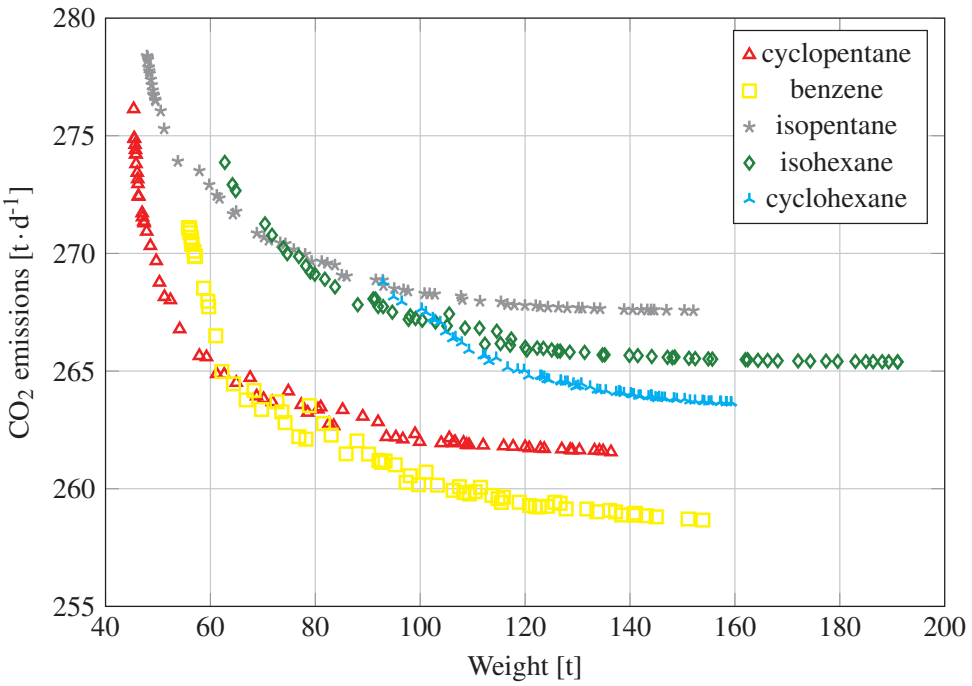

Figure 4.5: Pareto fronts of the organic Rankine cycle unit for the fluid candidates listed in Table 2.3. The CO_2 emissions (first objective function) are related to the weight of the organic Rankine cycle unit (second objective function).

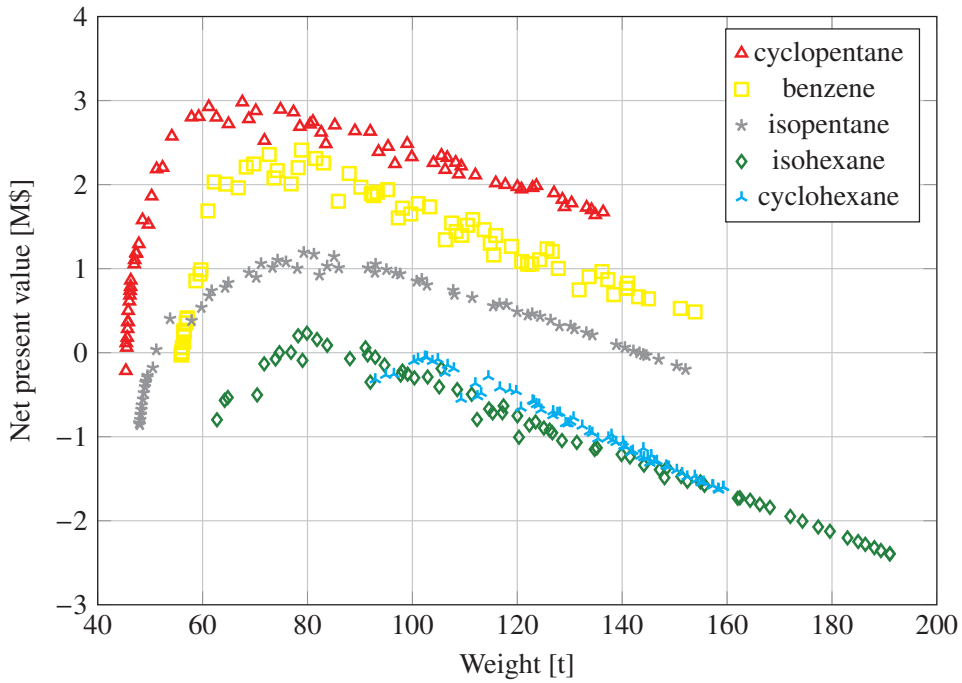

Figure 4.6: Pareto fronts of the organic Rankine cycle unit for the fluid candidates listed in Table 2.3. The net present value (third objective function) is related to the weight of the organic Rankine cycle unit (second objective function).

Figure 4.6 shows the trends relating the net present value to the weight of the heat exchangers for each fluid candidate. The graph confirms the presence of a weight which maximizes the economic revenue. Each curve starts with a relatively steep positive gradient. It reaches the maximum NPV, and it drops linearly to lower economic revenues. Cyclopentane gives the largest income (3.0 M$). A slightly lower revenue (2.4 M$) is expectable with benzene. It is also observed that isohexane and cyclohexane deliver economically infeasible designs. Their net present value is negative for a large number of Pareto solutions. The peak of isopentane (1.0 M$) is around half the value of benzene. Its economic indicator becomes negative at the extremes of the Pareto frontier.

Figure 4.7 shows the purchased-equipment cost breakdown of the organic Rankine cycle units for three hydrocarbons with the set of variables giving the maximum net present value. Cyclopentane presents the lowest total investment cost followed by isohexane and benzene. The condenser, the recuperator and the electric generator con-

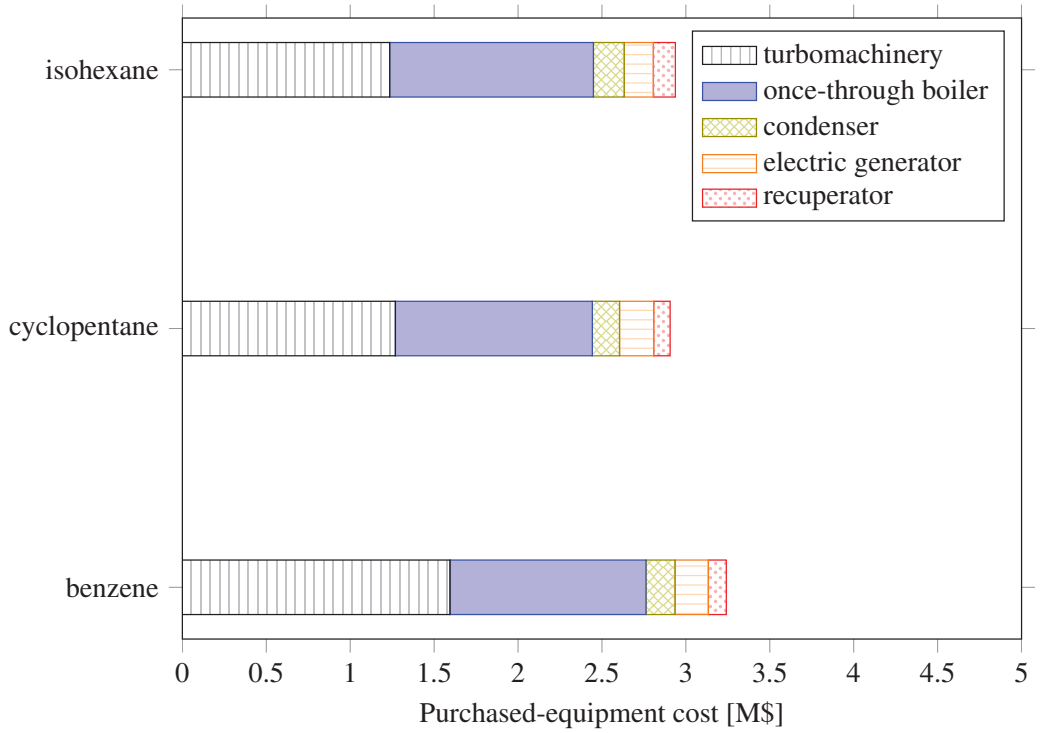

Figure 4.7: Breakdown of the purchased-equipment cost of the organic Rankine cycle unit for three of the fluid candidates listed in Table 2.3.

tribute with similar shares to the overall purchased-equipment cost. The turbine expense has the largest impact on the engine cost, especially with benzene. The modules using cyclopentane and isohexane have similar total investment costs. However, the potential reduction of CO_2 emissions with cyclopentane is on an average 3 % higher compared to isohexane, see Figure 4.5. The weight breakdowns of cyclohexane and isopentane led to figures similar to those of cyclopentane.

4.2 Dynamics as design criterion

The dynamics of gas turbine A and the ORC unit is examined. Figure 4.8 shows the transient response of the plant for two points of the Pareto front, i.e., those corresponding to the design candidates with the highest and the lowest weight. Gas turbine C is on standby. The dynamic test entails the trip of engine B. The event causes the power set-point of gas turbine A and the ORC module to step by $5.0\,\mathrm{MW}\cdot\mathrm{s}^{-1}$. The working fluid circulating in the ORC unit is cyclopentane. The influence of the ORC turbogenerator design on the transient of the network frequency is clearly visible; the lighter the heat exchangers the larger the undershooting of the frequency.

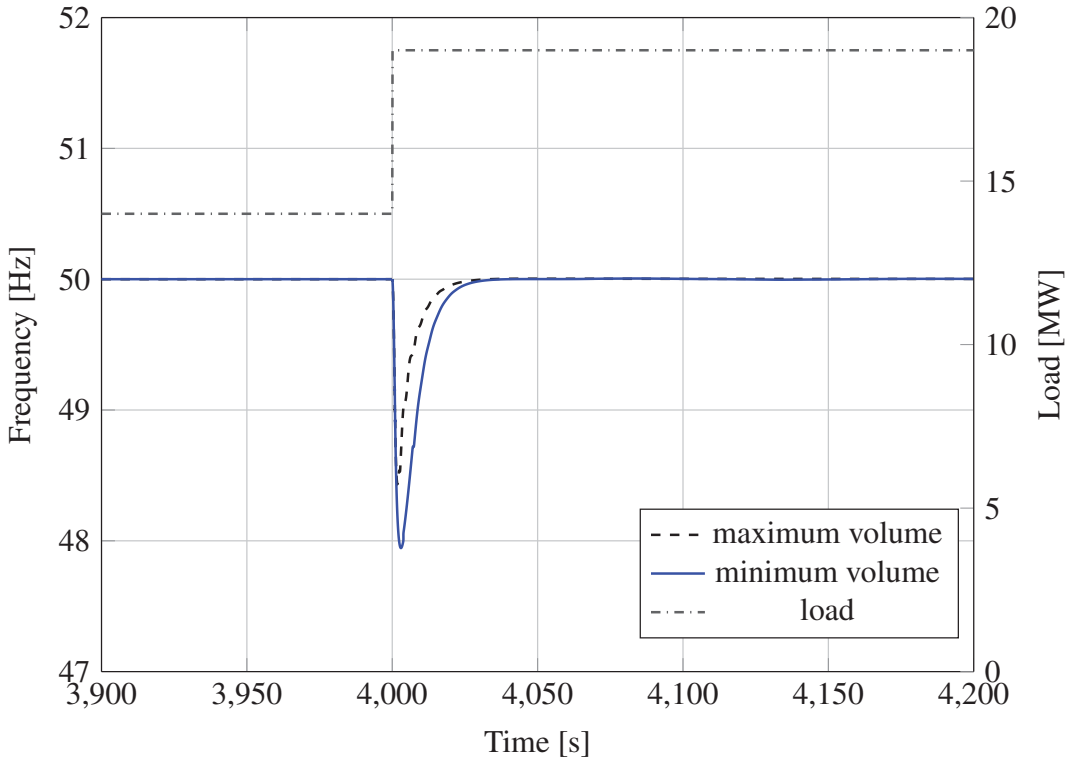

Figure 4.8: Frequency of the grid versus time for the two designs characterized by the maximum and minimum weight of the heat transfer equipment. The load set-point for the system comprising one gas turbine and the ORC unit is also reported.

Figure 4.9(a) relates the weight to the minimum frequency reached during the transient for each point of the Pareto front. The curve presents a highly non-linear trend. The magnitude of the frequency variations increases more sharply for decreasing weight. The frequency undershooting must not exceed 4 % of the nominal value, according with the standards for power quality adopted by the platform owner. Thus, considering a safety margin of 0.2 %−points, ORC power modules characterized by a weight lower than 46.2 t violate this constraint. These designs are, therefore, identified as infeasi-

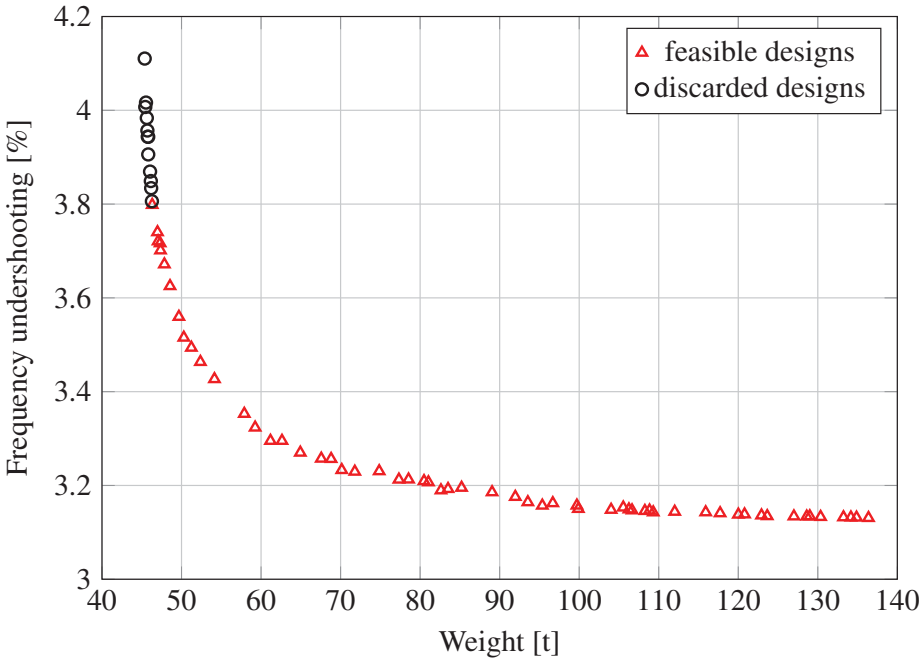

(a)

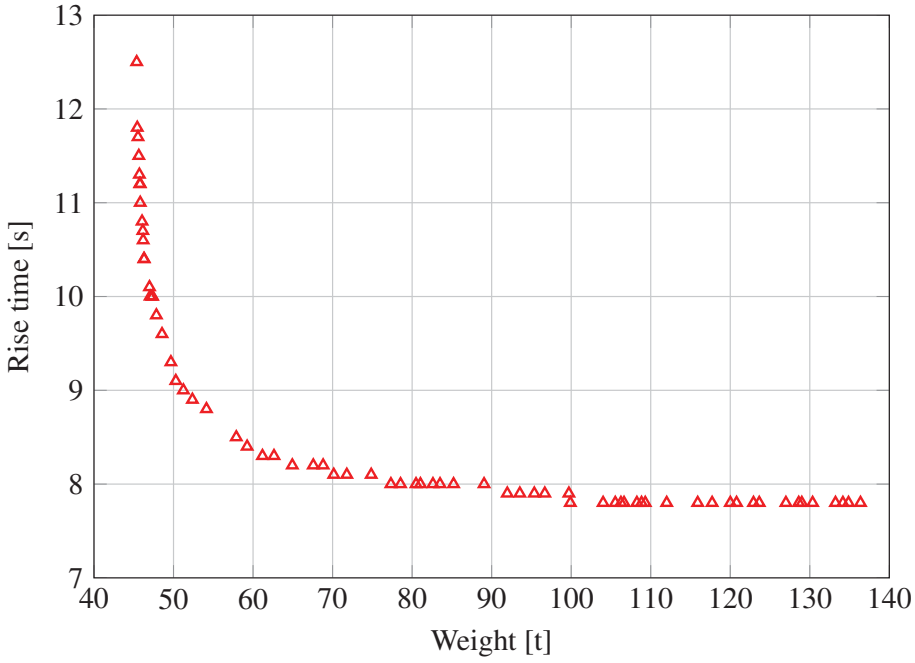

(b)

Figure 4.9: Results of the dynamic test. All the points of the Pareto front are reported. 4.9(a) Frequency undershooting versus weight of the heat transfer equipment. The designs identified by the ○ symbol are discarded due to the unacceptable frequency undershooting $> 3.8\,\%$. 4.9(b) Rise time versus weight of the heat transfer equipment.

ble. They are marked with the hollow circle (○) symbol in Figure 4.9(a). Figure 4.9(b) shows the rise time as a function of weight. The rise time is defined as the time required for the frequency to return back to 99.0 % of the value at steady-state. The trend of the curve is also non-linear with a minimum of approximately 7.8 s at 136.3 t. Design candidates characterized by light heat exchangers present a longer rise time. This dynamic metric reaches its peak value at the minimum weight of the Pareto frontier.

Figure 4.10(a) shows the time evolution of the temperature at the inlet of the ORC turbine for three points of the Pareto front. The two designs characterized by the maximum and minimum weight of the heat transfer equipment, together with an intermediate value, are considered. The load of the combined cycle unit undergoes a sharp variation. The temperature and the mass flow rate of the exhaust gases entering the OTB rise and reach steady-state in less than 20 s. As anticipated in Section 3.2.3, the dynamics of the temperature T_6 is much slower than the temperature of the exhaust gases T_{10}. The two major contributions to the delay are the inertia of the metal walls and of the working fluid in liquid phase contained in the heat exchangers. The mass of the exhaust gases is negligible. Conversely, that of the liquid cyclopentane contained in the OTB and in the recuperator is approximately 15 times larger than its mass in the vapor phase. The temperatures of the ORC designs with a weight between 50 t and 135 t present similar trends. The curves are characterized by an overshooting extinguished by the PI controller in approximately 15 min. The curve of the lightest unit shows an unstable tendency during the load modulation with four relative peaks.

Figure 4.10(b) reports the maximum value of the turbine inlet temperature T_6 as a function of the weight. This variable is of paramount importance, being closely related to the maximum temperature reached by the ORC working fluid. The peak value is encountered in the fluid layer close to the metal wall in the once-through boiler. Light units entail lower temperature peaks (down to 290 °C). The values rapidly increase with the weight, reaching a maximum of 310 °C at around 60 t. The peak temperature subsequently drops, stabilizing at a value lower than 300 °C for the heaviest ORC modules. As reported in Section 3.4.3, cyclopentane presents an upper temperature limit for safe operations of the ORC system. Design candidates exhibiting a temperature peak larger than 300 °C (identified by the ○ symbol in Figure 4.10(b)) could incur in fluid decomposition during sharp load modulations. Note that the temperature limit is larger than the one selected for the initialization of the MPC unit, see Table 3.6. In that case, the overheating of the working fluid is more severe as it occurs in steady-state conditions. On the contrary, the temperature peak refers here to a dynamic event extinguishing in few minutes.

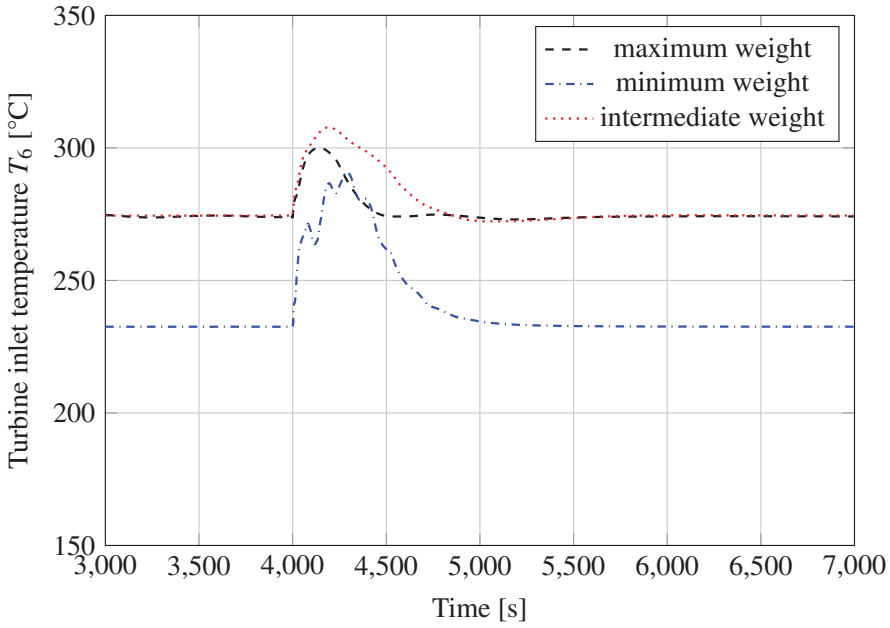

(a)

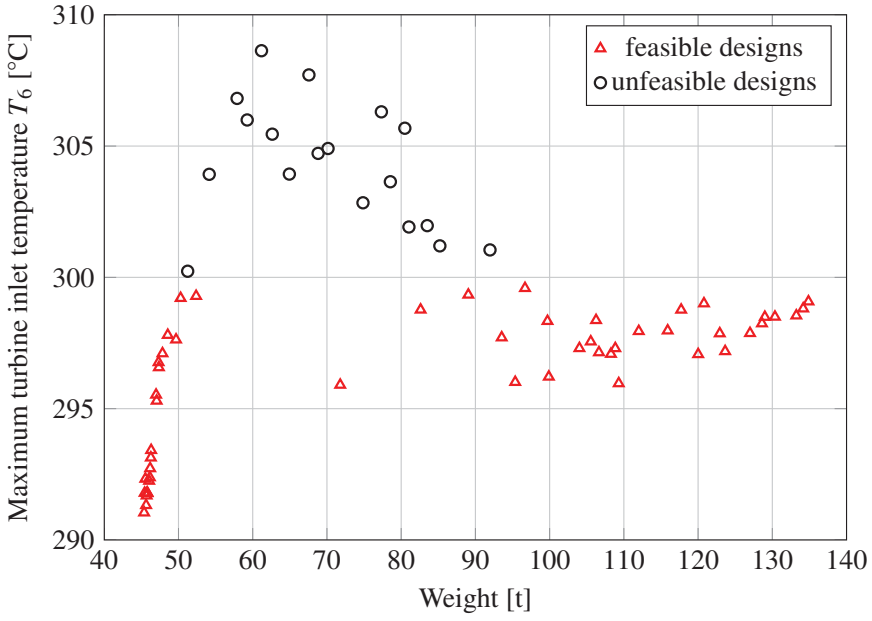

(b)

Figure 4.10: Results of the dynamic test. 4.10(a) Turbine inlet temperature T_6 versus time for three selected designs (the two designs characterized by the maximum and minimum weight of the heat transfer equipment, together with an intermediate value). 4.10(b) Maximum turbine inlet temperature T_6 versus weight of the heat transfer equipment. All the points of the Pareto front are reported. The designs identified by the ○ symbol present a higher risk of fluid decomposition.

4.3 The control system

This section presents the results of the regulator consisting of the model predictive control and the steady-state performance optimizer. The regulator is applied first to the gas turbine-based power plant (see Figure 2.2), and then to the system integrating the ORC module (see Figure 2.5).

4.3.1 The gas turbine-based power plant

The model predictive control is first applied to the gas turbine-based system considering the operation of a single engine. Equations 3.20 and 3.21 give the models used to design the MPC unit. The control action maneuvering the fuel valve solves Equation 3.18, subject to the system of Equations 3.19 and to the boundary conditions stated in Table 3.6. The dynamic simulations are performed on a discrete domain with a sampling time of 100 ms.

Figures 4.11(a) and 4.11(b) show the frequency responses over time for the model predictive control and the feedback regulator. In the two plots, the steps in the load set-point are 4 MW and 1 MW, respectively. For the first power change, the original control system reaches a maximum frequency undershooting of 3.0 %, while the MPC gives 1.7 %. The frequency given by the feedback controller presents an oscillating trend with a global minimum of 49.6 Hz for a 1 MW step. The model predictive control decreases the drop of the grid frequency to 0.3 Hz, with no significant periodic fluctuations. Both case studies indicate that the novel control system is superior compared to the feedback controller, considering the quality of the power supply. These advantages are particularly evident for the largest change of the load set-point.

Figure 4.12(a) shows the frequency undershooting in percent as a function of the step in the load set-point. The MPC enables to decrease the frequency drop in the range of 20 - 40 %. Figure 4.12(b) shows the value of the rise time corresponding to each variation of the load set-point. In this case, the rise time is measured as the time required for the frequency to return back to 99.6 % of the steady-state value. Examining the most severe step tests (3 MW and 4 MW), the regulator reacts in 1.7 s and 2.5 s. The feedback controller of the manufacturer takes around 6-times more. On the other hand, the results indicate that similar rise times (< 1.6 s) are to be expected with step variations between 1 MW and 2 MW. However, the controller of the manufacturer induces, in this range of power increments, some periodic oscillations, dampening in around 5 s.

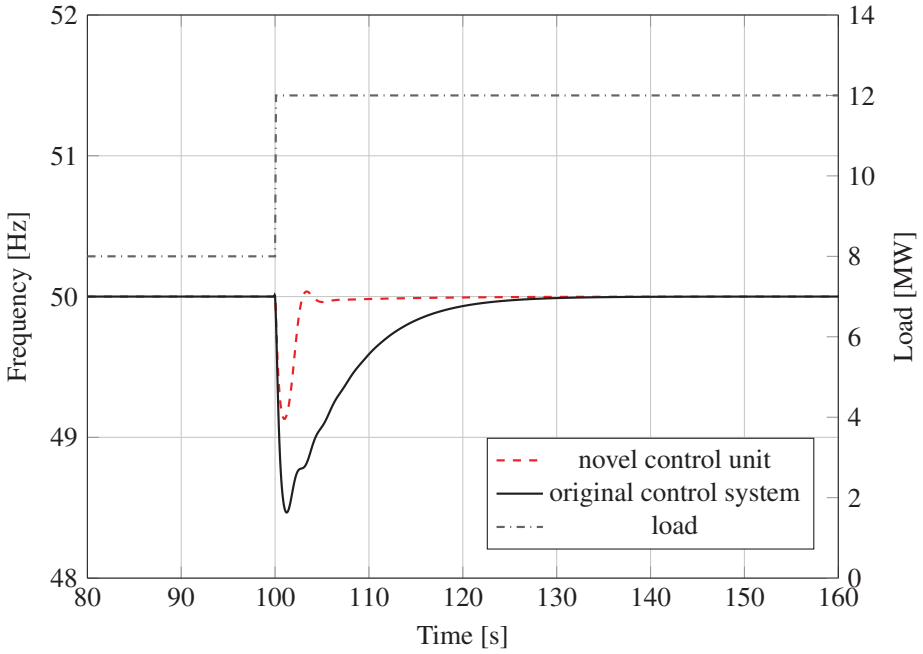

(a)

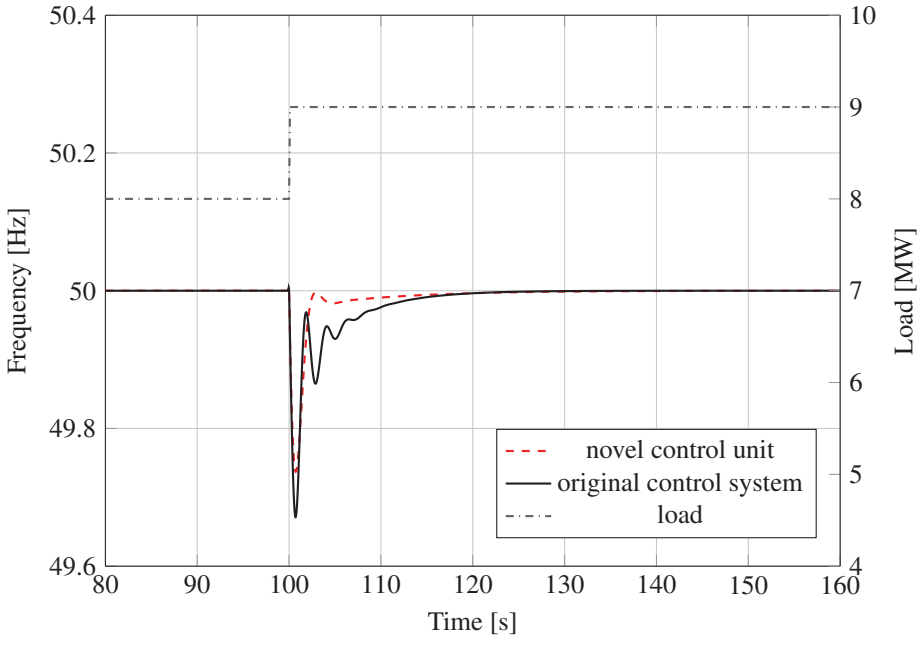

(b)

Figure 4.11: Frequency trends of the gas turbine operated by the model predictive control and the feedback controller of the engine manufacturer. No bottoming cycle is here adopted. 4.11(a) Frequency and load set-point over time for a 4 MW step. 4.11(b) Frequency and load set-point over time for a 1 MW step.

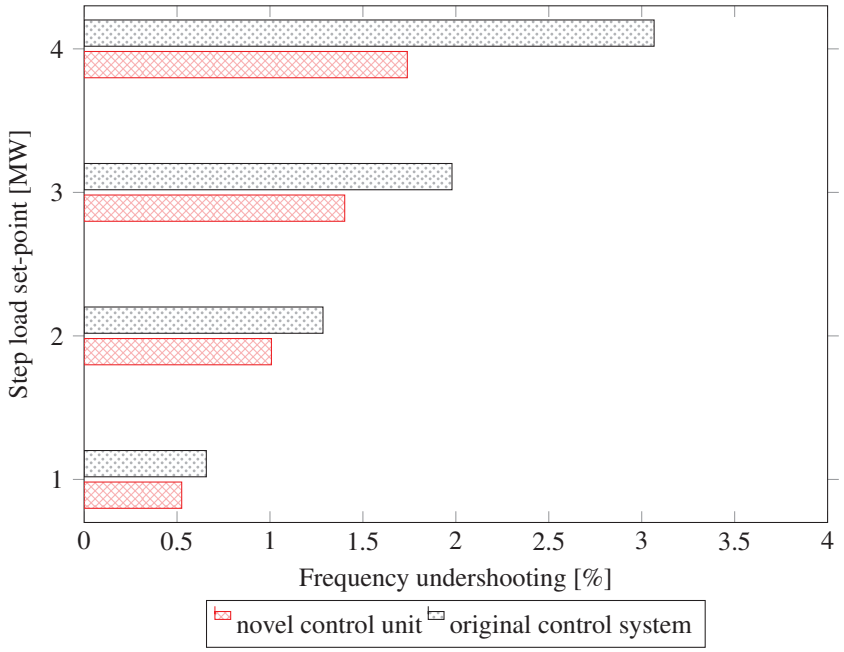

(a)

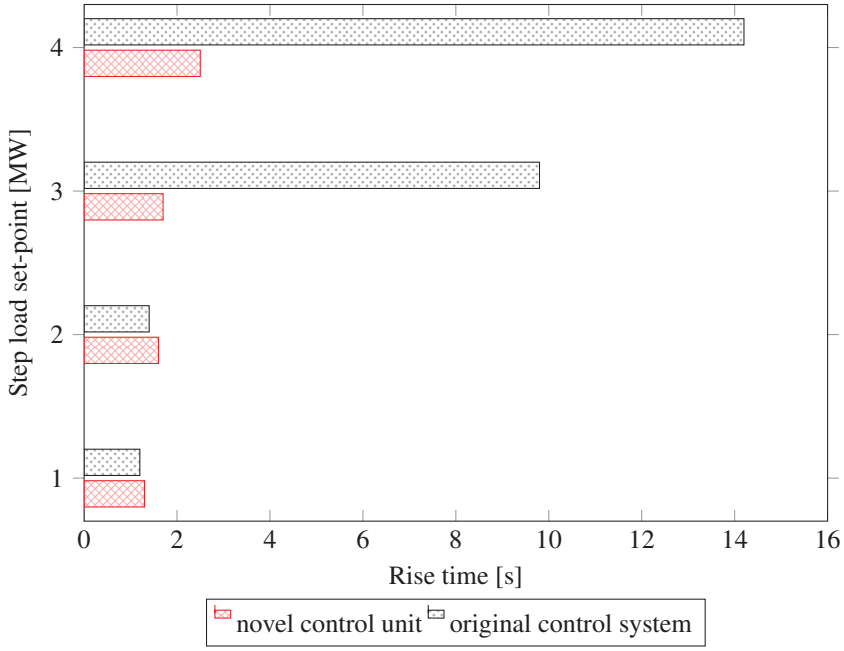

(b)

Figure 4.12: Comparison of the dynamic metrics given by the model predictive control and the feedback controller of the engine manufacturer. Note that no bottoming cycle is here adopted. 4.12(a) Frequency undershooting in percent as a function of the step in the load set-point. 4.12(b) Rise time as a function of the step in the load set-point.

4.3.2 The gas turbine and the ORC unit

The gas turbine is now connected to the ORC turbogenerator. The MPC uses the internal models given in Equations 3.22 - 3.26. The remaining settings for the controller are given in Table 3.6. The sampling time is set to 500 ms, due to the presence of the bottoming cycle unit. The steady-state optimizer is now active. Its task is the identification, for a given load, of the cycle configuration giving the highest thermal efficiency of the plant. Moreover, the unit verifies the feasibility of the working point. Figure 4.13(a) shows how the optimizer tracks the maximum plant efficiency when the power set-point of the combined cycle unit augments by 2 MW. The solid and dotted lines relate the thermal efficiency of the plant to the pump speed. The hollow circles represent the optimal working points. The steady-state optimizer ensures that the system does not operate at turbine inlet temperatures higher than 280 °C (unacceptable risk of cyclopentane degradation), or exhaust gas temperatures colder than 140 °C (large probability of acid formation at the outlet of the once-through boiler). Given the practicability of the working point, the MPC receives the degree of superheating as reference trajectory. The set-point is achieved by adjusting the pump speed. Null-weights are imposed in the matrix $\boldsymbol{Q}$ (see Equation 3.18) for the deviations of the two remaining reference trajectories, i.e., the temperatures at the inlet of the ORC expander and of the exhaust gas stream. It is also underlined that, for combined cycle loads from 30 to 100 %, the degree of superheating delivering the highest efficiency remains close to 35 °C. The optimal pump speed varies form 2200 to 3200 rpm.

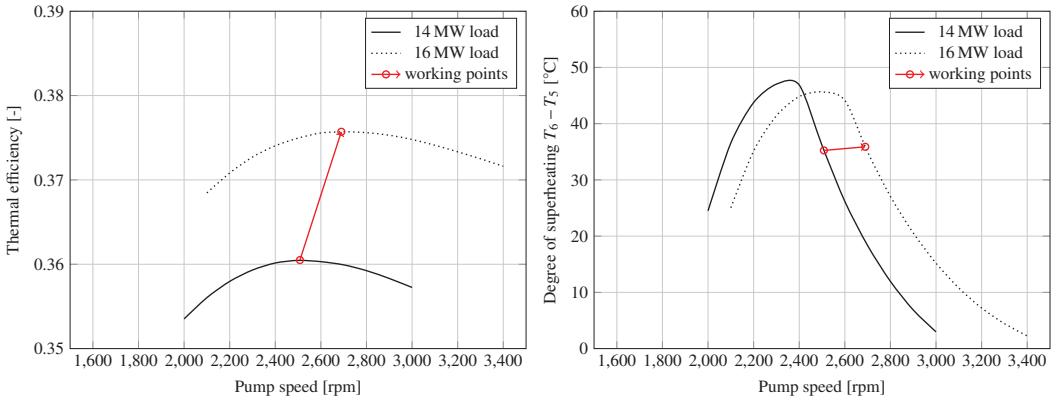

Figure 4.13: Change of load set-point (from 14 to 16 MW) for one gas turbine connected to the ORC turbogenerator. 4.13(a) The steady-state optimizer tracks the peak efficiency of the plant. 4.13(b) Set-point variation of the degree of superheating T_6 - T_5 at the peak efficiency.

The dynamic performance of the power system operated by the new regulator is compared to the one obtained with the control system of the gas turbine manufacturer. A properly-tuned PI controller (proportional gain equal to 1 and integral time equal to 4 s)

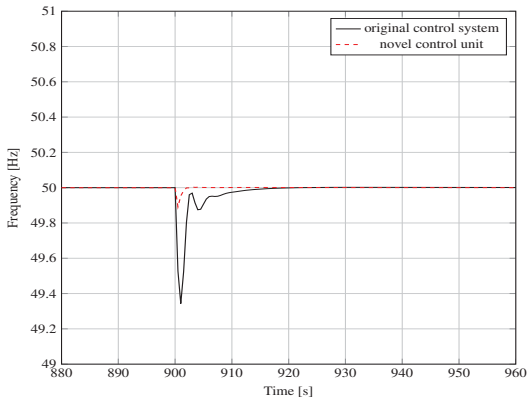

(a) Network frequency

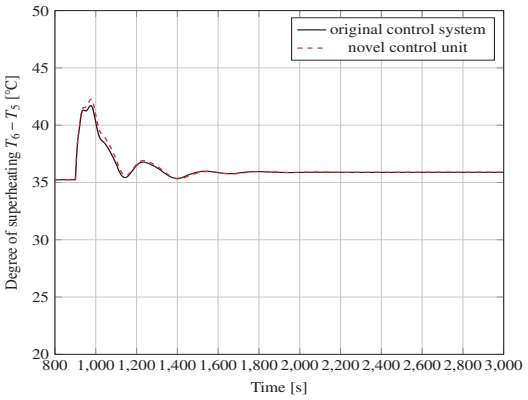

(b) Degree of superheating

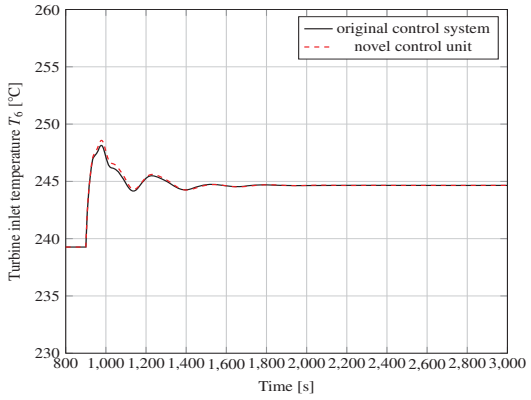

(c) Turbine inlet temperature

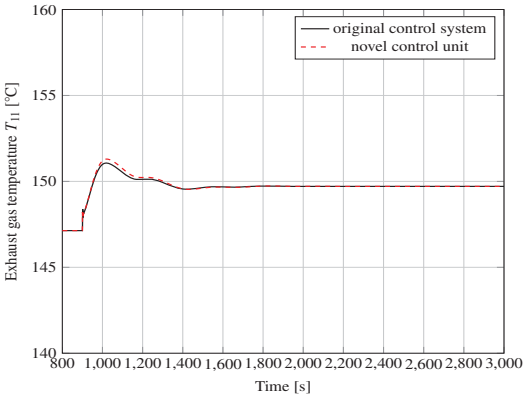

(d) Exhaust gas temperature

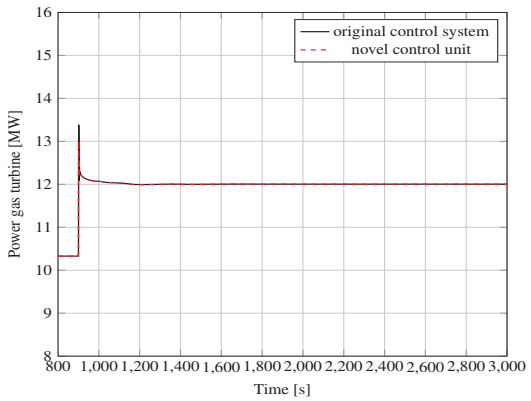

(e) Shaft power of the gas turbine

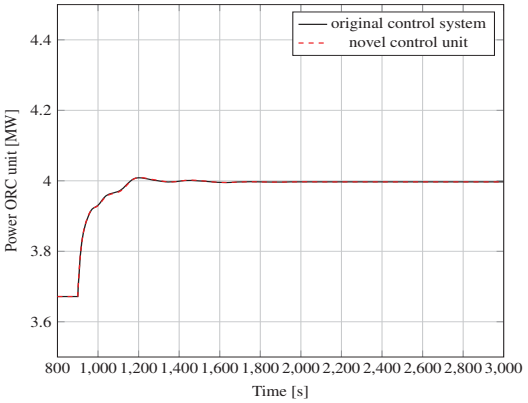

(f) Shaft power of the organic Rankine cycle unit

Figure 4.14: Dynamic responses of the combined cycle unit (gas turbine and ORC module) operated by the model predictive control and the feedback controllers. The power system operates in both cases at the optimal plant efficiency.

adjusts the pump speed. The latter device minimizes the error between the degree of superheating and the optimal set-point. The steady-state optimizer updates the optimal value. The load set-point increments by 2 MW at time t_0 equal to 900 s. Figure 4.14 shows the dynamics of the power system operated by the two devices. Figure 4.14(a) gives the frequency trends as a function of time. The MPC delivers an undershooting of the network frequency around 0.2 % and a rise time of 1.5 s. The same transient metrics for the feedback controllers are 1.3 % and 2.5 s, respectively. The novel regulator can thus abate the response time by around 66 %. Additionally, it can reduce the frequency drop by 0.6 Hz. Figure 4.14(b) shows the variation with time of the degree of superheating. The reference trajectories can be visualized in Figure 4.13(b). This measured output presents an oscillating trend, with an amplitude smoothly dampened when moving to steady-state conditions. The temperature overshooting and the rise time are 45 °C and 230 s, respectively. The temperatures at the inlet of the ORC expander exhibit similar trends. Figure 4.14(c) shows a steady-state temperature gain of 6.0 °C and a peak value lower than 250 °C. As for the exhaust gas temperature, Figure 4.14(d) pinpoints a smoother transition to steady-state conditions compared to the temperatures of the ORC module. The new steady-state value is around 150 °C. The turbine inlet temperature is below the limit of fluid decomposition. The exhaust gas temperature is hot enough to avoid corrosion in terminal part of the OTB. Figures 4.14(e) and 4.14(f) show the mechanical powers of the power turbine and the axial expander serving the ORC unit as a function of time. The different time constants of the two thermal engines are clearly visible. The gas turbine adapts almost instantaneously (in less than 20 s) to the set-point variation. Afterwards, small and slow steps in the valve position compensate for the increasing power coming from the ORC system.

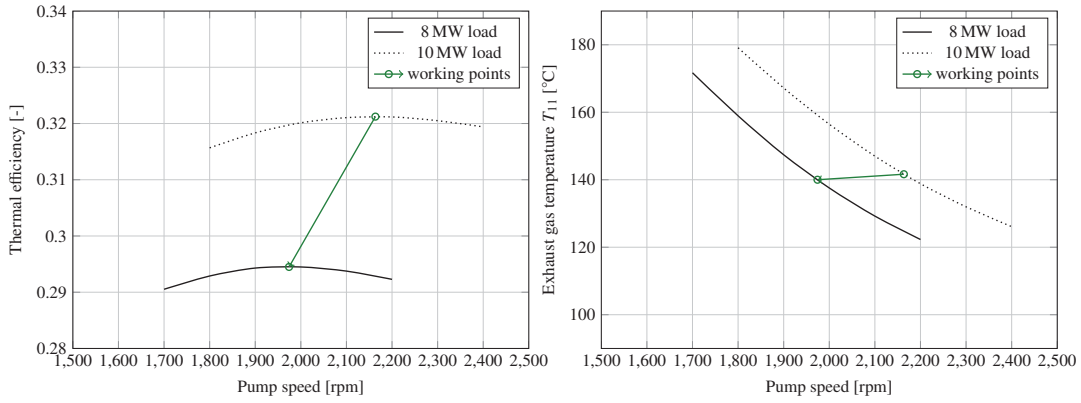

Figure 4.15: Change of load set-point (from 10 to 8 MW) for one gas turbine connected to the ORC turbogenerator. 4.15(a) The steady-state optimizer switches the operational strategy from peak efficiency to constant exhaust gas temperature. 4.15(b) Variation of the exhaust gas temperature T_{11}. The new reference trajectory transmitted to the MPC is equal to 140 °C.

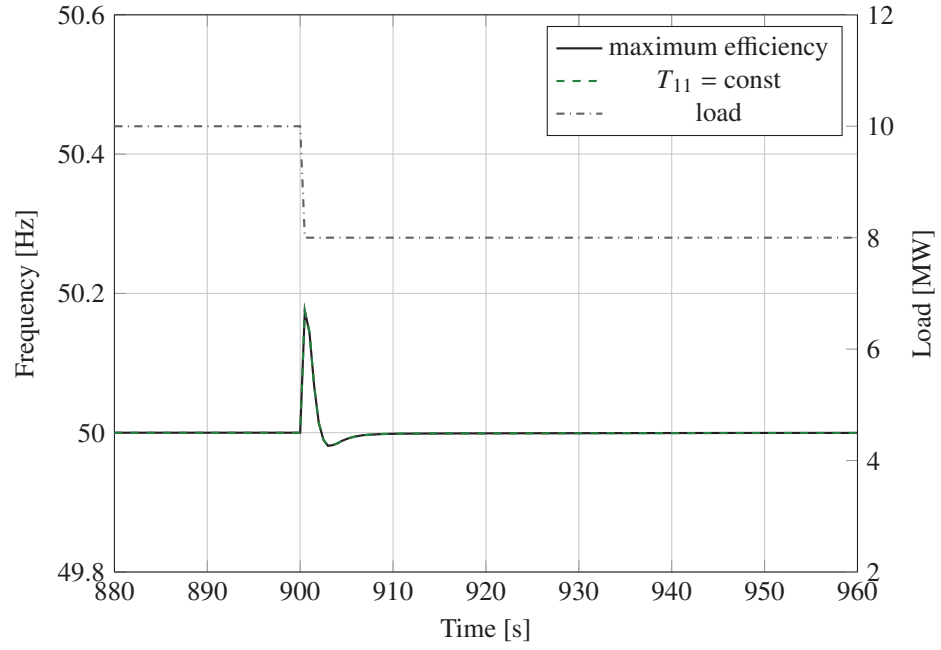

(a)

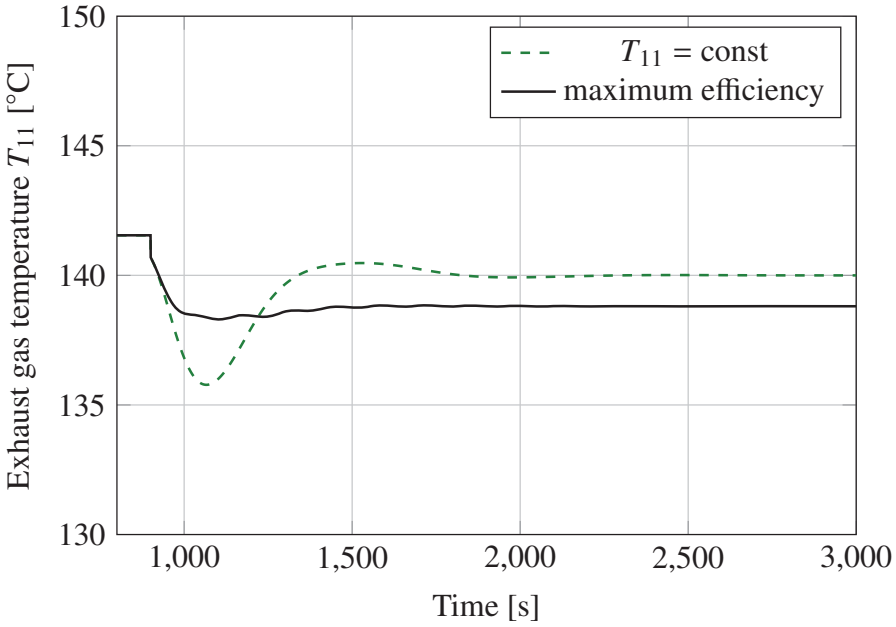

(b)

Figure 4.16: Dynamic responses of the combined cycle unit (gas turbine and ORC module) operated by the novel regulator. The solid and dotted lines refer to two different control modes, i.e., operation at peak efficiency and constant exhaust gas temperature. 4.16(a) Frequency and load set-point over time for a −2 MW step in the power demand. 4.16(b) Exhaust gas temperature as a function of time.

Figure 3.18 shows that the lower the power output of the combined cycle unit the colder the exhaust gas temperature. The limit for acid formation is not a criticality for loads larger than 40 %. On the contrary, tracking the maximum performance at lower capacities leads to working conditions potentially harmful for the once-though boiler. Therefore, the steady-state optimizer detects the infeasibility of the cycle configuration at low power activities. It then switches the operational strategy to constant exhaust gas temperature. This is practically carried out by resetting the weights on the measured outputs. Figure 4.15(a) relates the thermal efficiency of the plant with the pump speed for the initial and final load. Initially, the plant supplies 10 MW operating at the peak efficiency, see the hollow circle on the dotted line. The load of the combined cycle unit decreases then by 2 MW. The part-load activity is now performed at a fixed exhaust gas temperature of 140 °C, see Figure 4.15(b).

Figure 4.16(a) reports the frequency responses over time obtained operating the plant at the highest plant efficiency and at constant exhaust gas temperature. Changing the control strategy of the ORC turbogenerator does not produce any significant difference in the network frequency. Figure 4.16(b) shows the exhaust gas temperature as a function of time for the two control modes. The solid line indicates that, at around 40 % load, the optimal working point of the plant entails a temperature T_{11} lower than 140 °C. The plot also demonstrates that controlling the exhaust gas temperature induces an undershooting lower than 10 °C.

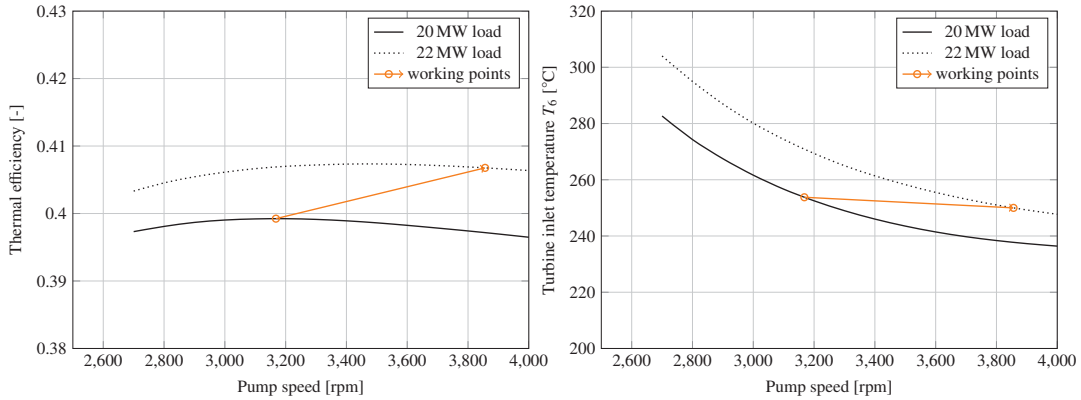

Figure 4.17: Change of load set-point (from 20 to 22 MW) for one gas turbine connected to the ORC turbogenerator. 4.17(a) The steady-state optimizer switches the operational strategy from peak efficiency to constant turbine inlet temperature. 4.17(b) Variation of the turbine inlet temperature T_6. The new reference trajectory transmitted to the controller is equal to 250 °C.

At power capacities near the design-point (≈ 22 MW), the system can operate at the maximum efficiency with limited risk of decomposition for the working fluid, see Figure 3.18. Harmful temperatures for cyclopentane are encountered running the plant at power duties larger than 120 % the nominal load. Operations at fixed turbine inlet tem-

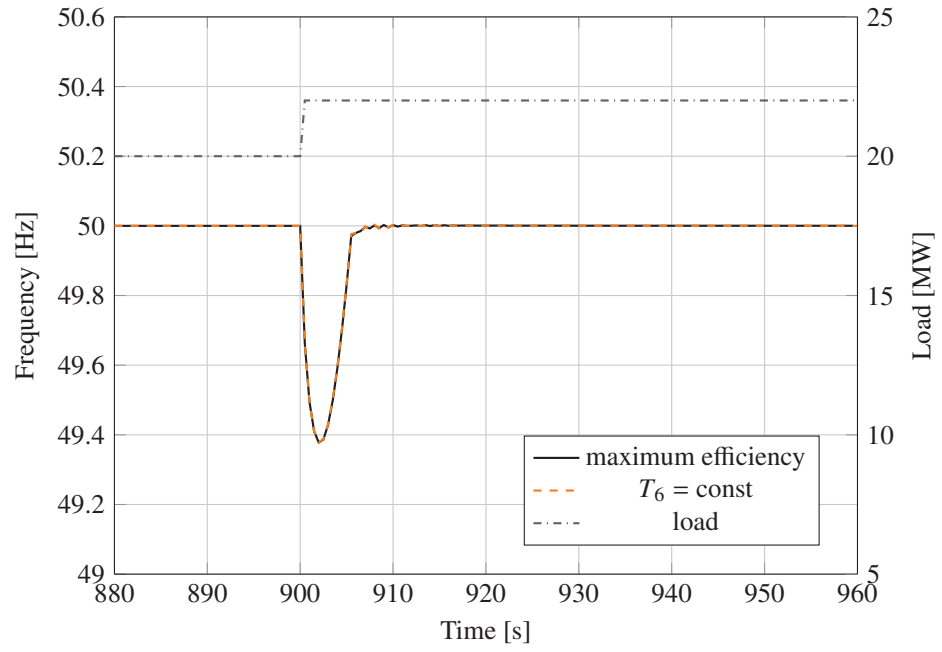

(a)

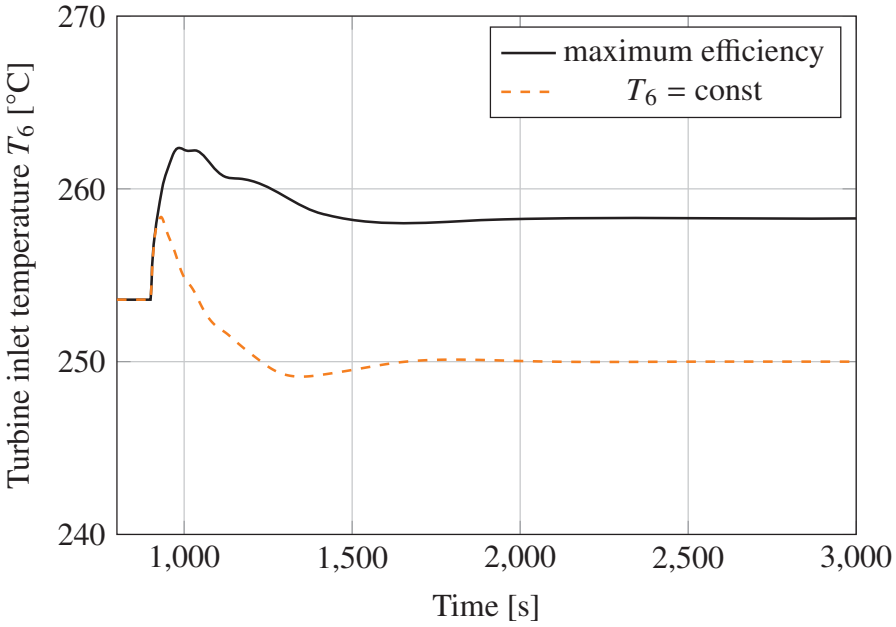

(b)

Figure 4.18: Dynamic responses of the combined cycle unit (gas turbine and ORC module) operated by the novel regulator. The solid and dotted lines refer to two different control modes, i.e., operation at peak efficiency and constant turbine inlet temperature. 4.18(a) Frequency and load set-point over time for a 2 MW step in the power demand. 4.18(b) Temperature at the inlet of the expander as a function of time.

perature are simulated, as aging of the plant constituents and of the working fluid itself modifies the position of the optimal running point. Moreover, the platform operator can select this control strategy to monitor the highest temperature of the working fluid. Figures 4.17(a) and 4.17(b) show the running points (hollow circles) obtained by increasing the load from 20 to 22 MW. The controller switches the strategy from optimal thermal efficiency to fixed turbine inlet temperature. The variation of the operational mode takes place by imposing a null-weight on the degree of superheating and a weight of $5 \cdot 10^3$ on the temperature T_6. Its set-point is assumed to be 250 °C.

Figure 4.18(a) shows the variation of the power set-point and the frequency response, operating the system at the peak efficiency and at fixed turbine inlet temperature. The frequency response is again independent from the operational strategy of the bottoming cycle unit. Figure 4.18(b) shows that the temperatures at the inlet of the ORC expander present different trends and steady-state values. The tracking of the set-point (250 °C) limits the undershooting of the measured output to approximately 5 °C. Following the maximum efficiency entails a peak temperature of almost 265 °C. Note that both control modes deliver smooth and well-dampened responses with a rise time of around 260 s.

Chapter 5

Discussion

This chapter discusses the findings of the thesis, their practical implications and the uncertainties of the model results. The first part deals with the identification of the optimal waste heat recovery technology and best working fluid. Subsequently, the chapter focuses on the system dynamics and the reasons which lead to discard the ORC design candidates. Finally, the performance and the stability of the control system are discussed.

5.1 Steady-state multi-objective optimization

This section addresses the research questions i) and ii). The aim is to determine the optimal bottoming cycle technology using the results of the multi-objective optimization. Additionally, relevant design features are discussed so as to identify the ideal ORC fluid candidate. Economically infeasible and low-efficiency alternatives are excluded. The section concludes quantifying the uncertainties of the steady-state analysis.

5.1.1 The optimal waste heat recovery technology

The two-dimensional Pareto fronts reported in Figures 4.1 and 4.5 show a hyperbolic tendency binding the weight to the CO_2 emissions. Larger heat transfer areas (i.e. weight) give the possibility to recuperate more heat from the gas turbine and to lower the heat transfer irreversibility in the heat exchangers. This allows improving the performance of the combined cycle units. The curve is, however, non-linear. At the extremes of the graphs, small increments in one variable correspond to large variations of the second metric. For instance, the heat transfer area of the once-through boiler grows rapidly at low CO_2 emissions due to the decreasing logarithmic mean temperature difference, see Equation 3.3. This hyperbolic tendency is in agreement with a number of parametric studies relating the UA-value to the evaporating temperature, see, e.g., Wang et al. [12] and Erhart [5].

Figures 4.2 and 4.6 show the presence of a system design which maximizes the economic revenue of the bottoming cycle technology. This tendency originates from the two conflicting terms (i.e. incomes and investment cost) determining the net present value, see Equation 3.5. An optimum is reached since the NPV is a function of the plant cost and of the yearly fuel and CO_2 savings. Starting from low weights, small increases of the yearly energy conversion efficiency improve significantly the NPV. After the maximum, enhancing the performance of the bottoming cycle modules by increasing the area of the heat transfer equipment diminishes the economic revenue. The total investment cost becomes excessively large.

Table 4.1 pinpoints that the optimal configurations of the steam Rankine unit fall in a limited range of both design variables and objective functions. The small dispersion of the exhaust gas temperature (RSD $< 1\,\%$), which determines the heat input to the engine, is the major responsible for the uniformity of the system designs. Furthermore, the presence of liquid at the turbine outlet in all design candidates deteriorates the expander efficiency. It also limits the evaporating pressure of the SRC unit to approximately 14 bar. The algorithm discards all design solutions operating at higher pressures, as explained in Section 3.3. The vapor quality reaches the defined limit of 84 %. Such phenomenon could lead to unacceptable mechanical stresses on the blades of the latter turbine stages.

Figure 4.1 shows that the organic Rankine cycle is the technology achieving the highest reduction of CO_2 emissions and fuel consumptions, i.e., 13.0 %. The relatively low exhaust gas temperature (379.2 °C) of the gas turbines and the variety of the system designs allow this combined cycle plant to deliver maximum design efficiencies around 42.0 %. From this perspective, findings discourage the exploitation of ABC units, as the gains in performance are half of those of the ORC unit. The causes are the large

work expenditures to run the two-stage compression process and the relatively high temperature (155.0 °C) of the air exiting the power turbine. The efficiency indicators of the steam Rankine module situate this technology in the second position behind the ORC turbogenerator.

The ABC plant features extremely low weights of the heat transfer equipment. This is due to the open-cycle configuration and to the high compactness offered by the finned-plate heat exchanger. The design results are in accordance with the values obtained by Bolland et al. [1] for the design of a finned-plate heat exchanger recuperating the exhaust heat from the LM2500 gas turbine. Weight and compactness of the SRC unit are to a large extent comparable to those of the ORC turbogenerator. Various surveys (e.g. Quoilin et al. [10]) argued that hydrocarbon fluids enable to manufacture more compact units compared to steam, owing to the higher fluid density and the lower degree of superheating. These potential benefits are not fully observable in this case. In fact, the higher mass flow rate ($\approx 40\,\mathrm{kg \cdot s^{-1}}$) circulating in the ORC module, compared to that of the SRC unit $\approx 7\,\mathrm{kg \cdot s^{-1}}$, compensates for the higher average fluid density and the shorter superheating section achieved by cyclopentane. On the other hand, Table 4.1 indicates that the tube diameters of the preheater-evaporator and superheater are almost equal. This feature can facilitate the implementation of once-through boilers with constant tube diameter. It is also highlighted that, as a practical implication, Table 4.1 provides to the designer figures for the optimal geometry of the heat transfer equipment. Hence, since the dimensions for heat exchangers are standardized, the designer can select the closest commercially available value.

Findings suggest that the technology achieving the largest economic revenue is the steam Rankine cycle. The ORC technology exhibits a lower economic revenue, despite the higher savings of combustible and CO_2 emissions. The increased incomes are not sufficient to justify the higher equipment expenses. The SRC unit is lighter than the ORC turbogenerator, considering the designs located at the maximum NPV. Nonetheless, Figure 4.2 shows that the net present value is sufficiently flat in the vicinity of the peak. Such trend may lead the plant designer to prioritize the system compactness by slightly sacrificing the economic revenue. Figure 4.2 pinpoints a more scattered trend for the net present value of the ABC unit compared to those of the organic and steam Rankine engines. This tendency has two reasons: i) the PEC of the air bottoming cycle unit is governed both by the two compressors and the three turbines, whereas the cost of the SRC and ORC modules primarily relates to the expander and the once-through boiler, and ii) the expressions employed to evaluate the purchased-equipment cost of the turbomachinery are a transcendental function of both mass flow rate and pressure ratio.

5.1.2 The best working fluid

Benzene gives the largest reduction of fuel consumption and CO_2 emission (14.0 %). Cyclopentane delivers similar performances and weights. The CO_2 reductions are around 4.0 %-points lower for the other hydrocarbons. The efficiency ranking is in accordance with a number of parametric studies [3, 11, 13] on ORC units operating at maximum temperatures from 250 to 350 °C. The lightest and cheapest unit uses cyclopentane as working fluid at the economic optimum. It is underlined that plant manufacturers are currently charging this hydrocarbon in operating ORC turbogenerators of similar sizes, see, e.g., Del Turco et al. [4] and Gaia and Bini [6]. Cyclohexane and isopentane should be avoided, since they lead to negative economic revenues.

Table 5.1 lists, for each fluid candidate (water is also included), the power output of the bottoming cycle unit, the condensing pressure and the Prandtl number of the liquid in single-phase flowing in the preheater section of the once-hough boiler. The volumetric flow ratio, the size parameter and the purchased-equipment cost per unit of power are also reported. The listing order of the hydrocarbons is for decreasing net present values. The investment cost of the expander strongly relates to the size parameter, see Equation A.21. Isopentane and cyclopentane present the smallest size parameters and, accordingly, the lowest specific costs. However, the latter hydrocarbon achieves higher plant power outputs, ultimately leading to a more favorable economic revenue. Benzene delivers economically feasible modules by virtue of the high design- and part-load performance, despite exhibiting the second largest size parameter. Economic and performance indicators suggest to discard cyclohexane and isohexane. Note that, from a practical perspective, cyclopentane and isopentane have the advantage (especially compared to water) of condensing above atmospheric pressure. This feature can avoid

Table 5.1: Thermodynamic and transport properties (power output, condensing pressure and Prandtl number) of the organic fluid candidates and turbine metrics (volumetric flow ratio, size parameter and specific equipment cost). Water is also included.

Fluid	$\dot{\mathbf{P}}_{\mathrm{GENA2}}$ [MW]	$\mathbf{p}_1$ [bar]	**Pr**[1] [−]	$\dot{\mathbf{V}}_7/\dot{\mathbf{V}}_6$ [−]	$\sqrt{\dot{V}_7}/\Delta h_{is}^{1/4}$ [cm]	$\overline{\mathbf{PEC}}_t$ [$/W]
Water	4.6	0.12	1.4	48.3	29.0	0.240
Cyclopentane	4.8	1.03	3.1	25.2	19.6	0.239
Benzene	4.8	0.36	3.7	39.5	24.3	0.310
Isopentane	4.0	2.05	3.1	10.2	17.4	0.251
Isohexane	4.1	0.72	3.5	20.9	22.4	0.327
Cyclohexane	4.3	0.36	3.9	24.9	25.6	0.367

[1] The value of the Prandtl number is reported as the average value in liquid phase of the preheater section of the once-hough boiler.

inward air leakage into the condenser. The design-point optimization of the organic compounds gives analogous geometries for the heat transfer equipment. This fact is due to the similarity of the thermodynamic and transport properties of the working fluids.

5.1.3 Uncertainties

As stated in Section 3.3, the weight calculation is limited to the heat transfer devices. An accurate weight calculation of the turbomachinery serving the bottoming cycle units is presently beyond the capability of the developed models. Nonetheless, proprietary information made available by ORC manufacturers indicates that the contribution of the turbine and the electric generator is typically around 30 % of the weight of the heat transfer equipment. The same share is to be expected for the SRC unit. The figures for the turbomachinery and the intercooler of the ABC module are comparable with those of the finned-plate heat exchanger [1]. These approximations suggest that the Brayton module may become less competitive, considering the significant contribution of the turbomachinery on the package weight.

A limitation of the presented approach is the assumption of constant isentropic efficiency for the turbomachinery serving the bottoming engines. In single-stage axial machines, lower losses are to be expected for hydrocarbons compared to steam, by virtue of the lower volumetric flow ratios [8]. This benefit is particularly evident using isopentane, see Table 5.1. Considering the size parameter (≈ 50 cm) and the volumetric flow ratio (≈ 50) of the steam turbine, a two-stage expander would be recommendable to reach the assumed isentropic efficiency (80 %). Additionally, the cost of the expander of the SRC unit should be related to the number of stages. These limitations could be tackled by devising price equations for single- or two-stage steam turbines and integrating the turbine design with the multi-objective optimization procedure.

The designs of the heat transfer equipment are derived using various correlations, all of which are associated with uncertainties. The assumptions that have the largest influence on the results are the equations used to estimate the heat transfer coefficients and the pressure drops. As an example, in evaluating heat transfer coefficients, average variations of 15 - 20 % and maximum deviations of about 40 % are to be expected [2]. These uncertanties strongly influence the weight calculation. A sensitivity analysis is thus performed, to quantify the impact of the variations in heat transfer coefficients and pressure drops. The optimal set of variables of the Pareto fronts shown in Figures 4.1 - 4.6 is given. The heat transfer coefficients on the cold and hot side of each heat exchanger are varied by -20 % and 20 %, respectively. When varying the heat transfer coefficient on the gas side of the OTB (which has the largest impact on the weight

estimation), the highest relative deviations span from -10.5 % (-10.4 t) to 6.6 % (8.1 t). On the contrary, the influence of the uncertainties on the daily CO_2 emissions and economic revenue is negligible. A ±20 % variation of the pressure drops on the hot side of the water-cooled-condenser or of the recuperator leads to a change in the daily CO_2 emissions lower than 1.0 %. No significant difference is observed in the estimation of the weight and net present value. Lower deviations are noticed modifying the pressure drops on the cold side of the once-though boiler. As for the finned-plate heat exchanger serving the ABC unit, ±20 % changes of the heat transfer coefficient on the air side lead the weight to span from -10.8 % (-5.0 t) to 18.2 % (8.4 t). No main deviation is observed on the three objective functions, modulating the pressure drops on the cold side of the FPHE from -20 to 20 %.

5.2 Dynamics as design criterion

Figures 5.1(a) and 5.1(b) show a new version of the two-dimensional Pareto fronts relating the CO_2 emissions and the net present value with the weight. The bottoming cycle unit is the organic Rankine cycle. Based on the results disclosed in Section 4.2, design candidates exceeding the limit of the frequency undershooting are deemed infeasible from a dynamic perspective, see the points marked with the ○ symbol in the plots. Modules heavier than 100 t are also discarded from the Pareto frontier, due to weight constraints on the Draugen platform.

Figure 5.2(a) shows the power delivered by the electric generator of gas turbine A over time after the failure of engine B. The trends are given for the two designs characterized by the maximum and minimum weight of the heat transfer equipment. The transient characteristics are similar. Slightly larger fluctuations, caused by the saturation of the feedback controller (i.e. the upper limit of the valve position is reached), appear for the design with the lowest weight. The power increment of engine A in steady-state conditions differs by around 0.4 MW for the two designs. Light units entail a lower amount of power supplied by the bottoming unit. Therefore, the share provided by the gas turbine (or, in other words, the opening of the fuel valve) has to increase more compared to the case of heavier ORC engines. This phenomenon is responsible for the larger undershooting of the frequency in light and low-power ORC turbogenerators. Figure 5.2(b) shows the load increment covered by engine A as a function of the weight. The value, given as a percentage of the nominal load of the gas turbine (i.e. 16.524 MW), is calculated observing the engine power in steady-state conditions before and after the trip of gas turbine B. The lighter the ORC module the larger the load variation of engine A and the frequency undershooting. Efficient and heavier units are thus preferable to reduce the frequency excursions and rise times.

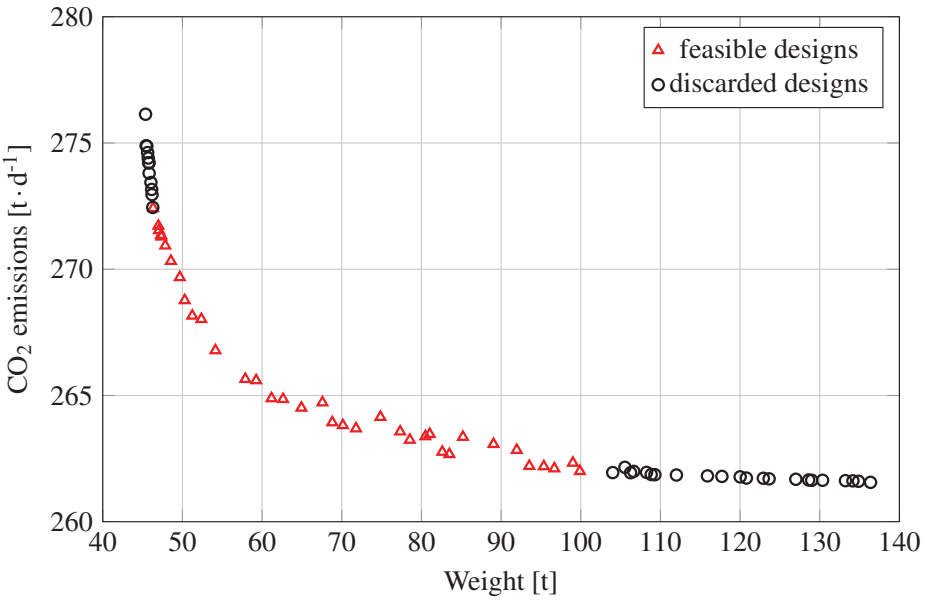

(a)

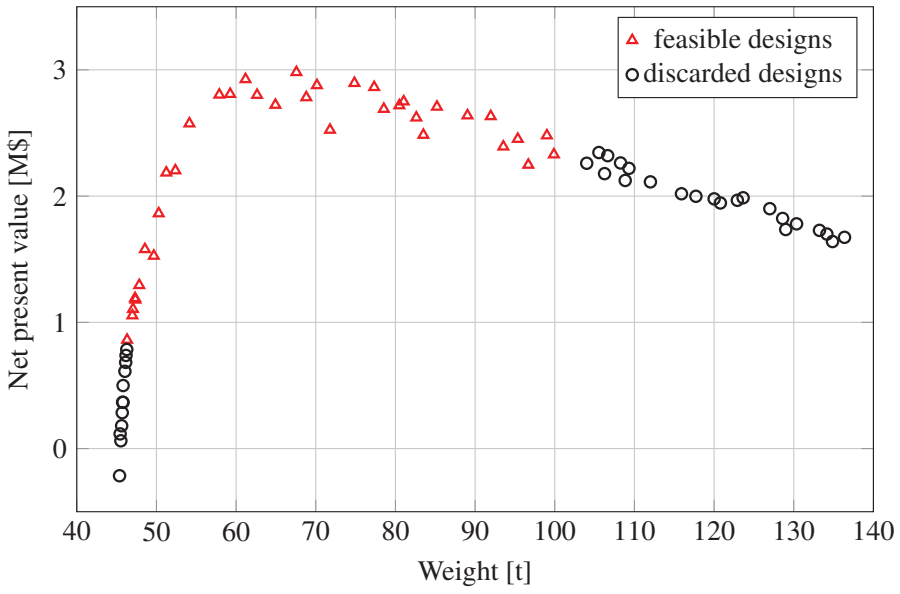

(b)

Figure 5.1: Two-dimensional Pareto fronts filtered using dynamic metrics and weight constraints. The designs identified by the ○ symbol are discarded due to the unacceptable frequency undershooting > 3.8 %. Candidates with a weight larger than 100 t are also considered infeasible. 5.1(a) Daily CO_2 emissions versus weight. 5.1(b) Net present value versus weight.

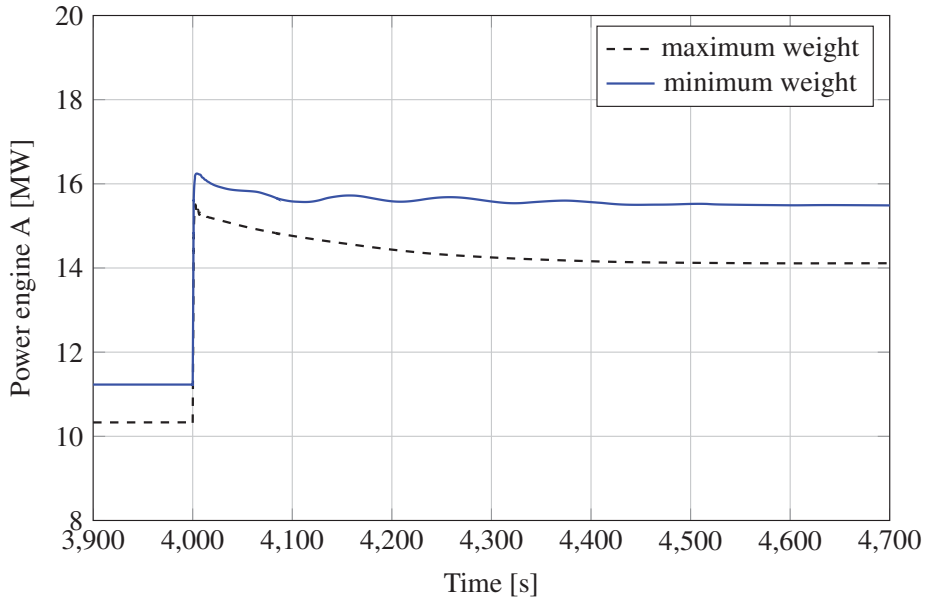

(a)

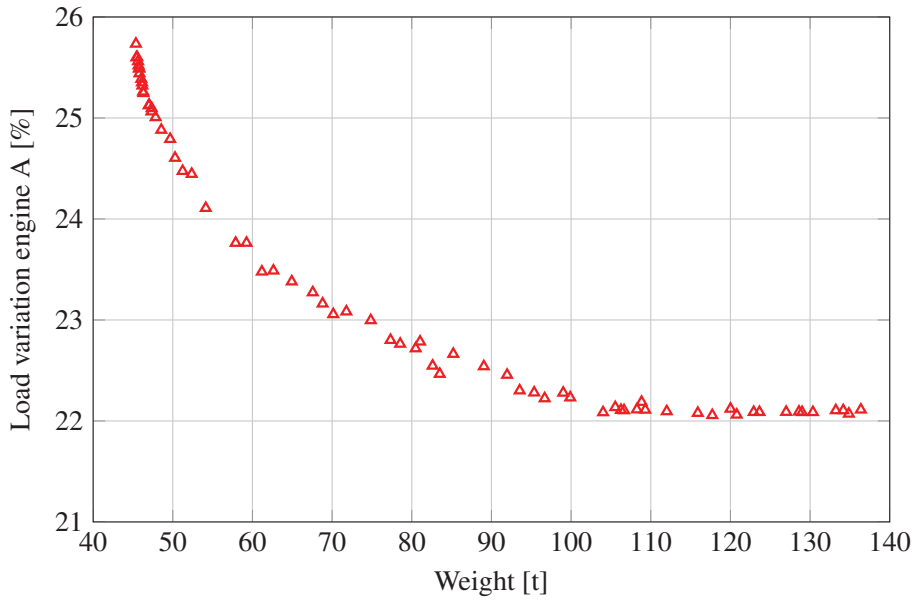

(b)

Figure 5.2: Dynamics of engine A. 5.2(a) Electric power produced by gas turbine A versus time for the two designs characterized by the maximum and minimum weight. 5.2(b) Percentage variation of the load of engine A versus weight. The values in the ordinate are normalized using the nominal power of the engine, i.e., 16.524 MW.

The diversity in the thermal inertia of the heat transfer equipment is also crucial to characterize the transient response of the bottoming cycle unit. In this regard, Figures 4.10(a) and 4.10(b) pinpointed two operational issues: i) the instabilities of the turbine inlet temperature with low-weight ORC modules, and ii) the high risk of cyclopentane decomposition for some design candidates. As regarding the latter problem, Figure 5.3(a) relates the turbine inlet temperature at design-point to the weight. Note that this variable represents the set-point of the PI controller regulating the rotational speed of the pump. Light units have the lowest design-point temperature with a minimum of 230 °C. Accordingly, the maximum turbine inlet temperature reached during the trip of engine B is minimized. The set-point of the PI controller presents a maximum value of 275 °C at around 80 t. It stabilizes to 270 °C at larger weights. This trend and the different thermal inertia of the engines are responsible for the high values of the temperature overshooting between 50-90 t.

Figure 4.10(a) demonstrated some instabilities in the dynamics of the turbine inlet temperature for the lightest ORC module. Figure 5.3(b) shows the vapor quality of cyclopentane at the first nine volumes of the once-though boiler (only odd cells are shown). Focusing on the foremost mass of fluid, the plot indicates that, before the trip of engine B, cyclopentane enters the primary heat exchanger in subcooled liquid conditions. Afterwards, the load set-point of the combined cycle plant increases. The quality in the first volume shows traces of vapor at the OTB inlet. Moreover, Figure 5.3(b) indicates the presence of two-phase flow in all the first eight volumes. These cells were in liquid state before the transient event. Initially, the ninth cell holds the fluid in vapor-liquid equilibrium. All volumes contain, instead, subcooled liquid in the new steady-state. The rapidly varying quality of the stream entering the once-through boiler induces abrupt changes in the thermodynamic and transport properties of cyclopentane. This, ultimately, perturbs the time-dependent terms of mass and energy balances, and it causes the instabilities observed in Figure 4.10(a). The phenomenon is more severe in low-weight modules (< 50 t). These units operate at low evaporating pressures and with large area of the OTB in vapor-liquid equilibrium (refer to the $T - s$ diagram in Figure 3.1(b)). This feature facilitates the onset of steep variations of the fluid properties.

The dynamic results presented in this work are, as for the steady-state calculations, affected by model inaccuracies. In this regard, the risk of fluid decomposition is associated to the temperature at inlet of the ORC expander. However, the most severe overheating is experienced in the fluid layer close to the last tube walls of the primary heat exchanger. Design-point calculations using the detailed methods outlined in Section 3.1.2 indicate that the wall temperature of cyclopentane in the hottest part of the OTB is expected to be 10-30 °C higher than the corresponding bulk value. Moreover, the evaluation of the heat transfer coefficients in the dynamic and part-load studies is performed with the simplifications described in Section 3.1.3. Therefore, the estimation of the temperature profiles inside the OTB and of the turbine inlet temperature has

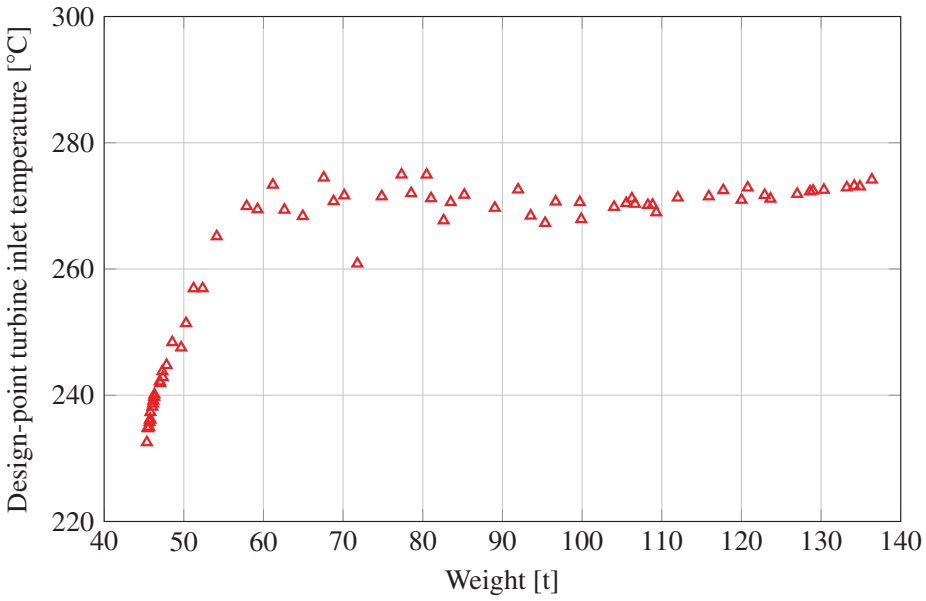

(a)

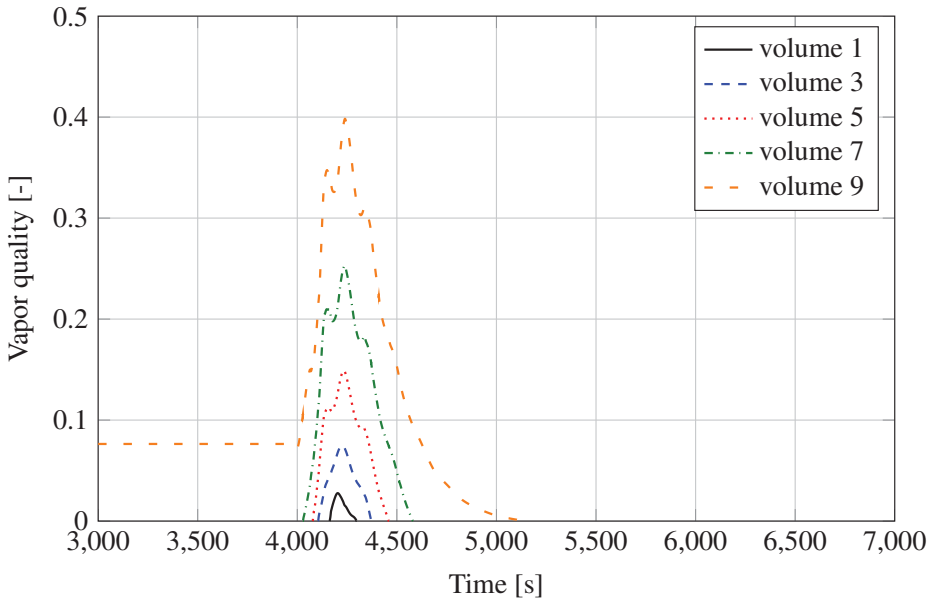

(b)

Figure 5.3: Dynamics of the organic Rankine cycle unit. 5.3(a) Turbine inlet temperature at design-point for the candidates selected by the multi-objective optimization. 5.3(b) Time evolution of the vapor quality at the first volumes of the once-through boiler after the trip of engine B. The design of the bottoming cycle unit is the one corresponding to the minimum weight of the heat transfer equipment.

a certain degree of uncertainty. The ongoing implementation of detailed heat transfer correlations and of the cross-flow topology (see the object diagram of the OTB shown in Figure 3.8) will enable to draw more accurate and quantitative conclusions. Nevertheless, the results obtained here are deemed reliable due to the use of in-depth validated dynamic tools, refer to Section 3.5. The findings of the experimental work by Ginosar et al. [7] were used to set the operational limit for the fluid decomposition. However, the survey method proposed by Pasetti et al. [9] has recently suggested the use of more conservative values, i.e., 275 °C. Proprietary information of ORC manufacturers and different operational constraints could thus vary the outcomes of the procedure aiming at identifying infeasible design candidates. Nonetheless, this work demonstrates the applicability of the methods embedded in the DYNDES tool, without loss of generality, regardless the specific bounds selected for the presents analysis.

5.3 The control system

This section discusses the results of the novel regulator coupling the model predictive control unit and the steady-state performance optimizer. The faster response given by the MPC unit is motivated by examining the dynamics of the control variables. The benefits of operating the system at the maximum efficiency are also quantified. Finally, the stability of the control action is verified by observing the performance of the controller in the presence of large unmeasured disturbances.

5.3.1 Comparison with conventional control systems

The results shown in Figure 4.12 indicate that the proposed control system delivers faster and smoother responses for a wide range of load set-points compared to the controller designed by the engine manufacturer. These advantages are particularly evident at large load changes. Considering one single gas turbine, the novel regulator decreases the frequency drop by 40 % and the rise time by more than 10 s for a step in the power set-point of 4 MW. The better performance is due to the feed-forward action. The internal models allow the controller to immediately counteract the measured disturbance. Conversely, the feedback system cannot deliver its control action until a deviation from the set-point is observed. Figure 5.4(a) shows the variation of the valve opening (manipulated variable) produced by the two control systems over time. The load set-point (measured at terminals of the electric generator) varies from 8 to 12 MW at time $t_0 =$ 100 s. The feedback loop does not react (constant valve position), until, at time $t_1 = t_0 + t_s$, the sensors detect the frequency deviation and transfer the information to the

control loop. The MPC unit increases the fuel flow at time $t_0 = 100\,\text{s}$ using the equations relating the measured disturbance and the valve position to the frequency of the grid. Moreover, even though both controllers reach the same maximum valve opening (0.6808), the MPC unit presents a smoother transition moving towards steady-state conditions.

Figure 5.4(b) gives the valve position of the two controllers as a function of time. The gas turbine is connected to the ORC turbogenerator. The load increments from 14 to 16 MW. The pump speed tracks the highest efficiency of the plant. The MPC unit opens the fuel valve earlier than the controller of the manufacturer, leading to a larger overshooting of the valve opening. This enables to limit the frequency undershooting to 0.2 % of the nominal value. The benefits of the model predictive control are more evident compared to the operation of the gas turbine alone. The reduction of the frequency undershooting and rise time is around 80 % for the selected step change. The engine manufacturer designed and tuned the control system to manage the operation of the topping unit. The original controller was not modified neither tuned. Therefore, larger improvements are expectable, when applying the new regulator to the combined cycle unit compared to the gas turbine alone.

Figures 4.14(b) - 4.14(f) demonstrate that the dynamics of the bottoming cycle unit does not change significantly with the controller. This fact can be explained by observing the change of the manipulated variable. Figure 5.5 shows the pump speed as a function of time for the PI controller and the MPC unit. The step in the load set-point is 2 MW. The actions delivered by the two controllers are equal. The model-based approach does not lead, in this case, to a faster tracking of the optimal degree of superheating. The transient response of the ORC module depends on the dynamics of the exhaust gases and on the pump speed. Given a positive step in the power set-point, the stream exiting the topping engine undergoes a rapid and relatively large increment of both mass flow rate and temperature. The contribution of the pump speed is lower in magnitude. Moreover, its impact on the system response is marginal. Note also that this manipulated variable is adjusted at a slower rate compared to the valve position. Anticipating the regulation of the pump speed by using a feed-forward approach does not meliorate the dynamics of the bottoming unit. Its response is dominated by the topping unit. Nonetheless, the use of the MPC enables to switch automatically among different control strategies, varying the weights of the matrix $\boldsymbol{Q}$ in Equation 3.18. The tuning of three separate PI controllers can thus be avoided. Furthermore, the MPC can treat directly (see the system of Equations 3.19) the constraints on the measured outputs, as well as on the manipulated variables and their rates.

Figure 5.6 shows the thermal efficiency of the combined cycle unit as a function of the pump speed. The power demand on board is supplied running gas turbine A and the ORC unit in parallel with engine B. The load of the combined cycle is equal to 14 MW.

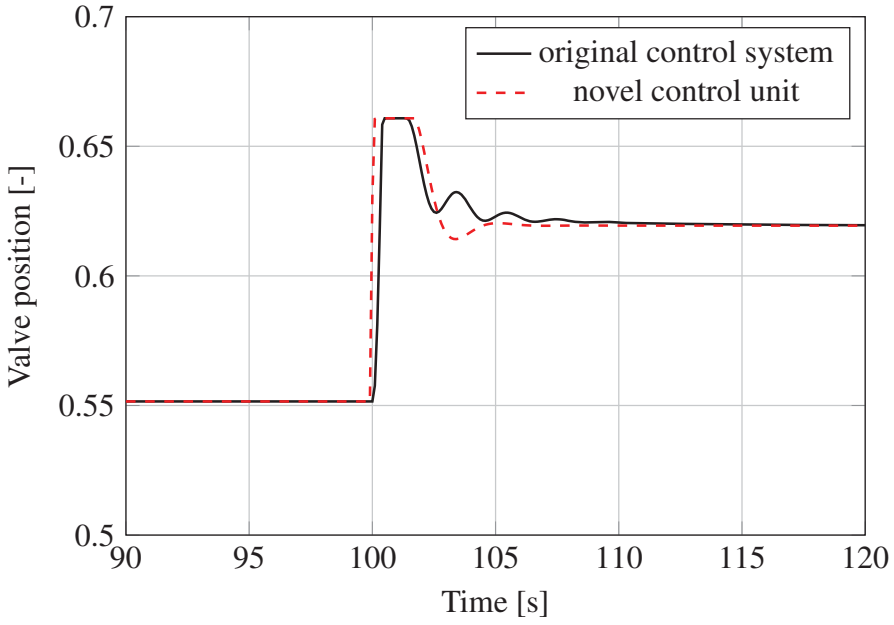

(a)

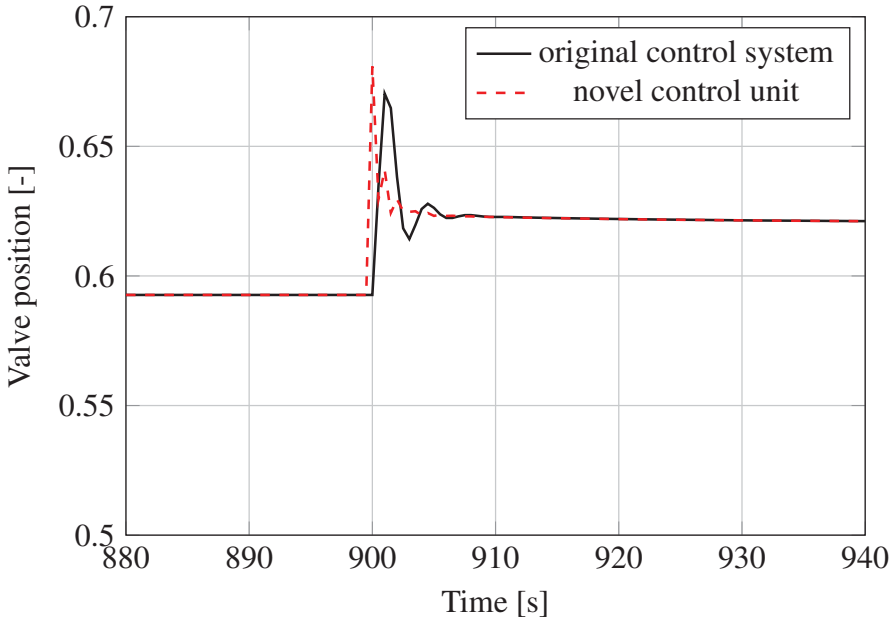

(b)

Figure 5.4: Dynamics of the valve position for the controller of the gas turbine manufacturer and the MPC unit. 5.4(a) Valve position as a function of time for a step in the load set-point of 4 MW. The power system consists of one gas turbine. 5.4(b) Valve position as a function of time for a step in the load set-point of 2 MW. The power system consists of one gas turbine and the ORC turbogenerator.

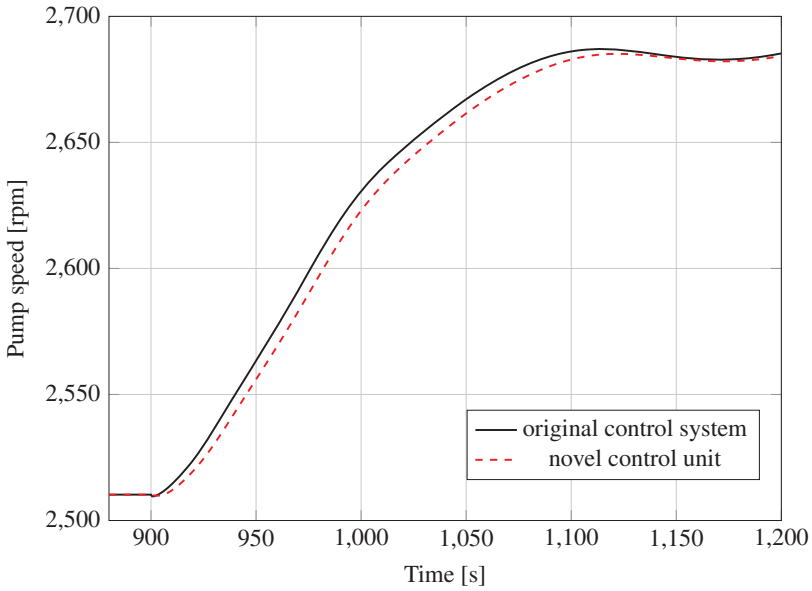

Figure 5.5: Dynamics of the pump speed for the proportional-integral controller and the MPC unit. The time is limited to 1200 s. The load set-point varies of 2 MW.

The plot reports the working points of the plant with three strategies: i) fixed design-point turbine inlet temperature (269.0 °C), ii) peak efficiency, and iii) constant design-point exhaust gas temperature (163.8 °C). Note that the set-points of the first and third variables are retrieved from the design-point configuration. The second control mode enables to operate at higher thermal efficiency: +0.6 % compared to fixed turbine inlet temperature and +0.2 % with constant exhaust gas temperature. Figure 5.7 provides the performance gains in terms of yearly fuel savings and net present value. The graph forecasts a possible reduction in the consumption of natural gas in the range of 2 - 3 %. The corresponding decrease in CO_2 emission is around 1.1 $t \cdot d^{-1}$. The proposed schedule can also increase the net present value over 20 years by more than 10 %.

A real-time update of the internal models of the MPC is presently beyond the capabilities of the present work. Adaptation and learning techniques are necessary to preserve the chemical integrity of cyclopentane and to identify the point of highest efficiency. Figure 5.8 demonstrates how the running point delivering the best performance shifts, when the overall heat transfer resistance of the once-though boiler increases by 20 %. This event, caused by fouling inside the tube rows, would induce the steady-state optimizer to deliver wrong optimal configurations. The real-time updating of the plant model could allow to determine the optimal pump speed and the correct set-point for the degree of superheating.

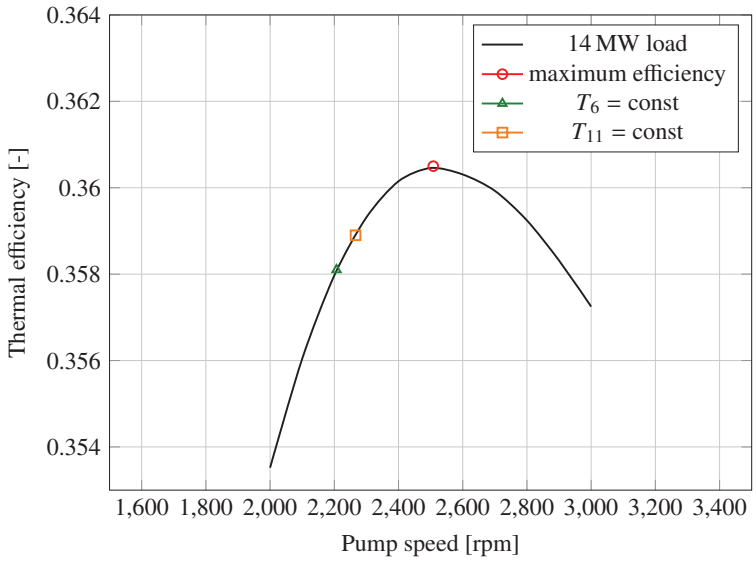

Figure 5.6: Thermal efficiency versus pump speed and working points of each control mode for a load of 14 MW.

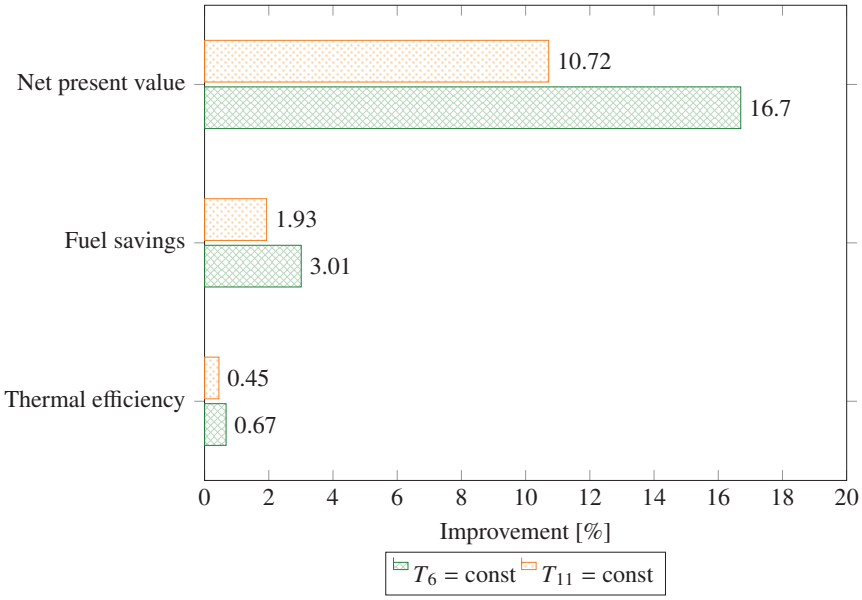

Figure 5.7: Improvements in terms of yearly performance, fuel savings and net present value obtained tracking the peak performance of the plant.

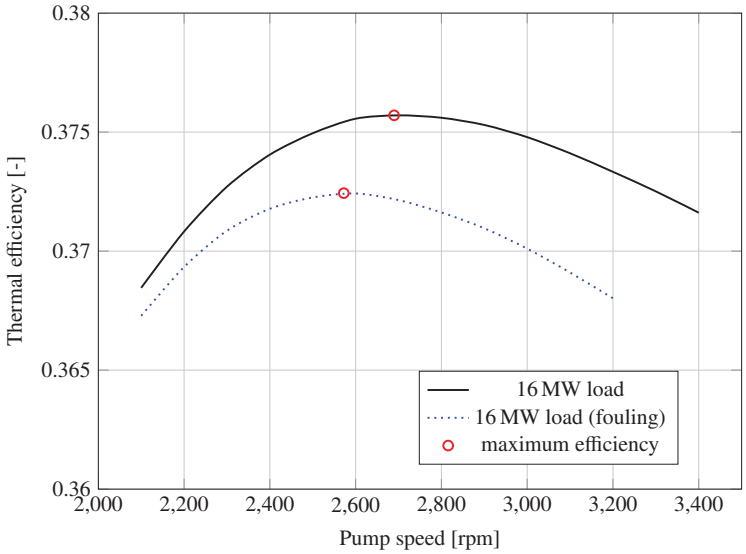

Figure 5.8: Effect of fouling of the once-though boiler on the thermal efficiency of the plant. The points of peak performance for a load set-point of 16 MW are reported before (solid line) and after (dotted line) fouling.

5.3.2 Stability of the control action

The on-line calibration of the models is fundamental to fully exploit the capabilities of the model predictive control. Fouling of the OTB cannot be anticipated by the internal models. Therefore, this event numerically perturbs the optimization problem solved by the MPC. Figure 5.9 shows the dynamics of the combined cycle unit in normal operation and with a 20 % deterioration of the overall heat transfer coefficient of the OTB. Note that the internal model of the steady-state optimizer is updated to identify the optimal thermal efficiency.

Figures 5.9(a) and 5.9(b) show the frequency of the grid and the corresponding valve position as a function of time. Fouling does neither induce control instabilities nor affect the valve dynamics. This statement applies also for the optimal degree of superheating and the rotational speed of the plant, see Figures 5.9(c) and 5.9(d). The shaft powers of the gas turbine and the ORC expander are shown in Figures 5.9(e) and 5.9(f). The plots indicate that fouling induces a reduction of around 5 % in the share supplied by the bottoming cycle unit. The results demonstrate that significant disturbances do not affect the stability of the control actions. A real-time update of the MPC models is thus not mandatory. However, the implementation of adaptation and learning techniques is recommendable to maximize the performances of the MPC unit.

The internal models of the MPC unit are built with no correspondence between the

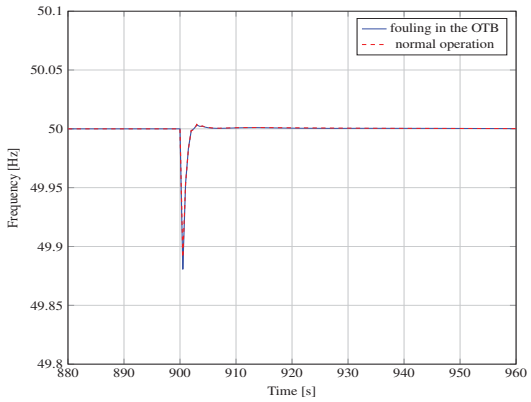

(a) Network frequency

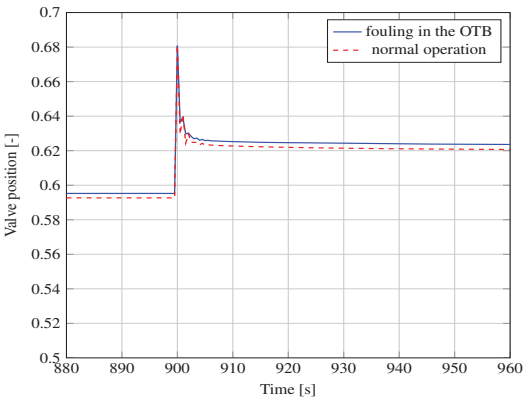

(b) Valve position

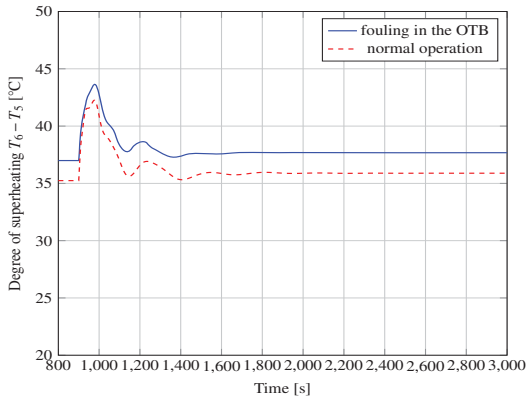

(c) Degree of superheating

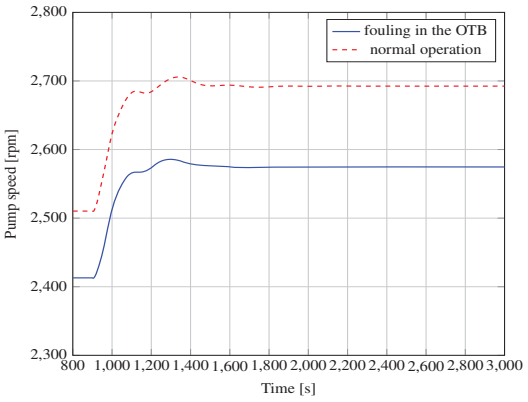

(d) Pump rotational speed

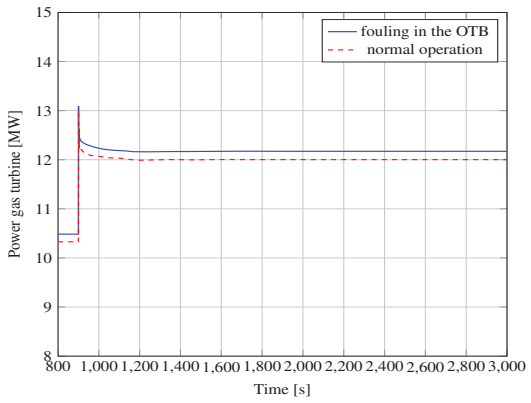

(e) Shaft power of the gas turbine

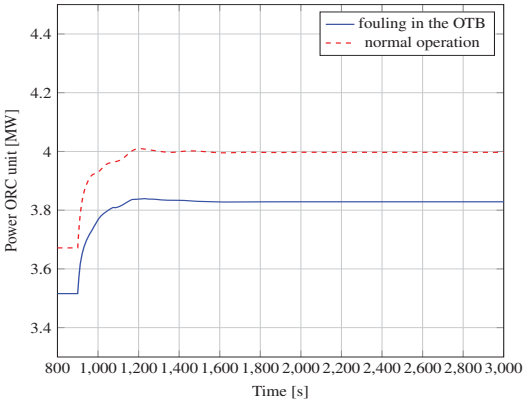

(f) Shaft power of the organic Rankine cycle unit

Figure 5.9: Dynamics of the combined cycle unit (gas turbine and ORC module) in normal operation and after a 20 % deterioration of the overall heat transfer coefficient induced by fouling in the tubes of the once-through boiler. The plant operates in both cases at the optimal thermal efficiency.

pump speed and the frequency, as well as between the valve position and the ORC output variables. As demonstrated in the previous section, the influence of the pump speed on the grid stability is marginal. Conversely, the process variables of the ORC module strongly depend on the thermodynamic conditions of the exhaust stream. The implementation of the additional transfer functions introduce instabilities in the control actions. Briefly described, the MPC unit may attempt to regain the frequency set-point using also the pump speed. Additionally, the fuel valve could be incorrectly controlled to track the degree of superheating. This could lead to unacceptable frequency offsets and fluctuations. The two control problems are thus kept distinct. The valve regulates the frequency, while the maximum thermal efficiency is monitored (if feasible) through the pump speed.

Bibliography

[1] O. Bolland, M. Førde, and B. Hånde. Air bottoming cycle: use of gas turbine waste heat for power generation. *Journal of Engineering for Gas Turbines and Power*, 118:359–368, 1996.

[2] C. Bonacina, A. Cavallini, and L. Mattarolo. *Trasmissione del calore*. Cleup, Padova, Italy, 1992. ISBN: 9788871789200.

[3] F. Cataldo, R. Mastrullo, A. W. Mauro, and G. P. Vanoli. Fluid selection of organic Rankine cycle for low-temperature waste heat recovery based on thermal optimization. *Energy*, 72(0):159 – 167, 2014.

[4] P. Del Turco, A. Asti, A. Del Greco, A. Bacci, G. Landi, and G. Seghi. The ORegen waste heat recovery cycle: Reducing the CO_2 footprint by means of overall cycle efficiency improvement. In *Proceedings of ASME Turbo Expo 2011*, pages 547–556, Vancouver, Canada, June 2011.

[5] T. Erhart. Dynamic simulation of OR-cycles. In *Proceedings of International Symposium on Advanced Waste Heat Valorisation Technologies*, Kortrijk, Belgium, September 2012.

[6] M. Gaia and R. Bini. Method and turbine for expanding an organic operating fluid in a Rankine cycle, July 2013. WO Patent 2013108099 A2.

[7] D. M. Ginosar, L. M. Petkovic, and D. P. Guillen. Thermal stability of cyclopentane as an organic Rankine cycle working fluid. *Energy & Fuels*, 25(9):4138–4144, 2011.

[8] E. Macchi. Design criteria for turbines operating with fluids having a low speed of sound. *Von Karman Inst. for Fluid Dyn. Closed Cycle Gas Turbines*, 2:1–64, 1977.

[9] M. Pasetti, C. M. Invernizzi, and P. Iora. Thermal stability of working fluids for organic Rankine cycles: An improved survey method and experimental results for cyclopentane, isopentane and n-butane. *Applied Thermal Engineering*, 73(1):762 – 772, 2014.

[10] S. Quoilin, M. V. D. Broek, S. Declaye, P. Dewallef, and V. Lemort. Techno-economic survey of organic Rankine cycle (ORC) systems. *Renewable and Sustainable Energy Reviews*, 22:168–186, 2013.

[11] G. Shu, X. Li, H. Tian, X. Liang, H. Wei, and X. Wang. Alkanes as working fluids for high-temperature exhaust heat recovery of diesel engine using organic Rankine cycle. *Applied Energy*, 119:204–217, 2014.

[12] J. Wang, Z. Yan, M. Wang, S. Ma, and Y. Dai. Thermodynamic analysis and optimization of an (organic Rankine cycle) ORC using low grade heat source. *Energy*, 49:356–365, 2013.

[13] L. Wu, D. Thimsen, B. Clements, L. Zheng, and R. Pomalis. A hybrid Rankine cycle (HyRC) with ambient pressure combustion (APC). *Applied Thermal Engineering*, 73(1):482 – 497, 2014.

CHAPTER 6

Conclusions

This chapter reports the final conclusions of the research activities disclosed in this Ph.D. thesis. The relevant findings obtained with the design method and the control system introduced in Chapter 3 are first summarized. Hypotheses i) - v) are then addressed. Guidelines for the design of future and existing offshore installations are also given. Finally, the chapter provides some suggestions for improving the adopted methods. Furthermore, opportunities for future research in the field of energy sustainability of oil and gas platforms are outlined.

6.1 Concluding remarks

This study aims at designing advanced power systems to supply future and existing offshore oil and gas platforms. The author accomplishes this task elaborating novel methods to design alternative waste heat recovery units (e.g. Brayton and Rankine engines) and innovative control systems enhancing the dynamic flexibility of the plant.

Hypothesis i) - the optimal waste heat recovery technology

The results demonstrate that the organic Rankine engine gives the best performance. The working fluid is cyclopentane. The potential reduction of CO_2 emissions and pollutants is in the range of 10 - 15 %. The Pareto frontier of each plant technology has a design candidate maximizing the economic revenue of the investment. In this regard, the implementation of steam Rankine cycle units permits to achieve the highest net present value (3.7 M$). The largest share of the investment is due to the expander. The lightest modules (10 - 60 t) are projected using the ABC system. This technology benefits from the open-loop configuration and the extreme compactness of the primary heat exchanger. Therefore, Brayton engines are preferable for the retrofitting of existing offshore facilities with extended lifetime. The poor performances and the lower economic revenue discourage its implementation on future platforms. The steam and the organic Rankine cycle are competing technologies for new installations. The final decision tightly relates to the selection of the topping unit and to the design of the energy system on board. In platforms requiring a high fuel-flexibility, advantages in terms of system design and performance lean toward the use of organic Rankine cycle turbogenerators. On the other hand, engineering efforts are necessary to manufacture low-cost turbines and to minimize the weight and volume of the primary heat exchanger.

Hypothesis ii) - the best working fluid

Varying the working fluid in the ORC module enabled to further reduce the objective functions. After the pre-selection process based on thermal stability, availability, cost, hazard and environmental impact, five candidates were deemed eligible, i.e., benzene, cyclopentane, isohexane, isopentane and cyclohexane. Benzene and cyclopentane give the highest reduction of fuel consumption and emission (up to 15.0 %). Isopentane and isohexane present poor performances for a given core weight. Benzene and cyclopentane offer the highest return of investment. The cost of the expander has the largest influence on the initial expenses. Cyclopentane and isopentane present low volumetric flow ratios (10-30) and optimal size parameters (< 20 cm). These feature facilitate the turbine design. Benzene compensates the higher cost of the expander with a high thermodynamic performance. Conversely, cyclohexane and isohexane are infeasible from an economic perspective due to the low power outputs and the high investment cost.

Hypothesis iii) - the dynamics as design criterion

Transient simulations give the possibility to discard infeasible designs which do not satisfy the requirements of the electric grid. This innovative method was implemented interfacing the steady-state optimization tool with a dynamic simulator. The tool is capable of determining the plant dynamics during critical scenarios, e.g., the trip of

one gas turbine unit. The system response during transients becomes in this way one of the crucial design criteria. Low-weight ORC turbogenerators can lead to exceed the maximum frequency tolerance, i.e., 4 %. Heavier modules minimize the frequency fluctuations and response times. Low-weight units require the largest changes of the fuel valve opening for a given variation of load set-point. Heavier turbogenerators facilitate the frequency control by virtue of the higher available power. Light modules are also more prone to experience instabilities in process variables, e.g., the temperature at the inlet of the ORC expander. This phenomenon tightly relates to the low evaporation pressures (20 - 25 bar) of these units. This design feature leads the once-through boiler to operate with a large portion of the organic fluid in vapor-liquid equilibrium. Furthermore, the dynamic simulations identify the design candidates with an excessive risk of chemical decomposition of the working fluid. Cyclopentane deterioration is found in ORC units with high design-point temperatures (280 °C) at the inlet of the expander.

Hypothesis iv) - the new control system

This work demonstrates the possibility for the combined cycle unit (the gas turbine and the ORC unit) to operate at the optimal performance with high reliability. The developed regulator uses the model predictive control to adjust the position of the fuel valve and the rotational speed of the ORC pump. The first control action minimizes the frequency variations. The second manipulated variable locates the working point of the combined cycle unit at its maximum thermal efficiency. A steady-state optimizer determines the optimal system configuration and its feasibility with respect to constraints. The variation of the operational strategy prevents acid formation at the outlet of the once-through boiler and the decomposition of the working fluid. Results advise to operate the power system at the peak efficiency in a load range from 40 % up to nominal power. This schedule has the potential to reduce the fuel consumptions by 3 % and to increase the economic revenue by more than 10 %. Low-power activities should be performed at constant exhaust gas temperature to preserve the integrity of the once-through boiler. The tracking of the temperature at the inlet of the ORC expander is not required. This process variable is below the decomposition limit at any load conditions. However, this strategy may be adopted in case of aging of the plant components or cyclopentane itself. Findings also stress the necessity-opportunity to update the plant model using adaptation and learning techniques.

Hypothesis v) - improved dynamic flexibility

The real-time updating of the MPC models, although recommendable to optimize the control action, is not crucial. The regulator delivers smooth and well-dampened responses, even in the presence of large unmeasured disturbances, e.g., fouling of the once-through boiler. The controller offers large improvements in the dynamic flexibility of the plant compared to the feedback controller of the engine manufacturer. The

MPC unit reduces the frequency fluctuations in the range of 20 - 40 %. The rise time also decreases. This demonstrates the faster response of the MPC compared to the PI controller. The control trajectory of the pump speed is similar to that of a properly tuned feedback regulator. The gas turbine governs the dynamics of the bottoming unit. Therefore, model-based algorithms can marginally affect the transient response of the bottoming unit. Nevertheless, the MPC is more flexible than standard PI controllers. In fact, it allows to switch the operational strategy of the bottoming cycle unit and to handle constraints on control and process variables.

6.2 Future work

Design methods

The performance of Rankine and Brayton engines strongly depends on the expender efficiency. This statement is particularly emphasized at low power capacities (1 kW to 10 MW). The expander is less efficient in this power range. Moreover, it usually determines the investment cost of the system. The optimization approach proposed in this work should be complemented with simulation tools calculating the expander geometry and its performance at given cycle conditions. However, codes for turbine design typically adopt mean-line methods solving the balance equations for mass, energy, and momentum in one or more directions [4]. This numerical approach has a large computational effort compared to the algorithms used to size the heat transfer equipment. Maps relating the expander performance to geometric and thermodynamic variables, interpolated by intelligent techniques (e.g. artificial neural networks [1]), can significantly decrease the computational time. Initial results based on ongoing work at the Technical University of Denmark and Delft University of Technology (The Netherlands) are promising. Preliminary simulations have shown the strong influence of the expander design in the cycle optimization. The relevance of data collection from test rigs and operating plants is here stressed. It allows to validate the component models and to better quantify the uncertainties of the simulation tool. These steps will enable the development of computer programs for the design of energy conversion systems based on the virtual prototyping concept [7]. This technique could avoid constructing expensive physical mock-ups to test different product designs and to simulate real-time operating conditions. It could cut the production costs, optimize the product design and identify equipment malfunctions.

Control algorithms

The regulator proposed in this thesis uses the linear model predictive control and a steady-state optimizer. Its task is to identify the optimal working point of the plant and its feasibility with respect to operational constraints. However, the same objective could be pursued by adopting non-linear model predictive algorithms, see Camacho and Alba [2]. This implementation enables to track directly the maximum efficiency of the plant, e.g., by setting unreachable set-points based on the Carnot's theorem. Nonetheless, difficulties to solve the non-convex optimization problem lead to a significant increase of the computational time. This has limited the practicability of this approach to slow processes until now [2]. In this context, advances in modeling techniques, with particular focus on faster calculations of fluid physical properties, are necessary to exploit the potentials of the non-linear model predictive control.

The control system requires the use of adaptation and learning techniques to operate at the peak efficiency and to optimize the control actions. Operational data should be used to update the internal models, especially of the steady-state optimizer. This requires to identify the component experiencing the malfunction (e.g. caused by aging) and to tune the plant model. This step could be accomplished using methods based on exergetic and thermoeconomic indicators, see, for instance, Lazzaretto and Toffolo [8], Lazzaretto et al. [9].

Towards zero-emissions offshore platforms

As regarding the sustainability of oil and gas power systems (see also Section 1.1), industry and academia are currently focusing on three separate directions: i) electrification from onshore power plants [3], ii) carbon capture and storage technologies [6], and iii) implementation of waste heat recovery units [10]. A possible integration of renewable energies (wind power) is also currently under investigation, see He et al. [5]. Unification of these research efforts could allow to project a futuristic platform. The facility should exchange power with the onshore grid, integrate wind farms backed-up with advanced power plants, and sequestrate the carbon dioxide generated during shortage of wind power. Moreover, the extreme need for reliability and high quality of the power supply obligates to improve both control schemes and design methods. This proof-of-concept requires to construct a virtual model of the entire facility using multi-objective optimization algorithms. Experimental work on gas turbines and ORC turbogenerators, possibly operating in supercritical conditions, should also be performed. This allows to evaluate the performance of the developed regulator. Furthermore, operational challenges in the presence of wind power losses could be addressed.

Bibliography

[1] C. M. Bishop. *Neural networks for pattern recognition*. Clarendon press Oxford, Oxford, United of Kingdom, 1995. ISBN: 9780198538646.

[2] E. F. Camacho and C. B. Alba. *Model predictive control*. Springer, London, Great Britain, 2013. ISBN: 9781852336943.

[3] I. M. de Alegría, J. L. Martín, I. Kortabarria, J. Andreu, and P. I. Ereño. Transmission alternatives for offshore electrical power. *Renewable and Sustainable Energy Reviews*, 13(5):1027–1038, 2009.

[4] S. Dixon and C. Hall. *Fluid Mechanics and Thermodynamics of Turbomachinery (Seventh Edition)*. Butterworth-Heinemann, Boston, Massachusetts, 2014. ISBN: 9780124159549.

[5] W. He, G. Jacobsen, T. Anderson, F. Olsen, T. D. Hanson, M. Korpås, T. Toftevaag, J. Eek, K. Uhlen, and E. Johansson. The potential of integrating wind power with offshore oil and gas platforms. *Wind Engineering*, 34(2):125–138, 2010.

[6] J. Hetland, H. M. Kvamsdal, G. Haugen, F. Major, V. Kårstad, and G. Tjellander. Integrating a full carbon capture scheme onto a 450MW_e NGCC electric power generation hub for offshore operations: Presenting the Sevan GTW concept. *Applied Energy*, 86(11):2298–2307, 2009.

[7] T. Huang, C. Kong, H. Guo, A. Baldwin, and H. Li. A virtual prototyping system for simulating construction processes. *Automation in Construction*, 16(5):576–585, 2007.

[8] A. Lazzaretto and A. Toffolo. A critical review of the thermoeconomic diagnosis methodologies for the location of causes of malfunctions in energy systems. *Journal of Energy Resources Technology*, 128(4):335–342, 2006.

[9] A. Lazzaretto, A. Toffolo, M. Reini, R. Taccani, A. Zaleta-Aguilar, V. Rangel-Hernandez, and V. Verda. Four approaches compared on the {TADEUS} (thermoeconomic approach to the diagnosis of energy utility systems) test case. *Energy*, 31(10–11):1586 – 1613, 2006.

[10] L. O. Nord and O. Bolland. Steam bottoming cycles offshore - Challenges and possibilities. *Journal of Power Technologies*, 92(3):201–207, 2012.

Appendix A

Steady-state correlations

This appendix contains the models used for the steady-state multi-objective optimization implemented in the DYNDES tool. The correlations used to evaluate the heat transfer coefficients and the pressure drops of the heat transfer equipment are given. Subsequently, the steady-state equations used to derive the part-load characteristics of the bottoming cycle units are reported. The appendix ends presenting the mathematical expressions used to estimate the purchased-equipment cost of the plant components.

A.1 Heat transfer and pressure drops

The correlations for the heat transfer coefficient and pressure drops on the gas side and in single-phase flow at hand read

- Gas flow outside finned tubes (Verein Deutscher Ingenieure [19] and Haaf [6])

$$Nu = 0.22\, Re^{0.6} Pr^{1/3} (A/A_t)^{-0.15}\,, \tag{A.1}$$

$$\Delta p = 2.5\, N_{\mathrm{tp}}\, Re^{-1/4}\, (P_{\mathrm{l}}/d)^{0.4} \rho u^2/2\,, \tag{A.2}$$

where A_{t} is the outside surface area of the tube considering fins, P_{l} is the longitudinal pitch, N_{tp} is the number of tube passes, ρ is the fluid density, and u is the fluid velocity. The variables Nu, Pr and Re are the Nusselt number, the Prandtl number and the Reynolds number.

- Single-phase flow (Gnielinski [5] and Coulson et al. [2])

$$\begin{cases} Nu = \frac{(\xi/8)(Re-1000)Pr}{1+12.7\sqrt{(\xi/8)}\,(Pr^{2/3}-1)} \left[1+\left(\frac{d}{l}\right)^{2/3}\right], \\ \xi = 1.84 \log_{10} Re - 1.64\,, \end{cases} \tag{A.3}$$

$$\Delta p = N_{\mathrm{tp}} \left(8\,\xi\,\frac{l}{d} + 2.5\right) \rho u^2/2\,, \tag{A.4}$$

where ξ is the friction factor.

Evaporation inside tubes is modeled implementing the equations reported in Shah [16] for the heat transfer coefficient, and in Friedel [3] and in Rouhani and Axelsson [14] for the pressure drops. As regarding condensation outside horizontal tubes, the heat transfer coefficient h_c is expressed in accordance to Kern [10] as

$$h_c = 0.95\, \lambda_{\mathrm{l}}\, [9.81 \rho_{\mathrm{l}}\, (\rho_{\mathrm{l}} - \rho_{\mathrm{v}})/(\mu_{\mathrm{l}}\, \Gamma_{\mathrm{h}})]^{1/3} N_{\mathrm{r}}^{-1/6}\,, \tag{A.5}$$

where N_{r} is the average number of tubes in a vertical tube row, Γ_{h} is the tube loading, λ is the fluid thermal conductivity, and μ is the fluid viscosity. The subscripts "l" and "v" refer to the saturated liquid and saturated vapor conditions. As suggested by Kern [10], the pressure drops are evaluated using the method for single-phase flow (see Equation A.4). A factor of 50 % is applied to allow for the change in vapor velocity.

The Nusselt number on the shell side of the recuperator equipped with finned tubes can be written as (see Coulson et al. [2])

$$Nu = 0.134\, Re^{0.681} Pr^{1/3} ((F_\mathrm{p} - F_\mathrm{t})/F_\mathrm{h})^{0.2} (F_\mathrm{p}/F_\mathrm{t})^{0.1134} , \tag{A.6}$$

where F_p is the fin pitch, F_t is the fin thickness, and F_h is the fin height. As regarding the pressure drops calculation outside the finned tubes, Equation A.2 is adopted.

The heat transfer coefficient and the pressure drops on each side of the finned-plate heat exchanger (see Figures 3.4(a) and 3.4(b)) are expressed as follows (see Manglik and Bergles [13])

$$h = j\, G\, c_\mathrm{p}\, Pr^{-2/3} , \tag{A.7}$$

$$\Delta p = 2\, (l/d)\, f\, G^2/\rho . \tag{A.8}$$

In Equation A.7, c_p is the isobaric specific heat capacity of the working fluid, and G is the mass flow velocity. The detailed equations relating the Colburn factor j and the Fanning factor f to the FPHE geometry are obtained from Manglik and Bergles [13].

A.2 Part-load

The steady-state equations used to assess the part-load performance of the components constituting the three bottoming cycle units are here listed.

- Steam and air turbines (Stodola [17] and Schobeiri [15])

$$C_\mathrm{T} = \frac{\dot{m}\sqrt{T_\mathrm{in}}}{\sqrt{{p_\mathrm{in}}^2 - {p_\mathrm{out}}^2}} , \tag{A.9}$$

$$\eta_\mathrm{is,t} = \eta_\mathrm{is,t,des} \frac{N}{N_\mathrm{des}} \sqrt{\frac{\Delta h_\mathrm{is,des}}{\Delta h_\mathrm{is}}} \left(2 - \frac{N}{N_\mathrm{des}} \sqrt{\frac{\Delta h_\mathrm{is,des}}{\Delta h_\mathrm{is}}} \right) . \tag{A.10}$$

In Equation A.9, C_T is the turbine constant, $\dot{m}$ is the mass flow rate, T_{in} is turbine inlet temperature, p_{in} and p_{out} are the inlet and outlet pressures. In Equation A.10, the isentropic efficiency $\eta_{is,t}$ is given as a function of the rotational speed N in rpm and the isentropic enthalpy drop Δh_{is}. The subscript "des" refers to the variable calculated at design-point.

- Electric generators (Haglind and Elmegaard [7])

$$\eta_{el} = \frac{Load\ \eta_{el,des}}{Load\ \eta_{el,des} + (1 - \eta_{el,des})\left[(1 - F_{cu}) + F_{cu}\ Load^{2}\right]} , \tag{A.11}$$

where η_{el} is the electric efficiency of the generator, Load is the mechanical power input in per unit, and F_{cu} the copper loss fraction.

- Heat exchangers (Incropera et al. [9])

$$h = h_{des}\left(\frac{\dot{m}}{\dot{m}_{des}}\right)^{\gamma} , \tag{A.12}$$

$$\Delta p = \Delta p_{des}\left(\frac{\dot{V}}{\dot{V}_{des}}\right)^{2} . \tag{A.13}$$

The exponent γ is taken equal to 0.8 or 0.6 depending on the fluid location (inside or outside the tube banks). In Equation A.13, the variables $\dot{V}$ and Δp are the volumetric flow rate and the pressure drops inside (outside) the tubes.

- Pumps (Veres [20])

$$\eta_{p} = \eta_{p,des}\left(0.86387 + 0.3096F - 0.14086F^{2} - 0.029265F^{3}\right) , \tag{A.14}$$

$$F = \frac{\dot{V}/N}{\dot{V}_{\text{des}}/N_{\text{des}}} \,, \tag{A.15}$$

where η_{p} is the pump hydraulic efficiency.

A.3 Purchased-equipment cost

The purchased-equipment costs of the air compressor PEC_{AC} and air turbines PEC_{AT} are calculated as (see Valero et al. [18])

$$PEC_{\text{AC}} = 39.5\, \dot{m}_{\text{a}}\, \frac{r_{\text{c}}\, log(r_{\text{c}})}{0.9 - \eta_{\text{is,c}}} \,, \tag{A.16}$$

$$PEC_{\text{AT}} = 266.3\, \dot{m}_{\text{a}}\, \frac{log(r_{\text{e}})(1 + exp(0.036\, T_{\text{in}} - 54.4)}{0.92 - \eta_{\text{is,t}}} \,, \tag{A.17}$$

where $\dot{m}_{\text{a}}$ and r_{e} are the air mass flow rate and the expansion ratio. The variable $\eta_{\text{is,c}}$ is the isentropic efficiency of the compressor. Equation A.17 applies also for the power air turbine.

The prices of the pumps PEC_{p} serving the SRC and the ORC power units and the cost of the electric generators PEC_{gen} are computed as (see Lozano et al. [12] and Lian et al. [11])

$$PEC_{\text{p}} = 378 \left[1 + \left(\frac{1 - 0.808}{1 - \eta_{\text{p}}}\right)^3\right] \dot{P}_{\text{p}}^{0.71} \,, \tag{A.18}$$

$$PEC_{\text{gen}} = 60\, \dot{P}_{\text{gen}}^{0.95} \,, \tag{A.19}$$

where $\dot{P}_{\text{p}}$ and $\dot{P}_{\text{gen}}$ are the pump power and the electric power produced by the generator. The purchased-equipment cost of the steam turbine is set as a function of the mechanical power output $\dot{P}_{\text{t}}$, in accordance with Lozano et al. [12]. Conversely, the

cost of the ORC expander depends on the number of stages n and the size parameter $\sqrt{\dot{V}_7}/\Delta h_{\mathrm{is}}^{1/4}$ of the last stage, see Astolfi et al. [1].

$$PEC_{\mathrm{t,SRC}} = 3000 \left[1 + 5\, exp\left(\frac{T_{\mathrm{in}} - 866}{10.42}\right)\right] \left[1 + \left(\frac{1 - 0.953}{1 - \eta_{\mathrm{is,t}}}\right)^3\right] \dot{P}_{\mathrm{t}}^{0.7} \,, \tag{A.20}$$

$$PEC_{\mathrm{t,ORC}} = 1600 \left(\frac{n}{2}\right)^{0.5} \left(\frac{\sqrt{\dot{V}_7}/\Delta h_{\mathrm{is}}^{1/4}}{0.18}\right)^{1.1} \,. \tag{A.21}$$

In Equation A.21, a conversion factor of 1.3 euro-to-dollar is applied. The volumetric flow ratios and enthalpy drops of the ORC turbine are around 30 and $160\,\mathrm{kJ \cdot kg^{-1}}$, respectively. The expander is thus a single-stage axial turbine. For the once-through boiler, the shell-and-tube heat exchangers and the finned-plate heat exchanger, the cost PEC is related to the heat transfer area using the following equations (see Valero et al. [18], Hall et al. [8] and Genceli [4], respectively)

$$PEC_{\mathrm{OTB}} = 3650 \left[\left(\frac{\dot{q}_{\mathrm{sup}}}{\Delta T_{\mathrm{lm,sup}}}\right)^{0.8} + \left(\frac{\dot{q}_{\mathrm{eva}}}{\Delta T_{\mathrm{lm,eva}}}\right)^{0.8} + \left(\frac{\dot{q}_{\mathrm{eco}}}{\Delta T_{\mathrm{lm,eco}}}\right)^{0.8}\right] + 11820\, \dot{m} + 658\, \dot{m}_{\mathrm{exh}}^{1.2} \,, \tag{A.22}$$

$$PEC_{\mathrm{sh}} = 30800 + 890\, A_{\mathrm{sh}}^{0.81} \,, \tag{A.23}$$

$$PEC_{\mathrm{FPHE}} = 187 + 25\, A_{\mathrm{FPHE}} \,, \tag{A.24}$$

where $\dot{q}_{\mathrm{eva}}$ and $\Delta T_{\mathrm{lm,eva}}$ are the heat rate and the logarithmic mean temperature difference limited to the vapor-liquid region. The variables $\dot{q}_{\mathrm{eco}}$ and $\Delta T_{\mathrm{lm,eco}}$ refer to the liquid-phase zone. Note that, compared to the formula proposed by Valero et al. [18], the terms $\dot{q}_{\mathrm{sup}}$ and $\Delta T_{\mathrm{lm,sup}}$ are added to account for the cost of the superheating section. The subscripts "OTB", "sh" and "FPHE" stand for the once-through boiler, the shell-and-tube heat exchanger and the finned-plate heat exchanger. The variables $\dot{m}_{\mathrm{exh}}$ and $\dot{m}$ represent the mass flow rate of the exhaust gases and working fluid.

Bibliography

[1] M. Astolfi, M. C. Romano, P. Bombarda, and E. Macchi. Binary ORC (Organic Rankine Cycles) power plants for the exploitation of medium–low temperature geothermal sources–Part B: Techno-economic optimization. *Energy*, 66(0):435–446, 2014.

[2] J. Coulson, J. Richardson, and J. Backhurst. *Coulson and Richardson's Chemical Engineering*. Chemical engineering. Butterworth-Heinemann, Oxford, Great Britain, 1999. ISBN: 9780750644440.

[3] L. Friedel. Pressure drop during gas/vapor-liquid flow in pipes. *International Chemical Engineering*, 20(3):352–367, 1980.

[4] O. Genceli. *Heat exchangers*. Birsen Book Company, Turkey, 1999. ISBN: 9789755112183.

[5] V. Gnielinski. On heat transfer in tubes. *International Journal of Heat and Mass Transfer*, 63(0):134 – 140, 2013.

[6] S. Haaf. *Wärmeübertragung in Luftkühlern*. Springer Verlag, Berlin, Germany, 1988. ISBN: 9783540154778.

[7] F. Haglind and B. Elmegaard. Methodologies for predicting the part-load performance of aero-derivative gas turbines. *Energy*, 34(10):1484 – 1492, 2009.

[8] S. Hall, S. Ahmad, and R. Smith. Capital cost targets for heat exchanger networks comprising mixed materials of construction, pressure ratings and exchanger types. *Computers & chemical engineering*, 14(3):319–335, 1990.

[9] F. P. Incropera, D. P. DeWitt, T. L. Bergman, and A. S. Lavine. *Fundamentals of Heat and Mass Transfer*. John Wiley & Sons, Inc., Jefferson City, Missouri, 6 edition, 2007. ISBN: 9780470501979.

[10] D. Q. Kern. *Process heat transfer*. McGraw-Hill, New York City, New York, 1950. ISBN: 9780070341906.

[11] Z. Lian, K. Chua, and S. Chou. A thermoeconomic analysis of biomass energy for trigeneration. *Applied Energy*, 87(1):84–95, 2010.

[12] M.-A. Lozano, A. Valero, and L. Serra. Theory of exergetic cost and thermoeconomic optimization. In *Proceedings of the International Symposium ENSEC*, pages 339 – 350, Cracow, Poland, July 1993.

[13] R. M. Manglik and A. E. Bergles. Heat transfer and pressure drop correlations for the rectangular offset strip fin compact heat exchanger. *Experimental Thermal and Fluid Science*, 10(2):171–180, 1995.

[14] S. Z. Rouhani and E. Axelsson. Calculation of void volume fraction in the subcooled and quality boiling regions. *International Journal of Heat and Mass Transfer*, 13(2):383–393, 1970.

[15] M. Schobeiri. *Turbomachinery flow physics and dynamic performance*. Springer Berlin, Berlin, Germany, 2005. ISBN: 9783540223689.

[16] M. Shah. Chart correlation for saturated boiling heat transfer: equations and further study. *ASHRAE Transaction*, 88(1):185–196, 1982.

[17] A. Stodola. *Dampf- und Gasturbinen: Mit einem Anhang über die Aussichten der Wärmekraftmaschinen*. Springer Berlin, Berlin, Germany, 1922. ISBN: 7352997563.

[18] A. Valero, M. A. Lozano, L. Serra, G. Tsatsaronis, J. Pisa, C. Frangopoulos, and M. R. von Spakovsky. CGAM problem: definition and conventional solution. *Energy*, 19(3):279–286, 1994.

[19] Verein Deutscher Ingenieure . *VDI-Wärmeatlas: Berechnungsblätter für den Wärmeübergang*. Springer-Verlag, Berlin, Germany, 1953. ISBN: 9783540412014.

[20] J. P. Veres. Centrifugal and Axial Pump Design and Off-Design Performance Prediction. Technical report, NASA, Sunnyvale, United States of America, 1994. Technical Memorandum 106745.

Appendix B

Compressor and turbine models

This appendix describes the methods used to predict the part-load characteristics of the axial compressors and turbines. These methods are implemented to model the dynamics of the gas turbines installed on the Draugen oil and gas platform, see Section 2. The different approaches are compared using the off-design curves provided by the engine manufacturer.

B.1 The compressor

B.1.1 The extrapolation method

Extrapolation methods employ multi-parametric polynomial curves fit with a certain number of coefficients to describe the maps. In axial compressors, a first curve relates the mass flow rate with the pressure ratio. The second equation gives the isentropic efficiency as a function of the mass flow rate or the pressure ratio. The accuracy of

this method strongly depends on the compressor map selected for the fitting procedure. The correlations proposed by Zhang and Cai [13] are used in this work.

The corrected mass flow rate $\dot{G}$ and speed $\dot{N}$ are defined based on the air mass flow rate, the rotational speed, the ambient temperature and the atmospheric pressure, see Equation B.1.

$$\begin{cases} \dot{G} = \frac{\dot{m}\sqrt{T_{\text{in}}}}{p_{\text{in}}} \\ \dot{N} = \frac{N}{\sqrt{T_{\text{in}}}} \end{cases} . \tag{B.1}$$

The equation relating the pressure ratio, the rotational speed and the mass flow rate at off-design can thus be expressed as

$$\frac{r_{\text{c,off}}}{r_{\text{c,des}}} = c_1 \left(\frac{\dot{G}_{\text{off}}}{\dot{G}_{\text{des}}} \right)^2 + c_2 \, \frac{\dot{G}_{\text{off}}}{\dot{G}_{\text{des}}} + c_3 \, , \tag{B.2}$$

where the subscripts "des" and "off" refer to the design-point and part-load conditions. The variables c_1, c_2 and c_3 depend on the rotational speed and are calculated as

$$c_1 = \frac{\dot{n}}{p(1 - m/\dot{n}) + \dot{n}(\dot{n} - m)^2} \, , \tag{B.3}$$

$$c_2 = \frac{p - 2m\dot{n}^2}{p(1 - m/\dot{n}) + \dot{n}(\dot{n} - m)^2} \, , \tag{B.4}$$

$$c_3 = \frac{-\left(pm\dot{n} - m^2\dot{n}^3\right)}{p(1 - m/\dot{n}) + \dot{n}(\dot{n} - m)^2} \, , \tag{B.5}$$

where $\dot{n} = \dot{N}_{\text{off}}/\dot{N}_{\text{des}}$ is the ratio between the corrected rotational speed at part-load and design-point. The values of the coefficients m and p are calculated through an optimization procedure. The deviation between the results given by Equation B.2 and the maps of the actual compressor is minimized. In absence of any information on the machine, reasonable figures for m and p are 1.06 and 0.36, respectively [13].

As regarding the compressor isentropic efficiency $\eta_{\mathrm{is,c}}$, the following equation is used

$$\frac{\eta_{\mathrm{is,c,off}}}{\eta_{\mathrm{is,c,des}}} = \left[1 - c_4 \left(1 - \dot{n}\right)^2\right]\left(\dot{n}/\dot{G}\right)\left(2 - \dot{n}/\dot{G}\right) , \tag{B.6}$$

where the coefficient c_4 is set equal to 0.3 [13].

B.1.2 The map scaling method

The map scaling procedure relays on the performance characteristics of an existing compressor. The curves are scaled so that the design-point is in line with a specific point in the map, the map scaling point. As reported in Kurzke [3], this procedure is accomplished through the following steps

1. selection of the design-point variables for the compressor that needs to be modeled, i.e., corrected mass flow rate $\dot{G}_{\mathrm{des}}$, corrected rotational speed $\dot{N}_{\mathrm{des}}$, pressure ratio $r_{\mathrm{c,des}}$ and isentropic efficiency $\eta_{\mathrm{is,c,des}}$,

2. find available characteristic maps of a compressor with similar design-point variables and configuration,

3. identification of the map scaling point through which the design-point selected in item 1 is matched,

4. calculation of the reference point variables (subscript "ref"), i.e., corrected mass flow rate $\dot{G}_{\mathrm{ref}}$, corrected rotational speed $\dot{N}_{\mathrm{ref}}$, pressure ratio $r_{\mathrm{c,ref}}$ and isentropic efficiency $\eta_{\mathrm{is,c,ref}}$,

5. computation of the map scaling factors f_{m}, f_{p}, f_{eta}, f_{sp} using the following set of equations

$$\begin{cases} f_{\mathrm{m}} = \dfrac{\dot{G}_{\mathrm{des}}}{\dot{G}_{\mathrm{ref}} f_{\mathrm{m,Re}}} \\ f_{\mathrm{p}} = \dfrac{r_{\mathrm{c,des}} - 1}{r_{\mathrm{c,ref}} - 1} \\ f_{\mathrm{eta}} = \dfrac{\eta_{\mathrm{is,c,des}}}{\eta_{\mathrm{is,c,ref}} f_{\mathrm{eta,Re}}} \\ f_{\mathrm{sp}} = \dfrac{\dot{N}_{\mathrm{des}}}{\dot{N}_{\mathrm{ref}}} \ , \end{cases} \tag{B.7}$$

where the variables $f_{\mathrm{m,Re}}$ and $f_{\mathrm{eta,Re}}$ account for Reynolds number effects. They are assumed equal to 0.995 and 0.99 [3] respectively,

6. the map scaling factors are applied to all numbers in the original map, thus enabling to align it with the design-point selected in item 1.

An appropriate selection of the reference point is essential for increasing the precision. For instance, locating the map scaling point in a region with poor performances allows the efficiency to increase towards part-load. Conversely, positioning the same point in the peak efficiency region of the map yields an efficiency decrease at any off-design operation [4].

B.1.3 The stage stacking analysis

The stage stacking analysis refers to a generic approach used to compute the overall pressure ratio and isentropic efficiency of a compressor using calculations of the pressure ratio and temperature rise of each stage. This work uses the stage stacking analysis introduced first by Stone [9] and by Howell and Calvert [2], extended by Cerri et al. [1] to model transonic and subsonic stages. This method will be referred as Cerri's stage stacking analysis (CSSA) throughout this appendix.

The CSSA uses generalized stage relationships between the normalized pressure coefficient $\bar{\psi} = \psi_{\mathrm{off}}/\psi_{\mathrm{des}}$, the normalized flow coefficient $\bar{\phi} = \phi_{\mathrm{off}}/\phi_{\mathrm{des}}$ and the normalized stage efficiency $\bar{\eta} = \eta_{\mathrm{off}}/\eta_{\mathrm{des}}$. These curves enable to perform the off-design analysis. The generalized relationship derived from experimental data over a wide range of compressor stages at hand reads (see Cerri et al. [1])

$$\bar{\psi} = \bar{\psi}_{\max} - \frac{(\bar{\psi}_{\max} - 1)\left[\bar{\phi}_{\max} + SF(\bar{\phi}_{\max} - 1) - \bar{\phi}\right]^2}{\left[\bar{\phi}_{\max} + SF(\bar{\phi}_{\max} - 1) - 1\right]^2} , \tag{B.8}$$

where the shaping factor SF ranges between -0.5 and 1. This parameter allows the representation of transonic and supersonic stages. The second empirical equation, proposed by Howell and Calvert [2], sets $\bar{\eta}$ as a function of $\eta_{\text{off}}/\eta_{\text{des}}$. It predicts the isentropic efficiency at off-design. The mathematical expression for the curve is divided into two terms in accordance with the following equation

$$\begin{cases} \bar{\eta} = 1 - \frac{1-\bar{\eta}_{\min}}{\left[1-(\bar{\psi}/\bar{\phi})_{\min}\right]^{3.5}} \left(1 - \bar{\psi}/\bar{\phi}\right)^{3.5} & \bar{\psi}/\bar{\phi} \in \left[(\bar{\psi}/\bar{\phi})_{\min}, 1\right] \\ \bar{\eta} = 1 - \frac{1-\bar{\eta}_{\max}}{\left[(\bar{\psi}/\bar{\phi})_{\max}-1\right]^2} \left(\bar{\psi}/\bar{\phi} - 1\right)^2 & \bar{\psi}/\bar{\phi} \in \left[1, (\bar{\psi}/\bar{\phi})_{\max}\right] . \end{cases} \tag{B.9}$$

The CSSA is fairly accurate in assessing the pressure ratio and mass flow rate, but poor in predicting the isentropic efficiency. This variable is peculiar for each compressor. The use of a single empirical curve does not guarantee the required level of accuracy [5]. For this reason, multi-dimensional methods based on computational fluid dynamics [6, 10, 12] have been developed to improve the model accuracy. The implementation of these methods is beyond the scope of this thesis. The analysis is thus limited to the application of the zero-dimensional approach outlined in Cerri et al. [1].

B.2 The turbine

The global turbine characteristic method introduced by Stodola [8] and Traupel [11] treats the turbine stage as a nozzle. This device is described accordingly with a set of algebraic equations. The most adopted formulation is the Stodola's law of the ellipse [8], which at hand reads

$$\dot{m}_{\text{off}} = \dot{m}_{\text{des}} \frac{p_{\text{in,off}}}{p_{\text{in,des}}} \left(\frac{T_{\text{in,des}}}{T_{\text{in,off}}}\right)^{1/2} \left[\frac{1 - (r_{\text{e,off}})^{\frac{n+1}{n}}}{1 - (r_{\text{e,des}})^{\frac{n+1}{n}}}\right]^{1/2} , \tag{B.10}$$

where n is the polytropic exponent. This variable is a function of the ratio κ between the isobaric and isochoric heat capacity and the turbine stage isentropic efficiency, see Equation B.11.

$$n = \frac{\kappa}{\kappa - \eta_{\mathrm{is,t}}(\kappa - 1)} \ . \tag{B.11}$$

The derivation of Equation B.10 can be found in Traupel [11]. It requires the following assumptions:

i) the polytropic exponent is constant for all flow conditions,

ii) the fluid is an ideal gas,

iii) the same average value of the wideness parameter [11] is valid for all flow conditions.

Note that expanders using mixtures of gases and steam can be modeled by Equation A.9 with the assumption that $\frac{n+1}{n} \approx 2$, valid if n ≈ 1.

As regarding the stage performance, the isentropic efficiency may be assumed constant in a rough preliminary off-design model. However, low mechanical powers deteriorate the efficiency owing to the increasing losses, thus requiring the introduction of a stage performance characteristic. As proposed by Schobeiri [7], the curve relating the non-dimensional efficiency to the velocity parameter $\bar{\nu} = \nu_{\mathrm{off}}/\nu_{\mathrm{des}}$ can be formulated using the following polynomial expression

$$\begin{cases} \bar{\eta} = \sum\limits_{i=1}^{m} a_{\mathrm{i}} \left(\frac{\nu_{\mathrm{off}}}{\nu_{\mathrm{des}}} \right)^{i} \\ \nu = \frac{N}{\sqrt{2\Delta h_{\mathrm{is}}}} \ . \end{cases} \tag{B.12}$$

The coefficients a_{i} can be determined by a fitting procedure. If no experimental data are available, a parabolic expression can be adopted, thus leading to the derivation of Equation A.10.

Bibliography

[1] G. Cerri, C. Salvini, R. Procacci, and F. Rispoli. Fouling and air bleed extracted flow influence on compressor performance. In *Proceedings of ASME Turbo Expo 1993*, Cincinnati, Ohio, May 1993.

[2] A. Howell and W. Calvert. A new stage stacking technique for axial-flow compressor performance prediction. *Journal of Engineering for Power*, 100:698–703, 1978.

[3] J. Kurzke. *GasTurb 10 User Manual*. Germany, January 2004.

[4] J. Kurzke. How to create a performance model of a gas turbine from a limited amount of information. In *Proceedings of ASME Turbo Expo 2005*, pages 145–153, Reno-Tahoe, Nevada, June 2005.

[5] F. Melino, M. Morini, A. Peretto, M. Pinelli, and P. Ruggero Spina. Compressor fouling modeling: relationship between computational roughness and gas turbine operation time. *Journal of Engineering for Gas Turbines and Power*, 134(5):1–8, 2012.

[6] V. Pachidis, P. Pilidis, I. Templalexis, and L. Marinai. An iterative method for blade profile loss model adaptation using streamline curvature. *Journal of Engineering for Gas Turbines and Power*, 130(1):1–8, 2008.

[7] M. Schobeiri. *Turbomachinery flow physics and dynamic performance*. Springer Berlin, Berlin, Germany, 2005. ISBN: 9783540223689.

[8] A. Stodola. *Dampf- und Gasturbinen: Mit einem Anhang über die Aussichten der Wärmekraftmaschinen*. Springer Berlin, Berlin, Germany, 1922. ISBN: 7352997563.

[9] A. Stone. Effects of stage characteristics and matching on axial-flow-compressor performance. *ASME*, 57(A-139):1–17, 1957.

[10] L. Templalexis, P. Pilidis, V. Pachidis, and P. Kotsiopoulos. Development of a two-dimensional streamline curvature code. *Journal of Turbomachinery*, 133(1): 1–7, 2011.

[11] W. Traupel. *Thermische Turbomaschinen. Band 1, 3. Auflage, 1977*. Springer-Verlag, Berlin, Germany, 1977. ISBN: 9783540079392.

[12] M. G. Turner, A. Merchant, and D. Bruna. A turbomachinery design tool for teaching design concepts for axial-flow fans, compressors, and turbines. *Journal of Turbomachinery*, 133(3):1–12, 2011.

[13] N. Zhang and R. Cai. Analytical solutions and typical characteristics of part-load performances of single shaft gas turbine and its cogeneration. *Energy Conversion and Management*, 43(9):1323–1337, 2002.

Appendix C

Gas turbine model validation

This appendix is an extension of Section 3.5.1, where the validation and verification of the gas turbine model are outlined. The curves of the manufacturer are compared with the three modeling approaches for the compressors, i.e., the map scaling technique, the Cerri's stage stacking analysis and the extrapolation method. Furthermore, the properties of the measuring instruments and data acquisition system are reported. This information characterizes the uncertainties in the operational data provided by the platform operator.

C.1 Steady-state verification

This section shows the results of the comparison between the three methods for predicting the part-load performance of the SGT-500 gas turbine. The map scaling technique, the Cerri's stage stacking analysis and the extrapolation approach are applied to model the compressors. The turbines use the Stodola's law of the ellipse with variable isentropic efficiency.

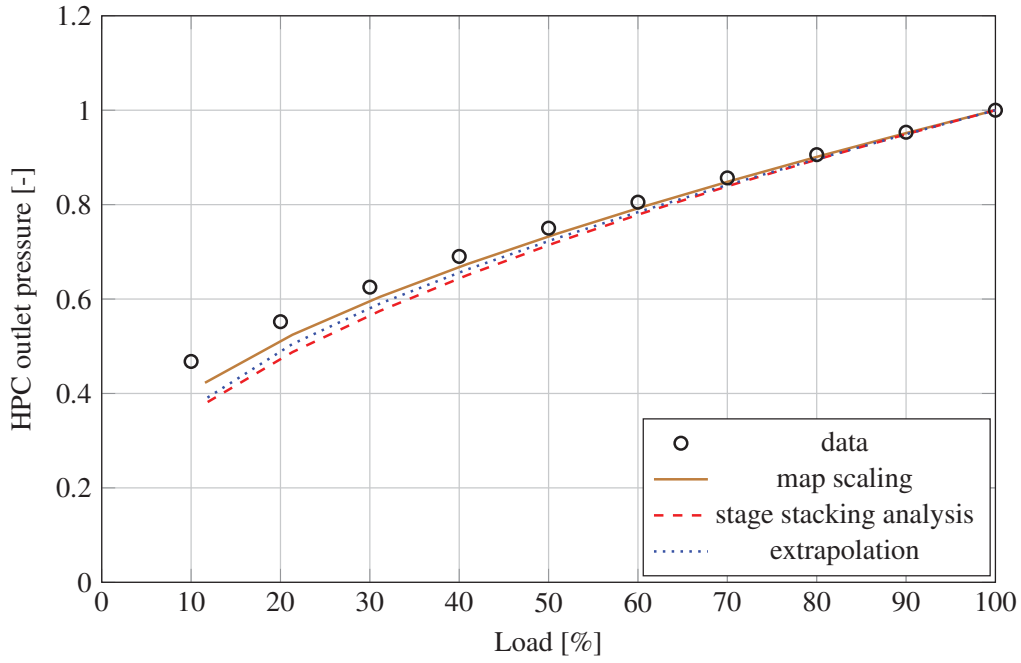

Figure C.1: High pressure compressor outlet pressure versus load. The dots represent the data provided by the engine manufacturer. The lines show the model results for the three methodologies. The variable in the ordinate is reported relative to the value at design-point.

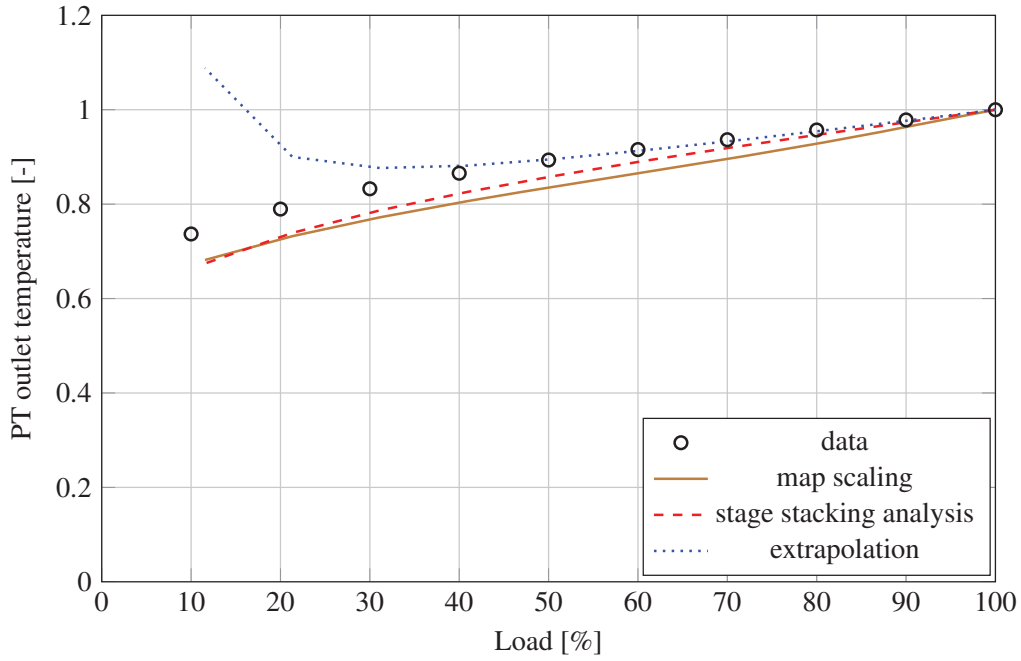

Figure C.2: Exhaust engine temperature versus load. The dots represent the data provided by the engine manufacturer. The lines show the model results for the three methodologies. The variable in the ordinate is reported relative to the value at design-point.

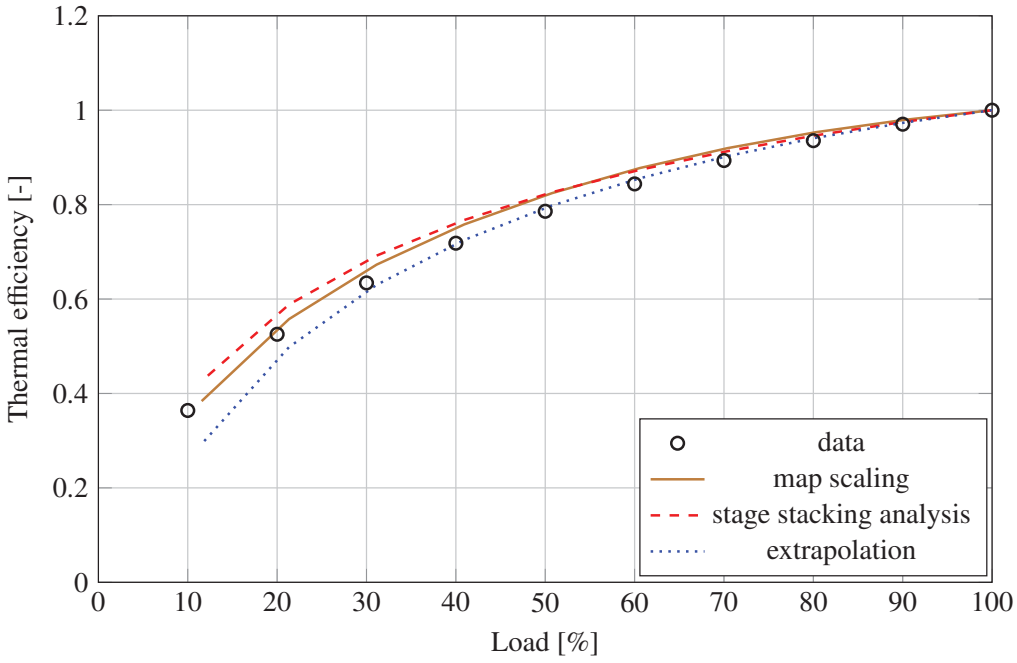

Figure C.3: Thermal efficiency versus load. The dots represent the data provided by the engine manufacturer. The lines show the model results for the three methodologies. The variable in the ordinate is reported relative to the value at design-point.

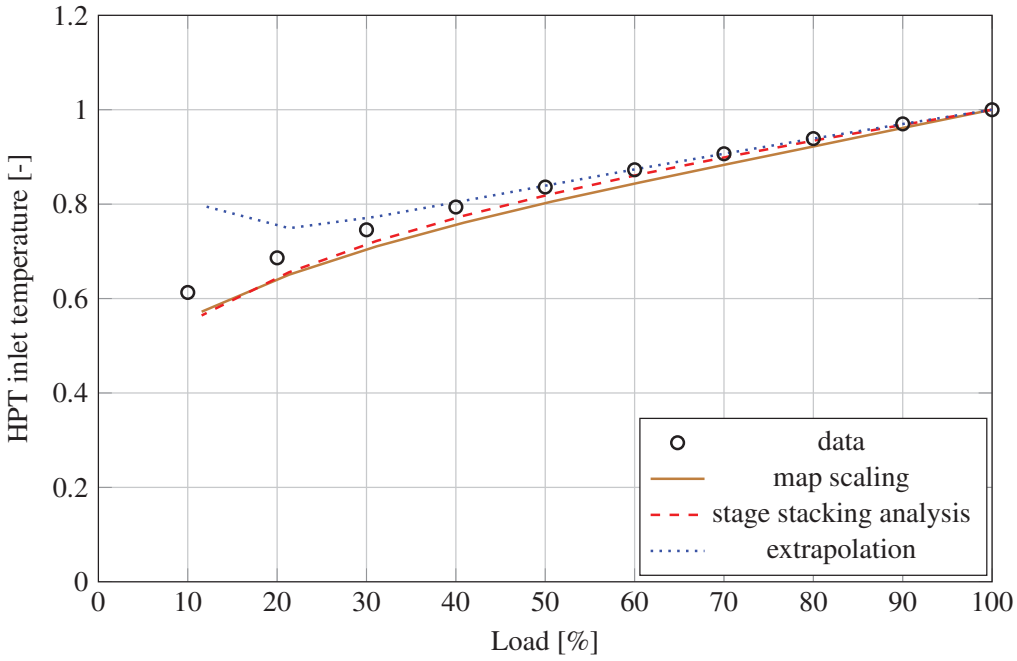

Figure C.4: High pressure turbine inlet temperature versus load. The dots represent the data provided by the engine manufacturer. The lines show the model results for the three methodologies. The variable in the ordinate is reported relative to the value at design-point.

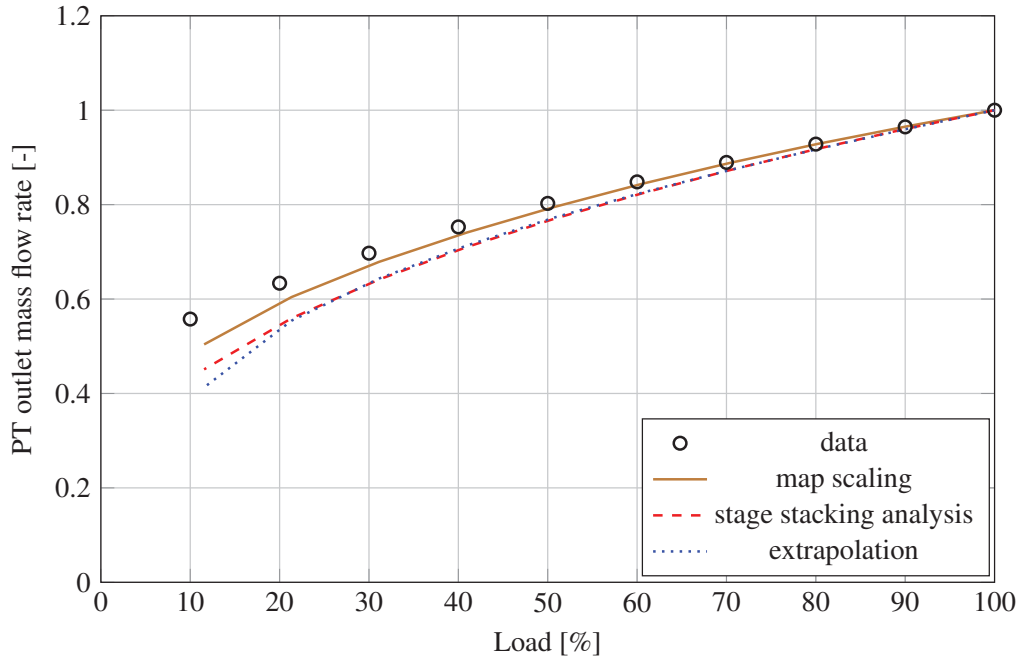

Figure C.5: Exhaust gas mass flow rate versus load. The dots represent the data provided by the engine manufacturer. The lines show the model results for the three methodologies. The variable in the ordinate is reported relative to the value at design-point.

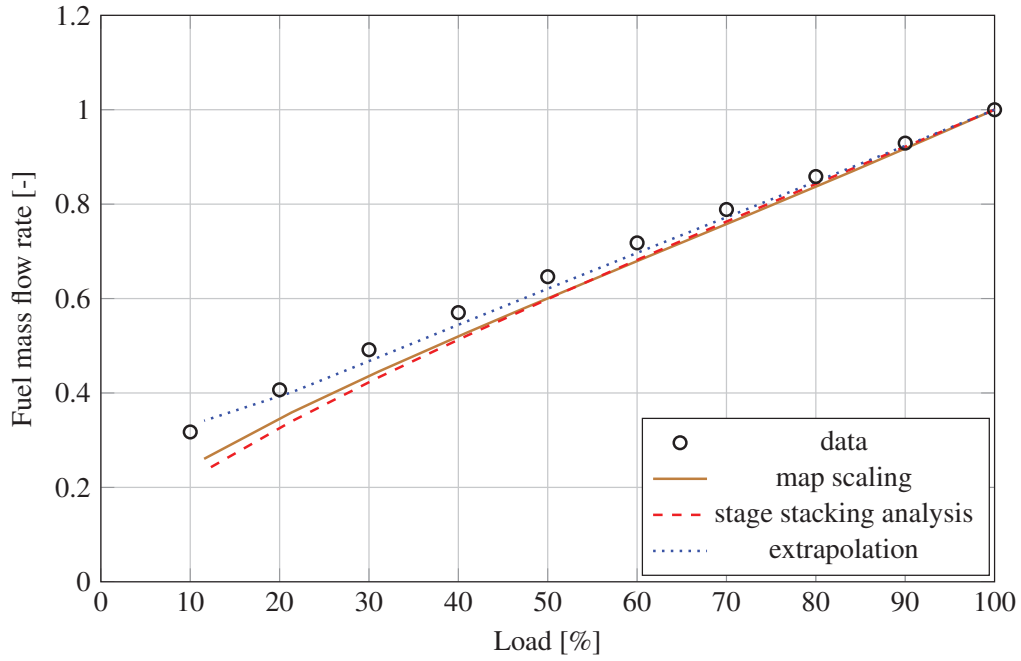

Figure C.6: Fuel consumption versus load. The dots represent the data provided by the engine manufacturer. The lines show the model results for the three methodologies. The variable in the ordinate is reported relative to the value at design-point.

C.2 The instrumentation and data acquisition system

The measurements for the validation of the dynamic model are accessible from a process information database (ProcessBook, OSIsoft©). Here the platform owner archives the operating data of the facility. The numerical values do not derive directly from the measuring equipment. They first undergo a standard procedure from the sensor data to the storage. The measured quantities are transferred to the process information server. Here they are post-processed before being saved in the database. The post-processing enables to reduce the size of the archived files.

A sampling time of 1 s is used for the dynamic model validation. All values are available with 15 digits in total. The post-processing of the measured data and the storage criteria of the database may affect quantitatively the model validation. The assumptions are the following

- averaging of the signals when multiple sensors (e.g. temperature sensors) are positioned in one location,
- updating of the values stored in the database only if the new value deviates from the last one by a certain threshold. If the value is within the limits, it is maintained constant,
- interpolation and/or constant values if the data are not saved at the time rate defined by the user, i.e., 1 s,
- the sampling time for extracting the values is 1 s, as defined by the user. However, no details about the data acquisition system are available. Further delays may be present between the time when the instrument measures the variables and the time when the value is stored in the database.

Table C.1 lists the uncertainties of the standard instrumentation installed on the SGT-500 engine, as given by the gas turbine manufacturer. Note that the uncertainty and the repeatability of the sensor measuring the fuel flow are not available (NA). The fuel flow is measured by the platform operator on the fuel supply ducts. No certain information for this measuring instrument was accessible.

Table C.1: Uncertainty and repeatability of the standard instrumentation of the SGT-500 gas turbine as provided by the manufacturer.

Measurement	**Uncertainty**	**Repeatability**
Generator output [%]	1.0	0.25
Ambient temperature [°C]	3	1
Ambient pressure [%]	0.5	0.2
Fuel temperature [°C]	0.5	1
Fuel flow [$kg \cdot s^{-1}$]	NA	NA
Outlet temperature HPC [°C]	5	3
Outlet temperature PT [°C]	5	3
LP, HP, PT shaft speeds [rpm]	-	Accurate within a few rpm
Outlet pressure HPC [%]	0.5	1.0
Outlet pressure LPT [%]	0.5	1.0

DTU Mechanical Engineering
Section of Thermal Energy
Technical University of Denmark

Nils Koppels Allé, Bld. 403
DK- 2800 Kgs. Lyngby
Denmark
Phone (+45) 4525 4131
Fax (+45) 4588 4325
www.mek.dtu.dk
ISBN: 978-87-7475-411-4

DCAMM
Danish Center for Applied Mathematics and Mechanics

Nils Koppels Allé, Bld. 404
DK-2800 Kgs. Lyngby
Denmark
Phone (+45) 4525 4250
Fax (+45) 4593 1475
www.dcamm.dk
ISSN: 0903-1685